Synthesis and Structural Studies on $(Ba,Sr)_3Ga(H,D)O_4$ and Ba_2LiD_3O Oxyhydrides

Nur Ika Puji Ayu

A thesis submitted for the degree of

Doctor of Philosophy

Department of Materials Structure Science

School of High Energy Accelerator Science

The Graduate University for Advanced Studies, SOKENDAI

June 2021

Table of Contents

Chapter 1 Introduction **1**

1.1 Hydrogen in solids 1

1.2 Oxyhydrides 2

1.3 Hydride ion conduction in oxyhydrides 4

1.4 Perovskite Structure Family 6

1.5 Purpose of Study 8

Chapter 2 Experimental **10**

2.1 High-Pressure Synthesis of A_3GaO_4H (A = Ba, Sr) 10

2.2 Ambient Pressure Synthesis of Ba_2LiD_3O 12

2.3 X-ray Diffraction (XRD) 13

2.4 Neutron Diffraction (ND) 15

2.4.1 Room Temperature ND Experiment of A_3GaO_4H (A = Ba, Sr) 16

2.4.2 High-Temperature ND Experiment of Ba_2LiD_3O 16

2.5 Rietveld Analysis 17

2.6 Bond Valence Sum 19

2.7 Maximum Entropy Method (MEM) Analysis 20

2.8 Thermogravimetry (TG) of A_3GaO_4H (A = Ba, Sr) 22

2.9 Electrochemical Impedance Spectroscopy (EIS) 22

Chapter 3 A New Family of *p*-block Metal Oxyhydrides $A_3GaO_4H_x$ (A = Ba, Sr) **24**

3.1 Introduction 24

3.2 Experimental 26

3.2.1 High-Pressure Synthesis of $A_3GaO_4H_x$ 26

3.3 Results and Discussion 27

3.3.1 X-ray Difraction Pattern 27

3.3.2 Sensitive Synthesis Condition 28

3.3.3 The Synchrotron X-Ray Diffraction (SXRD) 29

3.3.4 Presence of Hydrogen 31

3.3.5 Neutron Diffraction 32

3.3.6 Sample stability and TG of $Ba_{2.85}GaO_4H_{0.70}$ 35
3.3.7 Synthesis route consideration on oxyhydride synthesis 37
3.3.8 Structure stability and H^-/O^{2-} exchangeability 38
3.4 Conclusion 40

Chapter 4 Structural Study of Super-hydrides Conductor Ba_2LiD_3O 41

4.1 Introduction 41
4.2 Experimental 44
4.2.1 Synthesis of Ba_2LiD_3O (BLDO) 44
4.2.2 Characterizations 44
4.3 Result 45
4.3.1 Laboratory X-ray Diffraction 45
4.3.2 Fourier Transform Infrared Spectroscopy (FT-IR) 45
4.3.3 Synchrotron X-ray Diffraction (SXRD) at High Temperature 46
4.3.4 Electrochemical Impedance Spectroscopy (EIS) 49
4.3.5 High-Temperature Neutron Diffraction 50
4.3.6 Structure Refinement for MEM calculation 53
4.4 Discussion 58
4.4.1 Interstitial site at rock-salt layer 58
4.4.2 Interstitial site at perovskite layer 61
4.4.3 Conduction mechanism at perovskite layer 64
4.4.4 Additional contribution of conduction of rock-salt layer 67
4.5 Conclusion 68

Chapter 5 Summary 69

References 71
List of Figures 78
List of Tables 82
Acknowledgments 83

Chapter 1

Introduction

1.1 Hydrogen in solids

Hydrogen, as one of the most abundant elements, 70%-80%, in the universe, has two stable isotopes, hydrogen or protium ^{1}H and deuterium ^{2}H. Another isotope is Tritium ^{3}H which is radioactive. Due to their relative atomic mass difference, their physical properties are also significantly different, making it possible for isotopic element separation. Hydrogen gas has the physical properties of the lightest gas but the highest thermal conductivity and specific heat capacity and highest diffusion capacity due to its smallest atomic size. Hydrogen chemically has the electron configuration 1*s* and Pauling electronegativity 2.1. It results in four different types of compounds formed when hydrogen reacts with other elements with different electronegativity. Those elements can be the electropositive, electronegative, transition metal element, or element with similar electronegativity. In reaction with the electronegative elements or halogen elements, hydrogen exists as cation H^+, such as H_2O. In other cases, hydrogen forms as H^- or hydrides [1], Figure 1.1.

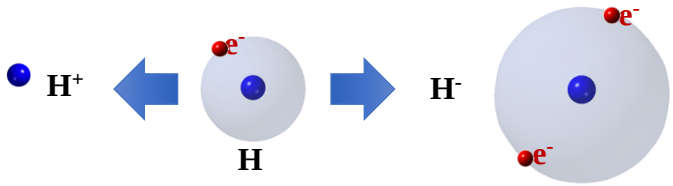

Figure 1.1 Hydrogen in the compound when it donors electron (H^+) or gains electron (H^-).

Hydrides or negative charge of hydrogen has several unique characteristics such as polarizable, flexible in size, and labile character in the material [2]. Based on its bonding with a cation forming a metal hydride, metal hydrides are divided into three kinds of compounds, ionic hydrides, metallic hydrides, and covalent hydrides [3]. Ionic hydrides are hydrides with dominant ionic bonding when hydrogen reacts with electropositive elements (*e.g.*, alkali or alkaline rare earth metal) and gain electrons forming hydrides, such as in BaH_2, SrH_2, and other alkaline metal hydrides. On the other hand, the reaction of hydrogen with an element having

the same electronegativity will result in sharing electron forming covalent bonding, such as group IIIA, IV, or VA elements. Moreover, if hydrogen reacts with transition metal elements, it gives nonstoichiometric metal hydrides, which hydrogen can occupy some interstitial sites in the structure.

In oxide material, hydrogen is commonly present as proton or hydroxide defect sits in the oxygen electron cloud. Proton also can appear in the grain boundary resulting in high resistivity of the grain boundary in the high proton conductor materials [4]. Neutral hydrogen rarely exists in oxide because it is ionized to protons easily. However, at reducing conditions having neutral hydrogen is possible. Meanwhile, the evidence of a stable hydride in oxide was not clearly observed. In a positron study of MgO at reductive condition, hydride could trap electrons even forming H^{2-} [5]. In addition, another report observed oxygen vacancy transport suspected as hydride due to the similar size and charge to oxide [6]. The incorporation of hydride or hydroxide in a cage structure of oxide material was reported in $Ca_{12}Al_{14}O_{13}$, which is shown by detecting electronic conduction upon UV radiation due to hydride ionization [7].

1.2 Oxyhydrides

Heating metal oxide under hydrogen gas usually induces the reduction of the metal. In a specific condition, hydrogen can partly substitute oxygen in forming oxyhydrides compounds. The first discovered metal oxyhydride, LaHO (1982), was synthesized by heating Lanthanum oxide under pure hydrogen gas at 900 ^{o}C. The stabilization of hydride in the oxides required a highly reductive condition at equilibrium [4] and without transferring electrons from hydrogen. Later, some hydrogen stabilized Zintl phase of the tetrel (*Tt*) and triel (*Tr*) family, $Ba_{21}Tt_2O_5H_{24}$ (*Tt*=Ge, Si) and $Ba_{21}Tr_2O_5H_x$ (*Tr*=Ga, In, Tl, x~22) was reported prepared by heating of metal and metal oxide under very reductive condition 1100 ^{o}C for 4 hours in pure hydrogen gas. Another attempt to synthesize $Ba_{17}AlO_3O_7$ in a similar reduction condition accidentally resulted in an anti-perovskite oxyhydride, Ba_3AlO_4H, with an orthorhombic structure where hydrogen occupied the interstitial site of distorted barium-hydride octahedra [8].

Oxyhydrides or partial substitution of oxides by hydrides in the perovskite layer structure was pioneered by Hayward. A partial oxide substitution in $LaSrCoO_4$ by hydride was done through reduction reaction using CaH_2 reductor results in $LaSrCoO_3H_{0.7}$ with the same structure as the oxide parent compound (Figure 1.2) [9]. This report revealed that preparation of oxyhydrides from an oxide material is possible and opens the gate to the oxyhydrides exploration from other oxide materials. Furthermore, the combination of oxide-hydrides or

oxyhydrides with hydride as a soft anion and oxide as hard anions [10] bring about potentially flexible structures and engaging physical and chemical properties.

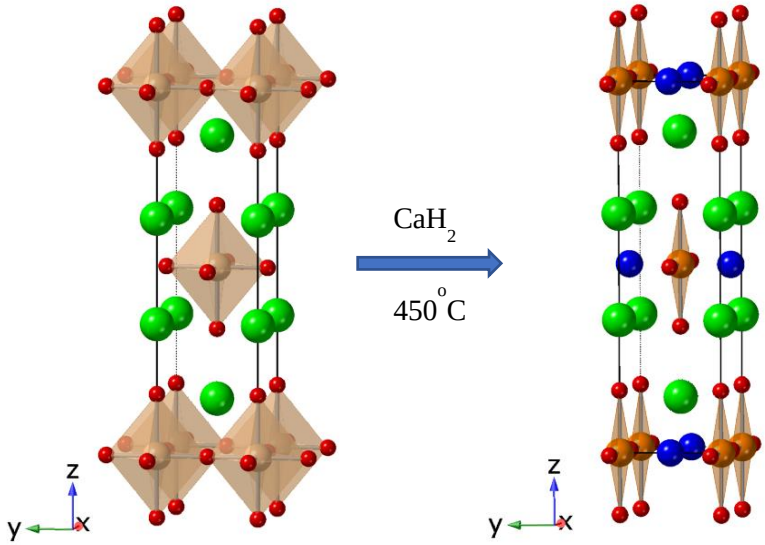

Figure 1.2 The partial replacement of oxygen by hydrogen in the $LaSrCoO_4$ (left) results in oxyhydride $LaSrCo_3H_{0.7}$.

Oxyhydrides synthesis based on the atomic type can be categorized into transition metal oxyhydrides and non-transition metal oxyhydrides. Because transition metals have several oxidation states, transition metal oxyhydrides can be prepared through reduction reaction using metal hydrides or high-pressure synthesis, also known as a topotactic reaction. The hydride substitution induced the changing of oxidation states in the transition metal atom indicated by the changing of sample color [11]. In the indirect synthesis or topotactical reaction, an oxide material is reduced using metal hydrides, such as CaH_2, SrH_2, or LiH. After sintering, washing is necessary to remove the side products. The properties of transition metal oxyhydrides include metal to insulator transition, catalytic activity, or superconductor. The physical properties of a pressure-induced insulator to the metal transition of $SrVO_2H$ are attributed to the *s*-orbital character of hydride [12]. In chemistry, the application of oxyhydride $BaTiO_{2.5}H_{0.5}$ as a catalyst of ammonia production is due to an exchange reaction [13]. For non-transition metal oxyhydride, the possible synthesis method is direct synthesis solid-state reaction under high pressure or conventional solid-state reaction under ambient pressure. The properties that are usually observed in non-transition metal oxyhydride including hydride conductor and catalytic activity. Kobayashi *et al*. reveal the pure H^- conduction in oxyhydride materials in Li-based oxyhydrides, promising for energy storage application [14].

1.3 Hydride ion conduction in oxyhydrides

Hydride mobility was reported in almost all oxyhydrides which make hydride one of the promising carriers. Hydride is a promising candidate for charge carriers because it is monovalent, suitable radius ~1.4 Å, large polarizability, and strong reducing ability, -2.25 V (H_2/H^-) comparable to magnesium ion [15]. Furthermore, high reduction-potential, flexibility in size, and labile character [2] of hydride make hydride ideal for a fast conductor. Hydride ion conduction is studied mostly in alkali metal ion oxyhydrides expecting pure ion conduction. The pure-hydride conduction phenomena were observed in the oxyhydride, $La_{2-x-y}Sr_{x+y}LiH_{1-x+y}O_{3-y}$, with K_2NiF_4-structure [16]. The demonstration of all-solid-state hydrides battery, Ti/*o*-La_2LiHO_3/TiH_2, shows promising future of oxyhydrides application as energy storage [14]. The recent report on hydride conduction in oxyhydrides, as listed in Figure 1.3, could reach practical conductivity at an intermediate temperature where some chemical reactor reactions occur. In comparison, oxide conduction requires a high temperature with a practical conductivity above 400 ^oC [17]. In contrast, proton conduction occurs at low temperatures due to the need for moisture [18].

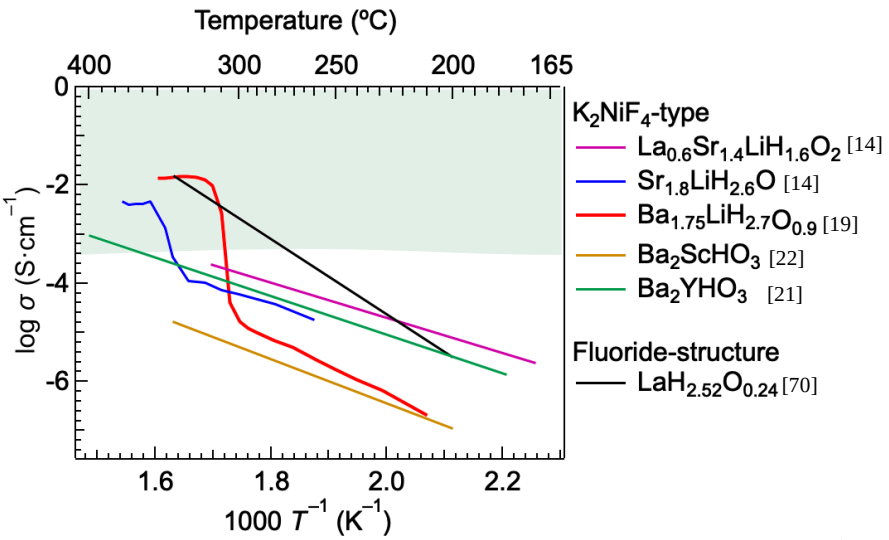

Figure 1.3 Summary of conductivity of reported oxyhydrides.

Among all the reported oxyhydrides in K_2NiF_4-type (Figure 1.3), the $Ba_{1.75}LiH_{2.7}O_{0.9}$ (BLHO) has been investigated as having the highest conductivity ~10^{-2} S·cm^{-1} at 320-350 ^{o}C [16,19]. With higher hydride content than others, hydrides in BLHO occupy both apical and equatorial sites, as drawn in Figure 1.4. In this material, the jump of the conductivity observed at high temperature followed by a phase transition from the orthorhombic structure to the tetragonal structure by doubling the lattice due to the order-disorder transition of hydride at apical and equatorial sites. The ordering of hydride can contribute to different hydride mobility mechanisms that have not been fully understood. The AIMD simulation study of hydride mobility in K_2NiF_4-type structure of $LaSrLiH_2O_2$ and Sr_2LiH_3O, reported that the equatorial hydrides mainly contribute to conduction, and the mobility of equatorial-apical hydrides migration requires larger activation energy compared to equatorial-equatorial hydrides migration [20]. The apical hydride may also contribute the conductivity as in Ba_2YHO_3 with ordering hydride at the apical site showing conductivity of ~10^{-4} S·cm^{-1} [21], different to Ba_2ScHO_3 with disordering of apical hydride [22]. The conduction mechanism in the latter compound was reported as an interstitials mechanism of apical to apical hydrides [23]. While BLHO with hydride occupied both equatorial and apical site, becomes superionic at high temperature. The previous report could not explain the mechanism of hydride conduction at superionic. The detail of the direct relation of phase transition behavior on the conductivity mechanism in BLHO was not unclear. In addition, the light mass of hydrogen made the investigation challenging.

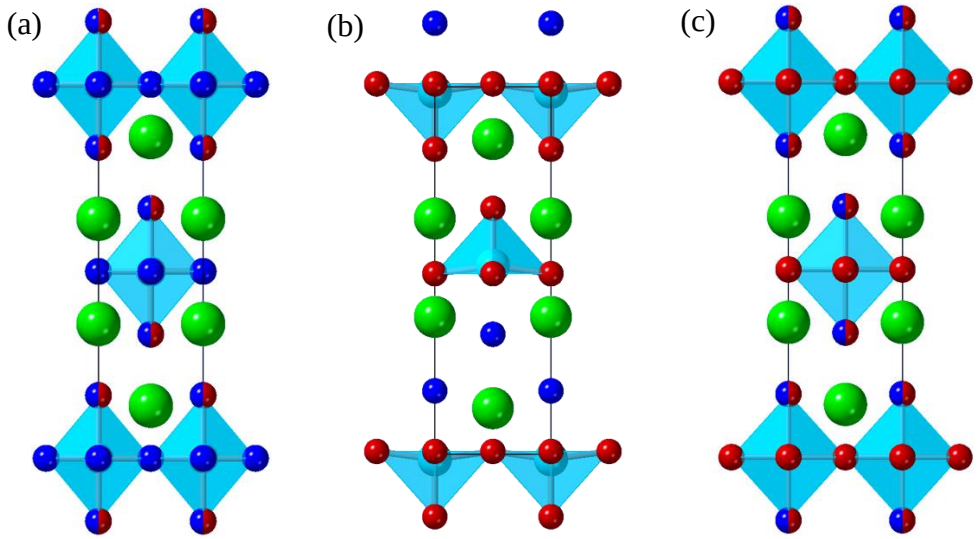

Figure 1.4 The crystal structure of (a) $Ba_{1.75}LiH_{2.7}O_{0.9}$, (b) Ba_2YHO_3, and (c)Ba_2ScHO_3. The green, blue and red balls represent barium, hydrogen, and oxygen, respectively. The tetragonal represents the cation of Li, Y, and Sc in each.

1.4 Perovskite Structure Family

Perovskite structure is one of the well-known structures, with a formula of ABX_3, *A*, and *B* refer to cation and *X* refer to anion shown in Figure 1.5 with BX_6 octahedral. The oxyhydride study in the perovskite structure was reported in Ti-based oxyhydride. Reduction of oxide perovskite $BaTiO_3$ result in $BaTiO_{3-x}H_x$ [24]. Known as a flexible structure, the cation and anion replacement in the perovskite structure induce a distortion due to the changing bond length and angle in the structure. Therefore, a tolerance factor called a Goldsmith tolerance factor, *t*, was introduced. For a simple cubic structure, the Goldsmith tolerance factor is written in equation (1).

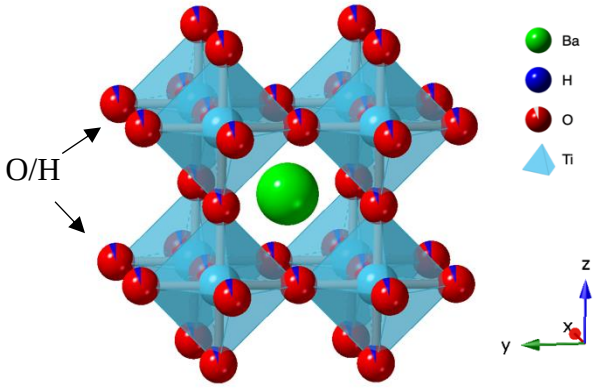

Figure 1.5 Perovskite structure ABX_3 with partial substitution of oxygen by hydride results in $BaTiO_{3-x}H_x$. In this structure, *A*, *B*, and *X* represent barium, titanium, and oxide/hydride.

$$t = \frac{r_A + r_X}{\sqrt{2(r_B + r_X)}} \tag{1.1}$$

r_A, r_B, and r_X are the ionic radii of cation *A*, cation *B*, and anion *X*. The ideal cubic structure results t=1 as the value of t >1 or t<1 the structure distorted yields a lowering crystal structure symmetry. The distorted structure, including cation displacement or BX_3 octahedral tilting or distortion, originated from the small cation size. The lowering crystal structure symmetry also can occur by introducing defects in the crystal, deriving some perovskite-related structures.

The solid solution oxyhydrides of $(Ca,Sr)TiO_{3-x}H_x$ and $(Sr, Ba)TiO_{3-x}H_x$, the small ionic size of Ca^{2+} and Sr^{2+} rising and octahedral tilting (a^-, a^-, c^+) in this solid solution which is an ideal cubic in the Ba-case. The reduction of oxygen phase showing that the lattice size of oxyhydride products expand compared to the oxide phase due to ionic size change of both cation from Ti^{4+}/Ti^{3+} and anion from O^{2-}/H^-. The relatively bigger ionic size of hydrides also increases the tilting angle of titanium and equatorial oxide bonding but has no relation to the

lattice expansion [24]. The flexibility of hydride ions in the perovskite structure was reported in other perovskite family structures, such as in anti-perovskite and K_2NiF_4-type structures.

An anti-perovskite or inverse perovskite structure is the perovskite structure with the opposite cation and anion position. If the perovskite structure expressed by ABX_3 with *A* and *B* are cations, and *X* is an anion, the anti-perovskite structure is expressed by AXB_3, with XB_3 octahedral sharing *B* edge cation. One example of the cubic anti-perovskite structure is $GaNMn_3$ with *p*-block elements cation. Oxyhydrides study in the anti-perovskite structure was reported in M_3HCh (*M* = Li, Na, *Ch*=chalcogenide). The considerable size flexibility of the hydride anion was reported to support the aliovalent substitution in enhancing the conductivity of Li^+ and Na^+ in the structure [25].

Another family member of the perovskite structure that is well explored for oxyhydrides study is the K_2NiF_4-type structure which has a layered structure. It is a modular structure that incorporates a rock-salt layer slab with a perovskite layer slab. This structure is ideal tetragonal with perovskite slab displacement $(a_p + b_p)/2$ and Ruddlesden-Popper structure with n=1 representing the number of inter-slab layers drawn in Figure 1.6. As previously mentioned, the hydride conductor materials in the Li-based oxyhydrides were reported having a K_2NiF_4-type structure. This structure type is interesting for oxyhydride conductor study because it allows several possibilities of hydrides ordering which is fascinating in the study of hydride conduction not only resulting in the two-dimensional pathway but also possibly in three-dimensional. The summary of reported oxyhydrides in the perovskite structure family is listed in Table 1.1.

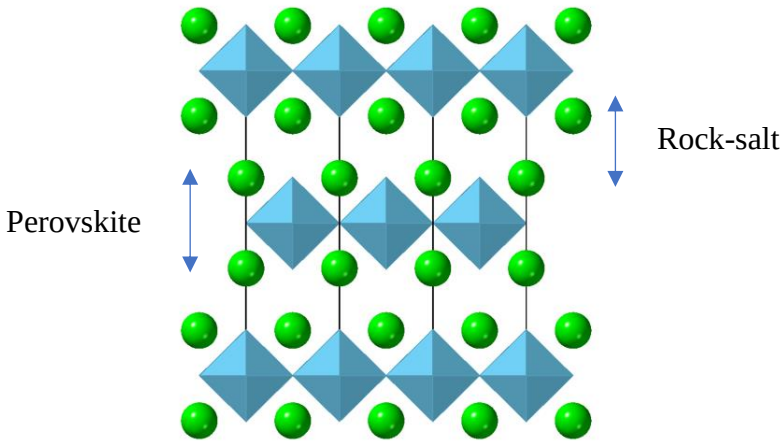

Figure 1.6 K_2NiF_4 structure showing a slab of layered perovskite and rock-salt structure.

Table 1.1 Summary of reported oxyhydrides.

Z	***TM*/*Ae****	**Compound**	**Structure**	**Hydride ordering**	**Ref.**
3	Li	(Ca,Sr,Ba,*Ln*)$LiH_{4-x}O_y$	RP (n=1)	Ordered	[14,26,27]
22	Ti	(Ca,Sr,Ba)$TiO_{3-x}H_x$	Cubic perovskite	Disordered	[24]
		$EuTiO_{3-x}H_x$	Cubic perovskite	Disordered	[28]
23	V	$SrVO_2H$	Cubic perovskite	Ordered	[29], [30]
		$BaVO_3H$	Cubic perovskite	Ordered	[31]
		$Sr_2VO_{4-x}H_x$	RP (n=1)	Ordered	[32], [33]
24	Cr	$SrCrO_{3-x}H_x$	Cubic perovskite	Disordered	[34]
25	Mn	$LaSrMnO_{3.3}H_{0.7}$	RP (n=1)	Partially ordered	[35]
27	Co	$LaSrCoO_3H_{0.7}$	RP (n=1)	Partially ordered	[36]
		$Sr_2Co_2O_{4.33}H_{0.84}$	RP (n=2)	Partially ordered	[36]
38	Sc	$BaScO_2H$	Cubic perovskite	Disordered	[37]
		Ba_2ScHO_3	RP (n=1)	Ordered	[22]
39	Y	Ba_2YHO_3	RP (n=1)	Ordered	[21]
44	Ru	$LaSr_3NiRuO_4H_4$	RP (n=1)	Ordered	[38]
45	Rh	$La_{0.5}Sr_{1.5}Mn_{0.5}Rh_{0.5}O_3H$	RP (n=1)		[39]

**Ln* (lanthanides), *Ae* (alkaline earth), *TM* (Transition Metal).

1.5 Purpose of Study

Hydride ion incorporation into oxide material, oxyhydride, result in several unique physical and chemical properties such as metal to insulator transition under pressure, superconductor, catalyst, and hydride conduction. Despite its attractive properties, the preparation of oxyhydrides with poor elemental selectivity is challenging in material exploration. Recently, there has been less report on *p*-element metal oxyhydrides despite some attractive application of *p*-metal elements due to its dual nature of metallicity and non-metallicity. Concerning this background, oxyhydride material exploration is one of the purposes of this study. The successful preparation of gallium content oxyhydrides is reported in Chapter 3, then discussed to gain the crystal chemistry knowledge of *p*-element metal oxyhydrides. As hydrides mobility was reported in almost all oxyhydrides, a hydride ion is one of the promising charge carriers. A super hydride conductor was reported in $Ba_{1.75}LiH_{2.7}O_{0.9}$ (BLHO). However, the hydride conductor mechanism in a superionic phase is unclear. In this report, the investigation of the conduction mechanism was done by a structural study using

MEM analysis reported in Chapter 4. A new conduction mechanism in a superionic hydride conductor was proposed in this study.

Chapter 2

Experimental

2.1 High-Pressure Synthesis of A_3GaO_4H (A = Ba, Sr)

The high-pressure study of materials is quite popular due to some distinct physical or chemical properties that only appear in high pressure. In chemistry, the smallest value of enthalpy and internal energy is expected for the most stable phase. Applied pressure affects chemical stability. Therefore, the pressure-dependent phenomena such as shifting of transition temperature or melting point are observed. Under pressure, the material undergoes a transition to a denser phase or other metastable phases. The quenching or rapid cooling under pressure can result in a preserved this metastable phase at atmospheric pressure. In the point of view of physics, the pressure increases the overlap between adjacent electronic orbital. In an insulator or semiconductor case, it may decrease the resistivity and lead to a metallic behavior.

The use of high pressure for synthesis was neglected in the early 19's century. The complexity of the instrument is one of the possible reasons. Around 1945, geologists start to consider high-pressure to synthesize some minerals [40]. Later, the development of high-pressure instruments for material synthesis grows rapidly and takes an essential role in synthesizing new material under high pressure. There are several types of high-pressure apparatus. The higher the expected pressure, the more sophisticated techniques are required. Some apparatus such as the Piston-cylinder apparatus and belt type apparatus pressures up to ~ 6 GPa. Another apparatus type, the cubic anvil apparatus, could provide a relatively homogeneous distribution of pressure up to 15 GPa for encapsulated samples. The cubic anvil apparatus at the Institute for Molecular Science (IMS), NINS, was used for the sample preparation in this study, as shown in Figure 2.1.

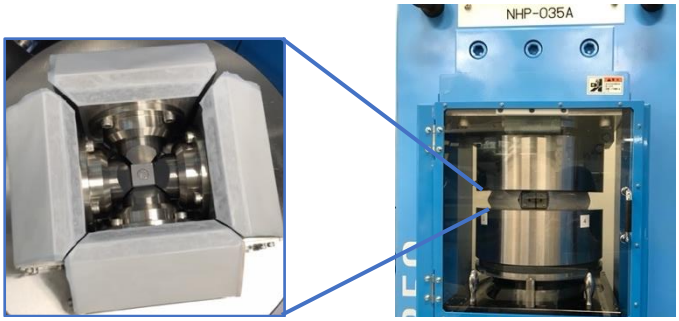

Figure 2.1 Cubic anvil of high-pressure apparatus.

The A_3GaO_4H (A = Ba, Sr) was prepared using a high-pressure method. The stoichiometric composition of the starting materials, AH_2 (99.5%, Mitsuwa Chemical Co.), AO (99.99%, Aldrich), and Ga_2O_3 (99.99%, Aldrich), were weighted in an Ar-filled glovebox, then mixed using planetary ball milling Fritsch-Pulverisette Premium line sealed in Ar-gas. The milling program was varied from 150 rpm to 600 rpm to obtain the optimum conditions. The optimum conditions were ball-milled using ZrO_2 pot and balls under 600 rpm for 2.5-3 hours. The obtained mixture then pelletized into a 5 mm-diameter of pellet under 20 MPa using a stainless-steel die.

During the sintering under pressure, the sample is isolated in the cubic pyrophyllite with several sleeves cover it, as shown in Figure 2.2 [2]. From the outer layer, cubic pyrophyllite with the size of 16 mm, to the inner layer, it consists of a graphite heater sleeve that connected to the molybdenum plate on the cap as an electrode, NaCl sleeve, and BN sleeve to isolate hydrogen during sintering. The sintering temperature should be lower than the melting point of NaCl at the expected sintering pressure, as it becomes one of the limitations of this method. The mixed raw materials pellet is assembled inside the cubic pyrophyllite following the order mentioned above. The cube then pressed to 2 GPa and sintered to 800 ^oC for 30 minutes before finally quenched to room temperature, following by releasing the pressure. The amount of sample that can be prepared within one batch of high-pressure synthesis is about 0.3 gram.

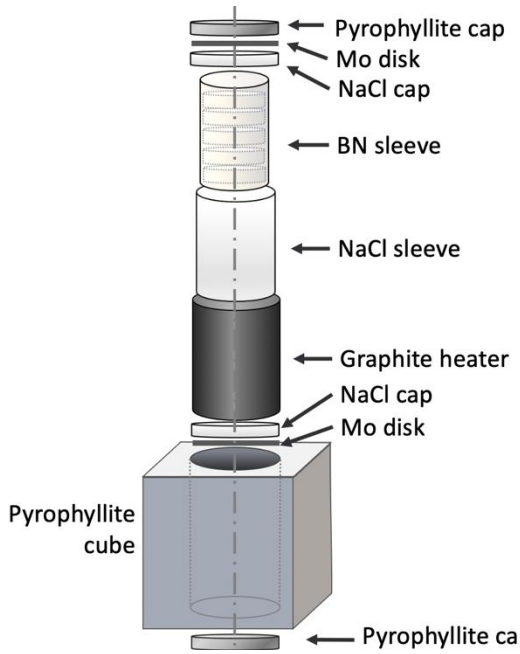

Figure 2.2 The high-pressure cubic cell assembly.

2.2 Ambient Pressure Synthesis of Ba_2LiD_3O

Oxyhydride prepared by direct solid-state reaction under high-pressure results in a small amount sample due to the limitation of the apparatus. The ambient pressure synthesis is preferable for a larger sample which stable at ambient pressure. Therefore, for a high-temperature neutron diffraction study, a nonstoichiometric $Ba_2LiD_3O_4$ in this report was prepared under ambient pressure synthesis at IMS, NINS. The raw materials of BaO (99.99%, Aldrich), BaH_2 (99.5%, Mitsuwa Chemical Co.), and LiH_2 (99.99%, Aldrich) was mixed in a ratio of 0.93:1:1.5 using planetary ball milling in an agate pot under 150 rpm for 30 minutes, then pelletized into a 5.5 mm diameter and 1.5 thickness. The sample is sintered inside a stainless-steel container on a stainless-steel crucible, as shown in Figure 2.4. The sample was

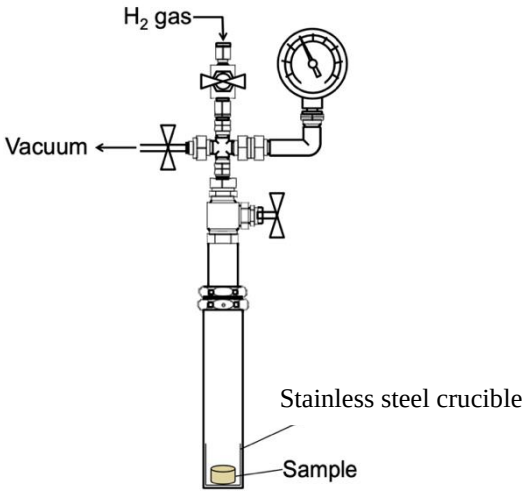

Figure 2.4 The stainless-steel container for ambient pressure synthesis.

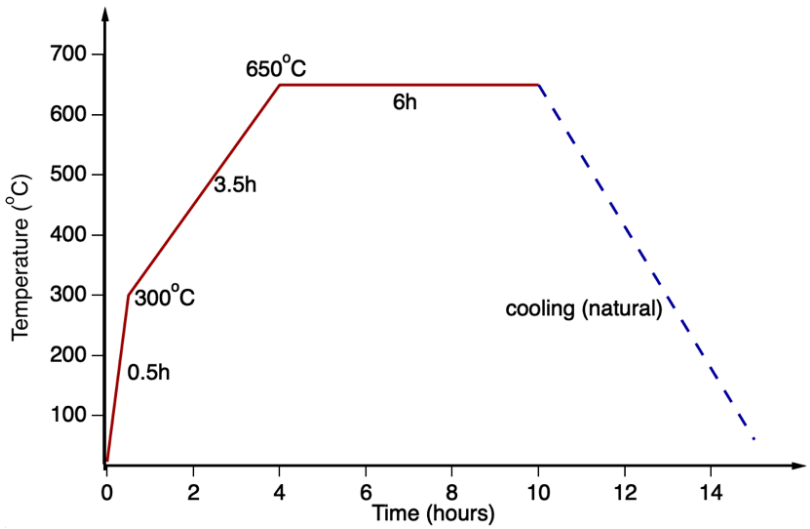

Figure 2.3 The heating program of ambient pressure synthesis of Ba_2LiD_3O.

sintered under deuterium gas pressure of 0.2 MPa. The heating program of the sintering is in Figure 2.3.

2.3 X-ray Diffraction (XRD)

The X-ray diffraction (XRD) measurement was conducted to confirm the sample quality, phases, and structure using a laboratory X-ray diffractometer with Cu source. A Cu source generator produce the wavelength of CuKα_1 and CuKα_2, 1.5406 Å and 1.5444 Å. The wavelength of the X-ray is comparable to the interatomic distance of atoms in the matters which in crystalline material, the periodic arrangement of atoms can be expressed as eq (2.1).

$$r' = r + \mathbf{R}, \qquad \text{with } \mathbf{R} = n_1\mathbf{a}_1 + n_2\mathbf{a}_2 + n_3\mathbf{a}_3 \tag{2.1}$$

with n_j is an arbitrary integer, $\mathbf{a}_j$ as three independent vectors, and r is a primitive unit with periodicity translated by **R**. The periodicity of the lattice can be explained by the Fourier transform of the periodic function $f(x)$ of period a satisfy $f(x) = f(x - na) = f(x - R)$, then the Fourier

$$f(x) = F^{-1}[f](x) = \frac{1}{\sqrt{2\pi}}\int_{-\infty}^{\infty} e^{ikx} f(k)dk \tag{2.2}$$

The k value that satisfies the periodicity of lattice or $\exp(ikx) = \exp[ik(x - a)]$ is indicated by notation G, where the Fourier component vanishes for every $k \neq G$. In this case, the G points form a regular lattice known as a reciprocal lattice. The relation between direct lattice point R and reciprocal lattice point G satisfy $e^{iRG} = e^{inal2\pi/a} = e^{i2\pi nl} = 1$.

In the diffraction experiment or elastic scattering, the is incoming wave vector k and radiated wave vector k′ are preserved $|\mathrm{k}| = |\mathrm{k}'|$. Where transferred wave vector $\mathrm{q} = \mathrm{k}' - \mathrm{k}$ holds the information of radiation angle and wavelength. The Bragg diffraction peak occurs when $\mathrm{q} = \mathrm{G}$ in the 3D reciprocal lattice or $|\mathrm{k}| = |\mathrm{k}'| = |\mathrm{k} + \mathrm{G}|$. The scattering is observed at angle 2θ related to the lengths of k and G

$$\sin\theta = \frac{|\mathbf{G}|}{2|\mathbf{k}|} \tag{2.3}$$

with lattice planes separated by $d = n2\pi/|\mathbf{G}|$, and radiation wavelength related with |k| by $|k| = 2\pi/\lambda$, the substitution of |k| and |G| to eq (2.3) yields Bragg condition for diffraction.

$$2d \sin\theta = n\lambda \tag{2.4}$$

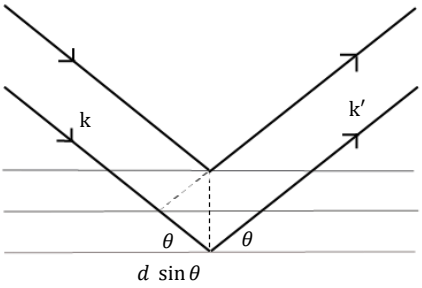

Figure 2.5 Bragg condition for diffraction.

The X-ray diffraction performed using laboratory X-ray diffractometer at Institute for Molecular Science. Laboratory X-ray diffraction (XRD) data collected using Rigaku MiniFlex 600 with Bragg Brentano set-up, CuKα_1 and CuKα_2 wavelength coexist. Some other XRD measurements were collected using Rigaku-Smartlab with CuKα_1 wavelength at the Institute of Material Structure Science (IMSS), KEK. There are two kinds of sample holders used; the set-up of the sample on the sample holders is shown in Figure 2.6 (a) Aluminum holder, and (b) Rigaku holder.

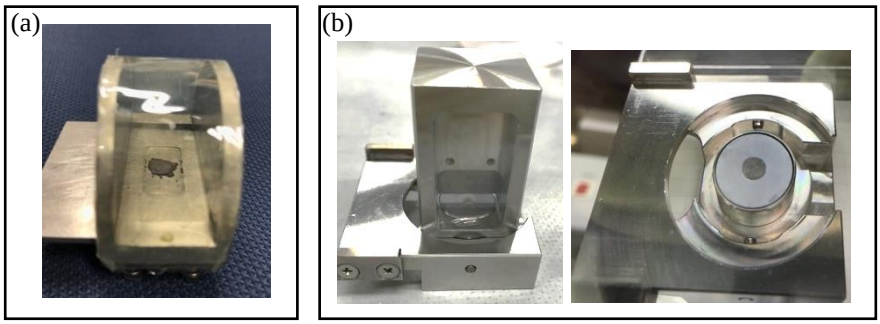

Figure 2.6 XRD sample holder for air-sensitive sample, (a) Al and (b) Silicon Rigaku holder.

Synchrotron radiation is the most powerful X-ray source with strong intensity. The SXRD measurement was performed at BL02B2, SPring-8 using a diffractometer with Debye-Scherer set-up. For the room temperature measurement, the sample was sealed inside a glass capillary with a diameter of 0.3 mm filled with Ar gas. For the high temperature SXRD measurement of Ba_2LiD_3O, the sample was sealed in the quartz capillary with a diameter of 3 mm under vacuum. The temperature-dependent measurement was done up to 400 ^oC, above its phase transition temperature. The X-ray wavelength operated in the beamline was 0.4198 Å. A short-wavelength X-ray is easy to penetrate or termed as *hard.* In contrast, long-

wavelength x-rays are easily absorbed and termed as *soft*. Therefore, checking the estimation of the X-ray absorption by the sample is necessary before the measurement to make sure that the collected data will be reliable.

2.4 Neutron Diffraction (ND)

The main difference between X-ray diffraction and neutron diffraction is its interaction with matter. The primary interaction of X-ray is with the electron in the material; therefore, the scattering factor in the X-ray diffraction increase by increasing the number of electrons. In neutron diffraction, the neutron interacts with the nucleus including the spin interaction and the scattering factor of atoms corresponds to the scattering length, *b*. The scattering length of some atoms related to the material in this report and the absorption coefficient are listed in Table 2.1.

Table 2.1 The list of scattering lengths, *b*, of some atoms on this report.

Atom	**Coherent *b***	**Incoherent *b***	**Abs xs***
Ba	5.07	--	1.10
Sr	7.02	--	1.28
Ga	7.288	--	2.75
O	5.803	--	0.00019
H	-3.7406	25.274	0.3326
D	6.671	4.04	0.000519
Li	-1.90	--	70.5

*xs: cross section/barn=1E-24cm^2, b: scattering length/fm=1E-15m.

The time of flight (ToF) method to study polycrystalline material was pioneered by Bronislaw Buras (1915-1994) and Fiodor Lvovitch Shapiro (1915 -1973) [10]. In the neutron scattering the polychromatic neutron beam coming from one direction. After hitting the sample, neutron scattered in all direction and detected to obtain its scattering information. The neutron wavelength is calculated in diffraction case to fulfill the Bragg Law written in equation (2.5)

$$\lambda_{hkl} = 2d_{hkl} \sin\theta \tag{2.5}$$

The neutron wavelength can be determined from the de Broglie wave relation considering neutron character as a particle

$$\lambda = \frac{h}{mV} = \frac{ht}{ml} = \frac{At}{l} \tag{2.6}$$

with λ is neutron wavelength, mV is momentum, h is Plank constant, A is a constant, and l is neutron flight path length which represents the length between the sample to the detector. Equation (2.6) shows the linear relation between the neutron wavelength and time of neutron to travel as the main idea of the time-of-flight method. Finally, we can calculate the constant,

A, is about 3.956×10^{-7} m^2/s or 0.3956 km^2/s. The neutron diffraction data were collected at BL09 SPICA, J-PARC [41]. The SPICA layout illustrated in Figure 2.7 has several detector banks, the backscattering bank and multi-purpose banks. The highest $\Delta d/d$ resolution of the back scattering bank was recognized as high as 0.09% in the case of diamond powder. In this report, the principal analyses were all using data collected at backscattering bank which collect neutron scattered at angle 175-150 degrees.

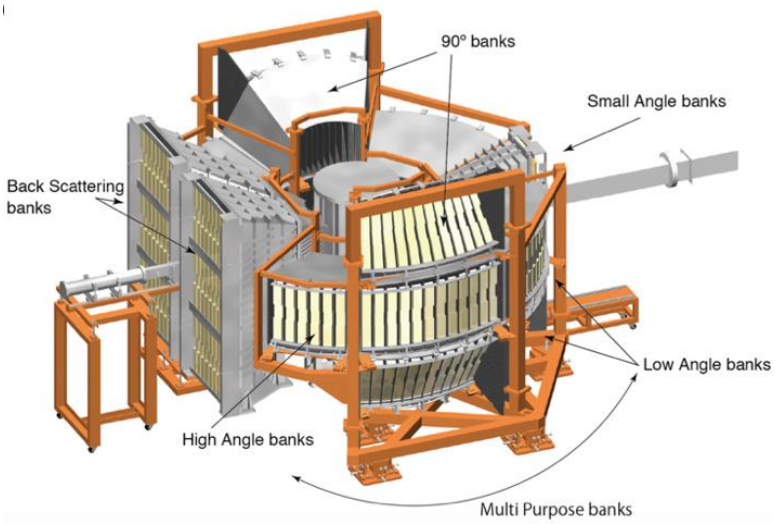

Figure 2.7 Layout of beam line BL09 SPICA.

2.4.1 Room Temperature ND Experiment of A_3GaO_4H (A = Ba, Sr)

The room temperature ND measurement performed using an auto-sample changer environment. The sample was put inside a V-Ni can holder with a SUS cap and sealed with rubber inside an Ar gas-filled glovebox. The sample amount was small, about 0.3 gram for each measurement. Inside a 6 mm diameter V-Ni, the sample height was about 3 mm. Due to the small amount of sample, the long measurement was necessary. The neutron diffraction data were collected for about 12 hours to obtain over ten thousand neutron counts statistics with slit size of the incoming beam fixed to 20×40 mm for auto-sample changer environment. During the measurement sample was rotated for better averaging the diffraction data.

2.4.2 High-Temperature ND Experiment of Ba_2LiD_3O

The high-temperature ND measurement performed at BL09 SPICA beamline J-PARC, using a Cryo-furnace environment. The sample was put inside a V-Ni can holder with Cu cap and sealed inside an Ar-gas-filled glovebox. The sample is then attached to the sample stick

and covered by three layers of radiation shield as detailed in Figure 2.9. The heater and sensor-C are set up above the edge of the sample can. The heating program controlled the temperature at the sensor-C which calibrated to approach the expected sample temperature. The sensor-C temperature and the heating program for the measurement is plotted in Figure 2.8.

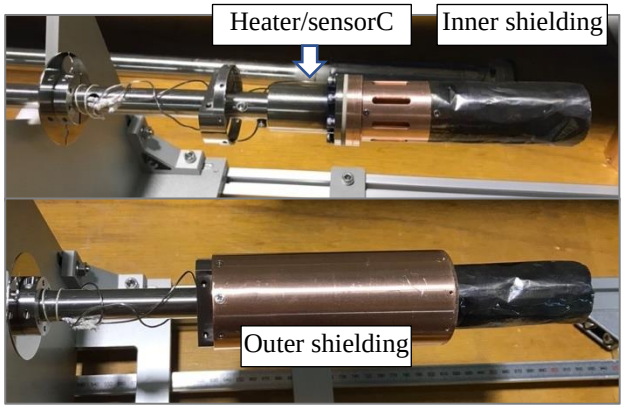

Figure 2.9 Radiation shield covered the sample attached to the sample stick for the Cryo-furnace.

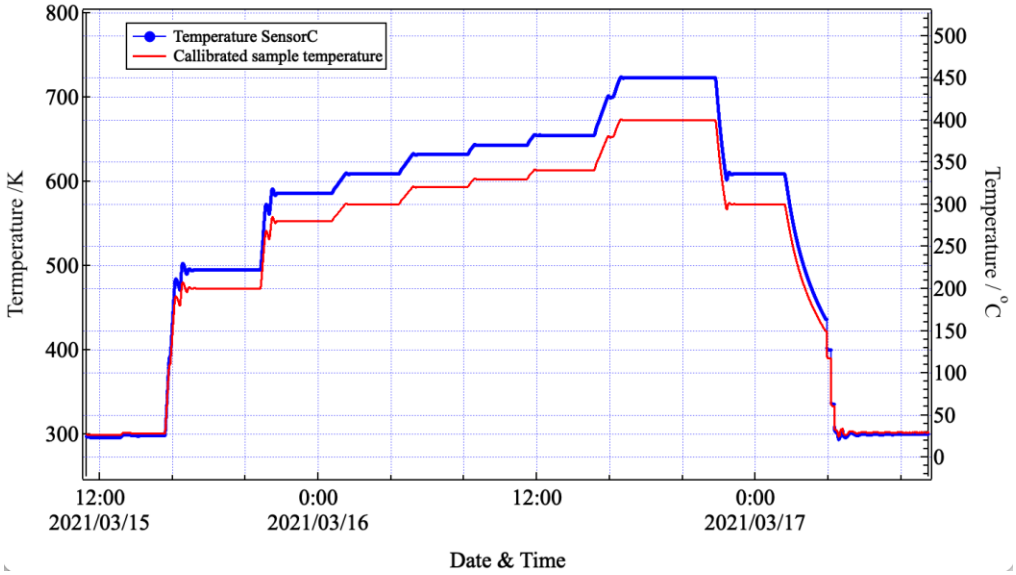

Figure 2.8 The heating program of temperature dependent neutron measurement of Ba_2LiD_3O.

2.5 Rietveld Analysis

Hugo Rietveld introduced the Rietveld method. Before the Rietveld method, there are two other well-known methods in the whole pattern fitting, the Pawley method or Le-Bail method. The Pawley method has significant differences from other methods. In the case of the angle-dispersive method, every single reflection is assumed to have a peak position with a 2θ error and peak width determined by the resolution function. A typical square matrix (10+N)

× (10+N) is required in the least-squares minimization procedure, with N as the number of symmetry independent. The problem in the peak separation sometimes appears, especially in the case of overlapping peaks. Pawley may miscalculate as a negative peak. In this case, introducing both constraints and restraints is necessary. There is so-called profile intensity partitioning in the Le-bail method, which works for any number of overlapping peaks. Both methods still have difficulty in overlapping peaks that commonly appear at high symmetry cases. Some Laue classes are impossible to derive reliable peak intensity such as in *4/m* and *6/m*, which is indistinguishable with *4/mmm* and *6/mmm*.

In the Rietveld method, the residual least-squares refinement is expressed by

$$S_y = \sum_i w_i (y_i - y_{ci})^2 \tag{2.7}$$

where w_i, y_i, and y_{ci} are the weighting factor calculated as $1/y_i$, the observed intensity at point *i*, and the calculated intensity at *i*. The Bragg reflections contribute to y_i. The calculated intensity is the summation of the structure factor $|F|^2$ of all reflections. Including the background and other contributions, the Bragg reflections are written in equation (2.8) [42].

$$y_{ci} = s \sum_k L_k |F_k|^2 \emptyset (2\theta_i - 2\theta_k). P_k A + y_{bi} \tag{2.8}$$

where s is scale factor, k is the miller index label, $L_k, \emptyset, P_k$ and A are Lorentzian factor, profile function, preferred orientation, and absorption factor. The addition y_{bi} represents the background. The structure factor, F_k, is expressed by

$$F_K = \sum_j N_j f_j \exp\left[2\pi i (hx_j + ky_j + lz_j)\right] \exp\left[-M_j\right] \tag{2.9}$$

with N_j are the site occupancy multiplier of the *j*th atom at the position or coordinate (x_j, y_j, z_j). The *h*,*k*, and *l* are Miller indices and M_j is the temperature factor of the atom due to the thermal motion given by the equation

$$M_j = 8\pi^2 \overline{u_s^2} \sin^2\theta / \lambda^2 \tag{2.10}$$

In this report, M_j is labeled as *B* with a unit of $Å^2$. The temperature factor is also commonly expressed as u_s (Å) in equation (2.10) that directly represents the displacement of the *j*th atom parallel to the diffraction vector.

The Rietveld refinement is a least-squares iteration process adjusting the calculated structure parameters to fit the experimental data best to obtain the crystal structure solution.

During the process, there several criteria of fitting that reflect the fitting quality. The numerical criteria of fit are known as the following.

$$R_{\mathrm{F}} = \frac{\sum\left|(I_k('\mathrm{obs}'))^{1/2} - (I_k(\mathrm{calc})^{1/2})\right|}{\sum(I_k('\mathrm{obs}'))^{1/2}} \tag{2.11}$$

$$R_{\mathrm{B}} = \frac{\sum|I_k('\mathrm{obs}') - I_k(\mathrm{calc})|}{\sum I_k('\mathrm{obs}')} \tag{2.12}$$

$$R_{\mathrm{p}} = \frac{\sum|y_i(\mathrm{obs}) - y_i(\mathrm{calc})|}{\sum y_i(\mathrm{obs})} \tag{2.13}$$

$$R_{\mathrm{wp}} = \left\{\frac{\sum w_i\left(y_i(\mathrm{obs}) - y_i(\mathrm{calc})\right)^2}{\sum w_i(y_i(\mathrm{obs}))^2}\right\}^{1/2} \tag{2.14}$$

where I_k represents the intensity of the *k*th Bragg peak at the end of refinement cycles. R_{F} and R_{B} are the *R*-Factor and *R*-Bragg, which indicates the reliability of the structure model. Whereas the criteria of pattern fitting are represented by R_{p} and R_{wp} or *R*-pattern and *R*-weighted pattern. Overall, the 'goodness of fit' indicator S is

$$S = \frac{R_{\mathrm{wp}}}{R_{\mathrm{e}}} \tag{2.15}$$

$$R_{\mathrm{e}} = \left[[\mathrm{N} - \mathrm{P}]/\sum w_i y_{oi}^2\right]^{1/2} \tag{2.16}$$

The R_{e} is the *R*-expected value with P and N are number of refined parameters and number of observations y_i. All the diffraction data in this report are refined using *Z-Rietveld* program [43].

2.6 Bond Valence Sum

In 1929 Pauling L postulated a valence principle stated the valence of an atom *V* is equal to the total valence of the surrounding atoms, v_i (eq 2.17). Which, the valence of the atom regards to the valence-shell electrons contributed to the bonding.

$$V = \sum v_i \tag{2.17}$$

This concept suggests a relation between bond valence and bond length that can be used to evaluate the ionic structure, as it obeys the equation (2.18).

$$v_i = \exp\left(\frac{R_0 - R}{b}\right) \tag{2.18}$$

with

R_0= ideal bond length

R= observed bond length

b= empirical constant, 0.37Å

the value of the R_0 and b obtained from various sources at the references[44,45]. The general tendency is that if the bond valence increases, the bond length decreases. Moreover, if the bond valence is kept fixed, the bong length should change and *vice versa*, known as the distortion theorem. It means if an atom lies in a large cavity, the bonds will be longer than the expected value and results in a low bond valence sum. By moving the atom away from the center of the cavity, some of the bonds are shortened, and others are lengthened. Therefore, it can increase the bond sum valence. So, by calculating the bond valence sum, we could evaluate defects in the structure.

2.7 Maximum Entropy Method (MEM) Analysis

The maximum entropy method (MEM) application by maximizing the entropy of the map for calculating the structure factor has become powerful problems solving incomplete information in the powder diffraction data. In the X-ray single-crystal diffraction data, the accurate amplitudes of the structure factor make it possible to project the three-dimensional reciprocal lattice space directly. The powder diffraction data is limited by the phase problem, making it difficult to obtain accurate information on the structure factor. Extracting the individual structure factor of overlapping peaks is even more difficult in a bigger unit cell. The MEM analysis can derive the more accurate density (electron or nucleus) distribution from the powder diffraction data than the Fourier-transformation method [46].

In the powder diffraction pattern, the fundamental relation of integrated intensity is proportional with the square of the structure factor ($I \propto |F|^2$) as in equation (2.8). And the calculated structure factor can be written as

$$F_{\text{cal}}(\mathbf{k}) = \sum_i f_i(\mathbf{k}) \exp\{2\pi i(hx_i + ky_i + lz_i\} T_i(\mathbf{k}) \quad (2.19)$$

with f and T are the atom type and calculated thermal factor, then the Fourier Transform relation of the density on a sufficiently fine grid of N_1 x N_2 x N_3 pixel over unit cell $\mathbf{r}$, $\rho(\mathbf{r})$, is expressed by

$$\rho(\mathbf{r}) = \int F(\mathbf{k}) \exp(-2\pi i \mathbf{k}.\mathbf{r}) T_i(\mathbf{k})\ dv \quad (2.20)$$

The definition of information entropy is similar to the concept of entropy of thermal kinetics. As part of Bayesian statistics, the MEM includes prior density, $\tau(r)$. The entropy S is defined as in equation (2.21)

$$S = -\sum_r \rho'(r) \ln \frac{\rho'(\mathbf{r})}{\tau'(\mathbf{r})} \quad (2.21)$$

where $\rho'(\mathbf{r})$ and $\tau'(\mathbf{r})$ represents the prior probability at *N*th and *(N+1)*th, $\rho'(\mathrm{r}) = \rho/\Sigma\rho(\mathrm{r})$, and $\tau'(\mathbf{r}) = \tau/\Sigma\tau(\mathbf{r})$.

The MEM criterion selects the density of maximum entropy that fulfill the constraint to avoid some noise in the Gaussian distribution of their standard uncertainty, σ. By using the constraint, each trial $\rho'(\mathrm{r})$ can be accepted or rejected based on its agreement with the experimental data. To obtain the best fit solution the constraint is applied.

$$C = \frac{1}{N} \sum_k \frac{|F_{\text{cal}}(\mathbf{k}) - F_{\text{obs}}(\mathbf{k})|^2}{\sigma^2(\mathbf{k})} \quad (2.22)$$

if C <1, we can get the solution within the statistic error. Thus, this parameter indicates the convergence condition. Here, the F_{cal} means the inversed relation between the structure factor F and the density distribution ρ in the unit cell.

$$F_{\text{cal}}(\mathbf{k}) = \sum_r \rho(\mathbf{k}) \exp(-2\pi i \mathbf{k}.\mathbf{r}) \times \text{Cell Volume} \quad (2.23)$$

Lagrange's method of an undetermined multiplier is used to constrain C to be unity while maximizing the entropy.

$$Q(\lambda) = -\sum_r \rho'(\mathbf{r}) \ln \frac{\rho'(\mathbf{r})}{\tau'(\mathbf{r})} - \frac{\lambda}{2}(C - 1) \quad (2.24)$$

The maximum of Q follows from $\partial Q(\lambda)/\partial\rho'(r) = 0$, for all $\rho'(r)$, resulting the formal solution of $\rho(r)$ written in a function of λ by

$$\rho(\mathbf{r}) = \tau(\mathbf{r}) \,.\exp\left[\frac{\lambda F_0}{N}\sum_{\mathbf{k}}\frac{\{F_{\text{obs}}(\mathbf{k}) - F_{\text{cal}}(\mathbf{k})\}}{\sigma^2(\mathbf{k})}\exp(-2\pi i\mathbf{k}.\mathbf{r})\right] \qquad (2.25)$$

The MEM analysis in this report are calculated using *Z-MEM* program [47] integrated in the Z-Rietveld software using recommended setting of lattice mesh, T, λ multiplier, modify σF equal to 5 and deselect peaks which has nearly zero intensity, large deviation (>50%) or overlap with impurity peaks.

2.8 Thermogravimetry (TG) of A_3GaO_4H (*A* = Ba, Sr)

Thermogravimetric analysis is a technique to measure a sample's thermal stability by precisely monitoring the change of sample mass during constant heating refers to the mass of reference material. The thermogravimetry analysis was performed using Rigaku TG 8121 Thermo EVO at IMS, NINS, with a horizontal sample set-up. The sample was placed on an Al-pan with an initial mass of about 15 mg. The exact amount of Al_2O_3 powder was prepared as a reference considering its stability up to 500 ^oC. The measurement was done under Ar and O_2 gas flow of 100 mL/min. During measurement, the sample heated from room temperature up to 500 ^oC and then cooled down to 50 ^oC with the heating and cooling rate of 5 ^oC/min, as plotted in Figure 2.10. All the sample handling and the measurement were done inside an Ar-filled glovebox. The XRD patterns were measured before and after TG.

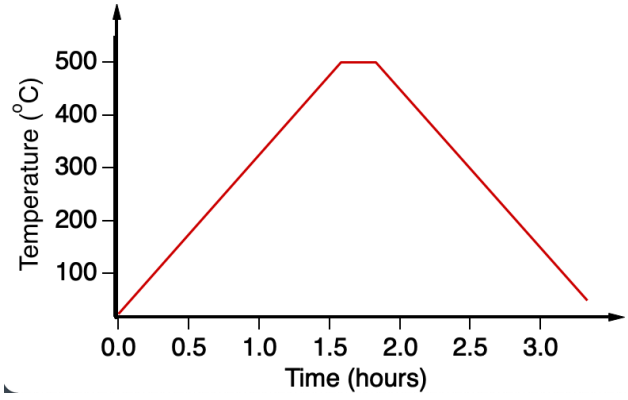

Figure 2.10 Heating program of TG measurement.

2.9 Electrochemical Impedance Spectroscopy (EIS)

In the simple direct current method, the resistance can be calculated by dividing voltage and current in Ohm law, *R=V/I*. However, this simple method cannot measure the electrical conductivity of ionic conductor material due to polarization at the interface and the defect region, such as grain boundaries. Using the alternating current (AC) signal, the changing of

impedance Z to the signal frequency is measured, and the sample resistance can be evaluated. It is done by applying voltage, $v(t) = v_0 \sin \omega t$, to the sample results in current $i(t) = i_0 \sin(\omega t + \theta)$, which θ is the phase difference. The impedance of the sample can be expressed by equation (2.26).

$$Z = \frac{v(t)}{i(t)} = \frac{v_0 \sin \omega t}{i_0 \sin(\omega t + \theta)} \tag{2.26}$$

The AC impedance is generally represented by $Z(\omega)$ and considered as complex quantity with real component $Z'(\omega) = |Z| \cos \theta$, and imaginary component $Z''(\omega) = |Z| \sin \theta$. The plot of Z'' to Z' is called the Nyquist plot. In this study, the total resistance of the sample was fitted using EC-Lab software using an equivalent circuit drawn in Figure 2.11.

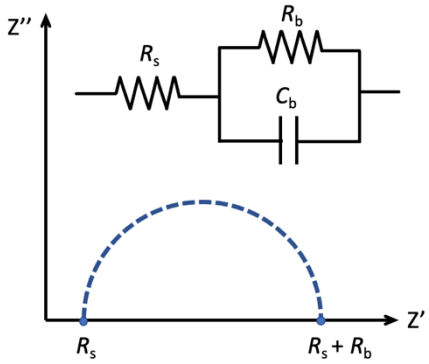

Figure 2.11 The Nyquist plot and the equivalent circuit were adopted to calculate the total resistivity of the sample R_b in this study. The R_s and C_b represent the cell resistance and capacitance, respectively.

From the total resistance, we can calculate the total conductivity of the sample with thickness t and area A as $\sigma = \frac{1}{R} \times t/A$. The total conductivity of the bulk and grain boundary was calculated by considering the approximate capacitance value responsible for the phenomenon in bulk at high frequency (1-20 pF) and grain boundary at low frequency (1-10 nF). The plot of conductivity over temperature is known as the Arrhenius plot.

Chapter 3

A New Family of *p*-block Metal Oxyhydrides $A_3GaO_4H_x$ (A = Ba, Sr)

Abstract

Oxyhydride materials have gained popularity recently due to several exciting characteristics. However, the preparation of oxyhydrides with poor elemental selectivity is one of the challenges for material exploration. A new oxyhydrides containing gallium cation has been successfully synthesized in this study through a solid-state reaction under high-pressure synthesis. Polycrystalline samples of $(Ba,Sr)_{3-y}GaO_4H_{1-x}$($x$=0.22-0.30, y=0.10-0.15) were identified as a new tetragonal phase with *I4/mcm* unit cell from the synchrotron X-ray diffraction (SXRD) and neutron diffraction (ND) pattern analysis. The gray-colored powder sample is unstable in the air. The thermogravimetry (TG) results revealed an oxide ion-exchange ability of $Ba_{2.85}GaO_4D_{0.70}$. Furthermore, the stability range of oxyhydrides in the anti-perovskite structure was provided in this study for the next exploration.

3.1 Introduction

The incorporation of hydrides into oxide material, oxyhydrides, results in several unique physical and chemical properties such as metal to insulator transition under pressure, superconductor, catalyst, and hydride conduction. Despite its attractive properties, the preparation of oxyhydrides with poor elemental selectivity is challenging in material exploration. Among all the reported oxyhydrides are transition metal, rare earth metals, and lanthanide atoms. The oxyhydrides of *p*-block triel element is rare. The *p*-metal element reported having superior properties and application such as semiconductor (GaAs), electrocatalyst (*n*-SnNiFe), photoluminescence, and solar-cell ($CsPbI_2$). In ionic conduction material, *p*-element doping could enhance the ionic conductivity by providing an additional ionic pathway such in lithium conductor LGPS series and facilitate proton conductor $LaBaGaO_4$ [48,49].

One of the overstudied *p*-metal element oxyhydrides is the Mayenite oxide C12A7 ($12CaO.7Al_2O_3$), and S12A7 reported they could be hydride donor after heated to 1300 ^oC in hydrogen gas [50]. The hydride ion is trapped in its cage[7], as shown in Figure 3.1. Upon UV illumination, the hydride dissociates into H^0 and electrons localized at halogen vacancy so-called *F*-center [51]. Its presence can be detected by Electron Paramagnetic Resonance (EPR) spectra measurement. Those electrons contribute to the conduction in microporous crystals. This report shows a promising synthesis of *p*-block elements.

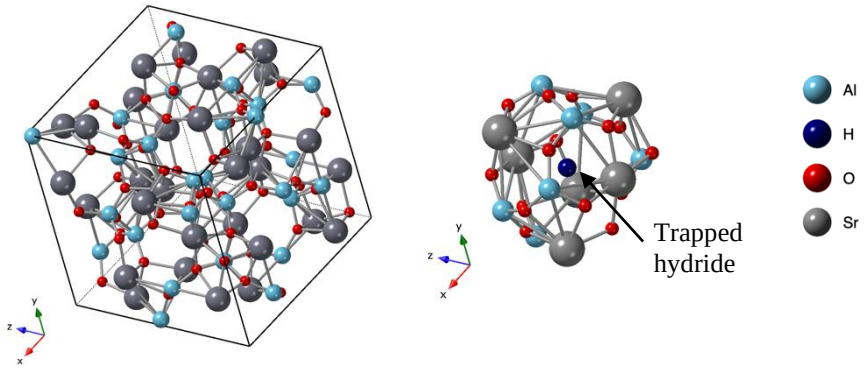

Figure 3.1 The crystal structure of Mayenite oxide, C12A7 (left) similar to S12A7 and its cage structure with hydride ion trapped inside (right).

Other reported Al-containing oxyhydrides are Ba_3AlO_4D and Sr_3AlO_4H. Despite having similar chemical formula and relatively similar ionic radius of Ba^{2+} (1.42Å) and Sr^{2+} (1.42Å), they have different structures. The Ba_3AlO_4D was reported to have an orthorhombic *Pnma* structure and Sr_3AlO_4H having a tetragonal *I4/mcm* structure [8,52]. Both structures consist of AlO_4 tetrahedra with different ordering and orientation, resulting in a different structure, where the octahedra of Ba_6D is strongly distorted in Ba_3AlO_4D, see Figure 3.2.

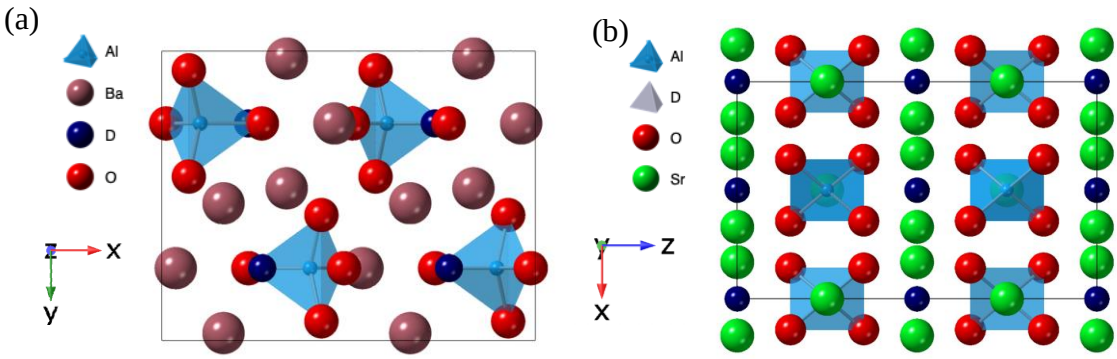

Figure 3.2 Crystal structure of (a) Ba_3AlO_4D and (b) Sr_3AlO_4H.

Many transitions metal, alkaline, and alkaline earth metal oxyhydrides have been studied, but less study in *p*-element metal oxyhydrides. The C12A7 oxyhydride with a strong tendency of covalency of p-element shows the reversible hydrogen incorporation originates electronic conduction. Later, Al-oxyhydrides, Sr_3AlO_4H was reported stable adopting anti-perovskite structure with *I4/mcm* space group.

The aim of the topic (a) is to gain the crystal chemistry knowledge of *p*-element metal oxyhydrides. First, we synthesized the oxyhydrides A_3GaO_4H (A=Ba, Sr) and investigated their structure and thermal stability. Then, the stability regions *p*-element metal oxyhydrides A_3AlO_4H, A_3GaO_4H (*A*=Ba,Sr) with an anti-perovskite structure were obtained for the first time.

3.2 Experimental

3.2.1 High-Pressure Synthesis of $A_3GaO_4H_x$

Polycrystalline samples of $A_3GaO_4H_x$ (*A* = Ba, Sr) were prepared by heating the stoichiometric mixtures of AH_2 (99.5%, Mitsuwa Chemical Co.), *A*O (99.99%, Aldrich), and Ga_2O_3 (99.99%, Aldrich) under high pressure. The stoichiometric raw materials were mixed using planetary ball milling Premium line Pulverized Fritsch in the 20 mL Zirconia (ZrO_2) jar with 80 balls with 5 mm diameters. The optimization of the ball milling process was done and resulted in 600 rpm as the optimum conditions refer to the purity of the final product. The mixed powder of raw materials was pressed into pellets with a size about 5 mm in diameter and assembled into a BN sleeve, NaCl sleeve, and pyrophyllite cell. The cell was pressed under 2 GPa using cubic anvil apparatus and heated up to 800 ^oC for 30 minutes before finally quenched into room temperature, following by slowly releasing the pressure.

After the synthesis, the phase identification was performed using a laboratory X-ray diffractometer Rigaku MiniFlex 600. The detailed structure was investigated by the Synchrotron X-ray diffraction data collected at BL02B2, SPring-8. Neutron diffraction (ND) data of the deuterated sample was collected in SPICA, J-PARC to confirm the presence of hydrogen in the sample with an auto-sample changer environment that allowed sample rotation during neutron collection. The sample was mounted in a 6-mm-diameter V-Ni can filled with Ar-gas. In addition, the sample stability was confirmed using thermogravimetry, where the changing of sample mass on the Al-pan holder was recorded during heating and cooling under O_2 and Ar gas flow.

3.3 Results and Discussion

3.3.1 X-ray Difraction Pattern

The initial phase identification was performed by using laboratory XRD. The XRD pattern in Figure 3.3 revealed a new phase that could be indexed well with a tetragonal unit cell with lattice parameters *a* and *c* are 7.3280(1) Å and 11.7278(2) Å, respectively for Ba_3GaO_4H. The XRD pattern is similar to Sr_3AlO_4H reported by Matsuishi [52]. A small amount of raw material, SrO, remains in the Sr_3GaO_4H sample.

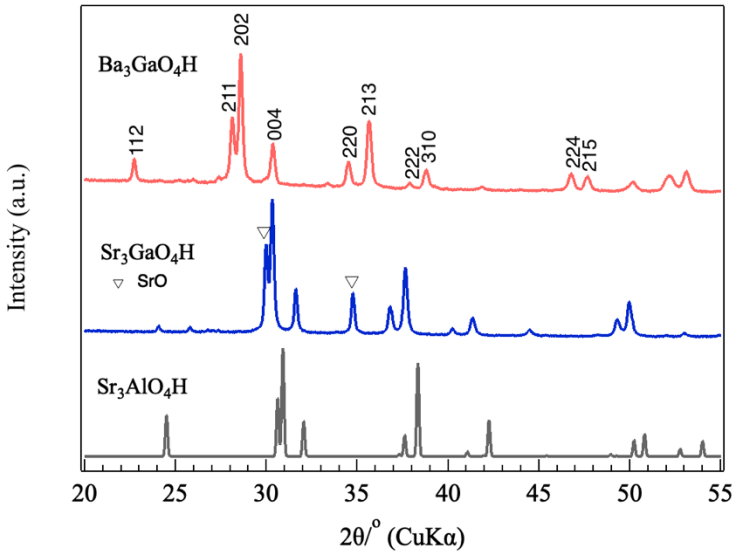

Figure 3.3 The laboratory XRD pattern of Ba_3GaHO_4H and Sr_3GaO_4H.

3.3.2 Sensitive Synthesis Condition

One of the critical conditions in the synthesis of $A_3GaO_4H_x$ (A = Ba, Sr) is the initial ball milling condition of the raw materials. Some of the ball-milling conditions had been varied to check its effect of stabilizing the phase. The varied parameters in the ball-milling process include the balls and pot material, the rotation speed, and time. In Figure 3.4(a), the raw

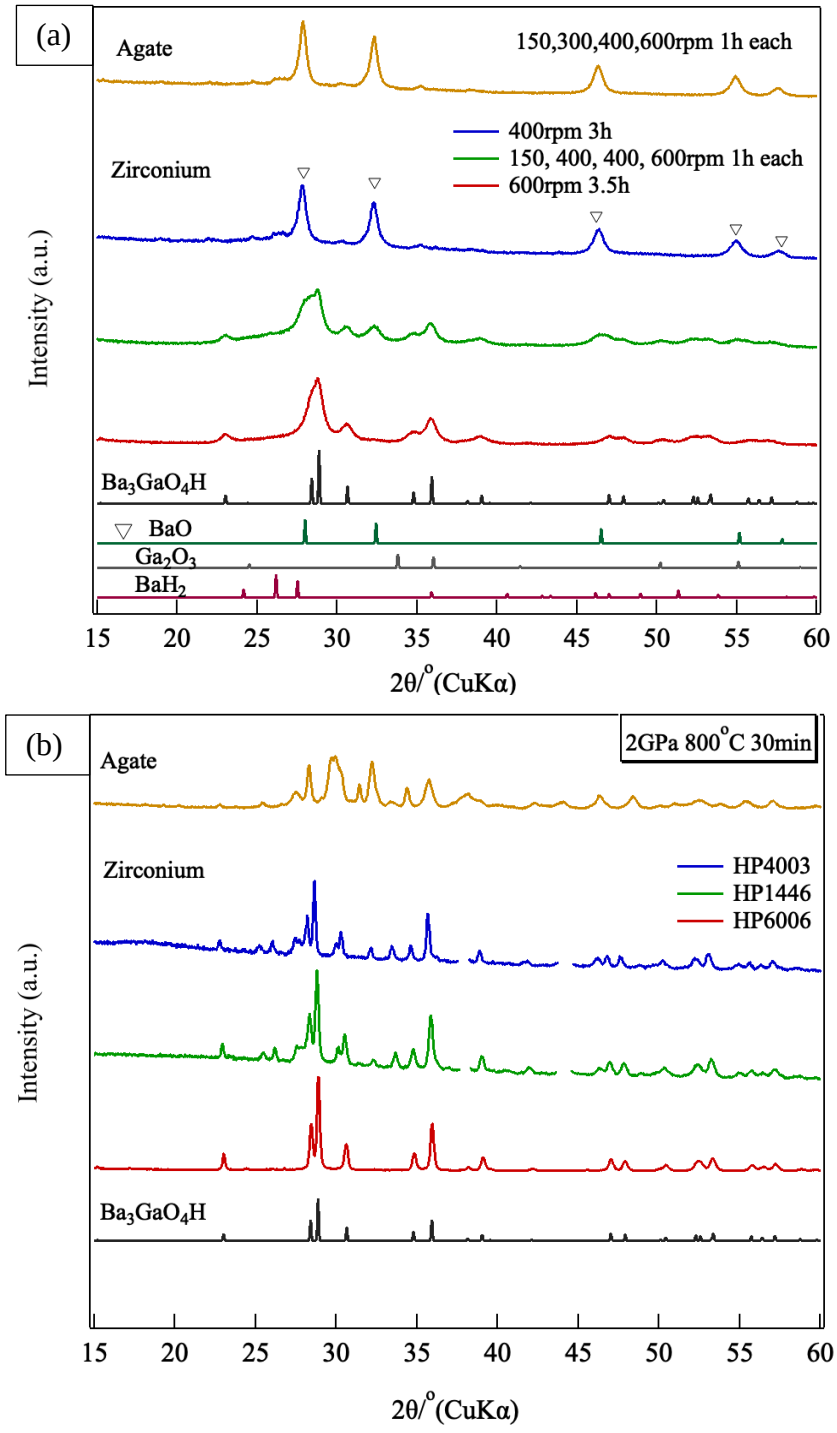

Figure 3.4 The XRD pattern of (a) mixed BaH_2+BaO+Ga_2O_3 after ball-milling and (b) after sintering under high-pressure.

materials of Ba_3GaO_4H after ball-milling under low ball milling energy condition such in the Agate and Zirconia at 400 rpm shows the oxide phase remains. The oxide phase of the raw materials starts to disappear at a higher speed of Zirconia ball-milling until it completely disappears after ball-milling under 600 rpm. The XRD pattern is similar to the expected phase Ba_3GaO_4H with a broad profile. It suggests that the main phase is already stable after the ball-milling process. After sintering under high-pressure 2 GPa and 800 ^oC, the XRD pattern in Figure 3.4(b) shows obvious different and nearly pure samples obtained under high energy ball-milling, Zirconia, and 600 rpm, concluded that ball-milling is necessary to stabilize this sample.

3.3.3 The Synchrotron X-Ray Diffraction (SXRD)

The SXRD experiment was performed at BL02B2 SPring-8 to investigate the detailed structure of the $A_3GaO_4H_x$ (A = Ba, Sr), The refinement of the SXRD data adopting the crystal model of Sr_3AlO_4H results in acceptable fitting parameters for both samples. The refined pattern is plotted in Figure 3.5.

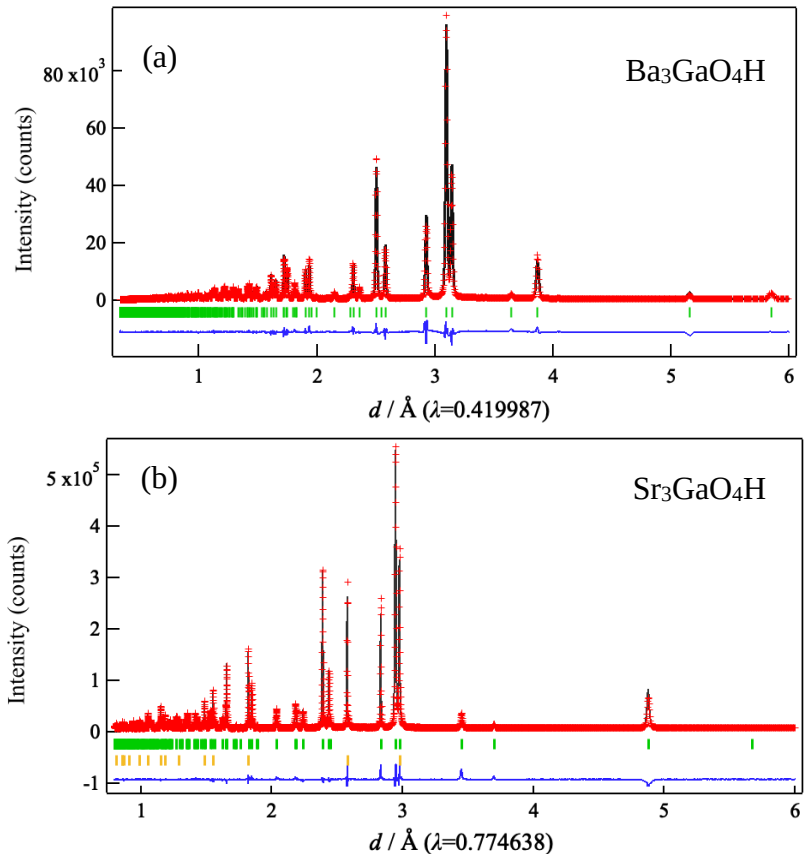

Figure 3.5 The refined SXRD pattern of (a) Ba_3GaO_4H and (b)Sr_3GaO_4H. The red mark, black and blue pattern are the experimental pattern, the calculated pattern, and the difference pattern. The green tick marks indicate the main phase. The yellow tick mark on the Sr_3GaO_4H represents the SrO (18.7 wt%).

Table 3.1 Refined crystal structure parameters from SXRD data of Ba_3GaO_4H and its calculated BVS.

atom	site	*g*	*x*	*y*	*z*	*B*/Å^2	BVS
Ba1	4*a*	0.92916(6)	0	0	0.25	1.333(8)	1.42
Ba2	8*h*	1	0.17327(2)	0.67315(2)	0	0.547(5)	2.16
Ga	4*b*	1	0	0.5	0.25	0.626(11)	2.38
O1	16*l*	1	0.1487(2)	0.6487(2)	0.6520(1)	2.50(4)	1.68

Ba_3GaO_4H Unit cell: Tetragonal *I4/mcm*; *a*=*b*=7.29616(3)Å, *c*= 11.70656(6)Å,
S=2.48, R_{wp} = 7.49%, R_p=5.21%, R_e=3.02%, R_B= 4.34%, R_F=3.27%.

Table 3.2 Refined crystal structure parameters from SXRD data of Sr_3GaO_4H and its calculated BVS.

Phase 1: Sr_3GaO_4H (82.3 wt%)

atom	site	*g*	*x*	*y*	*z*	*B*/Å^2	BVS
Sr1	4*a*	0.9219(5)	0	0	0.25	0.892(11)	1.32
Sr2	8*h*	1	0.17310(3)	0.67310(3)	0	0.130(7)	2.03
Ga	4*b*	1	0	0.5	0.25	0.389(10)	2.53
O1	16*l*	1	0.15529(8)	0.65529(8)	0.64920(6)	1.86(2)	1.70

Sr_3GaO_4H, Unit cell: Tetragonal *I4/mcm*; *a*=*b*=6.901414(5) Å, *c*= 11.341604(10)Å,
S=6.82, R_{wp} =5.98%, R_p=3.98%, R_e=0.88%, R_B= 5.31%, R_F=3.24%.

Phase 2: SrO (18.7% wt%)

atom	site	*g*	*x*	*y*	*z*	*B*/Å^2
Sr1	4*b*	1	0.5	0.5	0.5	0.29
O1	4*a*	1	0	0	0	0.34

SrO, Unit cell: Cubic *Fm-3m*; *a=5.157548(2),* R_B= 3.42%, R_F=2.01%.

The refinement of the XRD pattern suggests that the crystal model's framework is acceptable, with small barium occupancy likely exist. This structure is a layered structure of $AGaO_4$ and A_2H or also can be explained as an anti-perovskite structure with expected hydrogen occupy the (0,0,0) site or the center of Ba_6-octahedral, see Figure 3.6. As listed in Table 3.1, Ba1 and Ba2, two barium sites have different environments. The Ba1 site has a large temperature factor and shows a tendency of small vacancies exist, opposite to the Ba2 site. The BVS calculation [53] also revealed that the Ba1 site is under bonding, indicating that the Ba1 site size is larger than the ionic size of Ba. The tendency to under-bonding Ba1 site also appeared in strontium sample, in Table 3.2, with Sr1 being under-bounded. Therefore, there is a possibility of local ordering in this structure. The neutron diffraction experiment was performed to investigate further the crystal structure and the hydrogen existence in the structure.

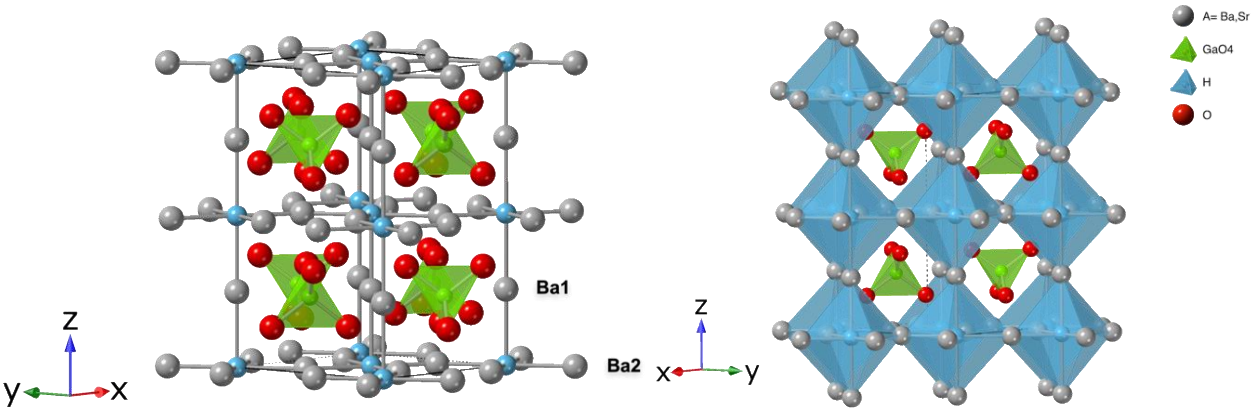

Figure 3.6 The crystal structure of A_3GaO_4H (A = Ba, Sr) drawn as layered structure and anti-perovskite structure. The green tetrahedral represents GaO_4. Gray balls represent Ba. Blue balls represent the expected position of hydrogen.

3.3.4 Presence of Hydrogen

The presence of hydrogen in the structure of A_3GaO_4H (A = Ba, Sr) was investigated on the deuterated sample using neutron diffraction experiment at room temperature at BL09 SPICA, J-PARC. The deuterated sample of Ba_3GaO_4H was prepared using a similar synthesis route. The contribution of incoherence scattering of hydrogen appeared as a higher background level of Ba_3GaO_4H compared to Ba_3GaO_4D, as can be seen in Figure 3.7. The relative intensity of those two patterns also different as evidence that hydrogen exists in the structure.

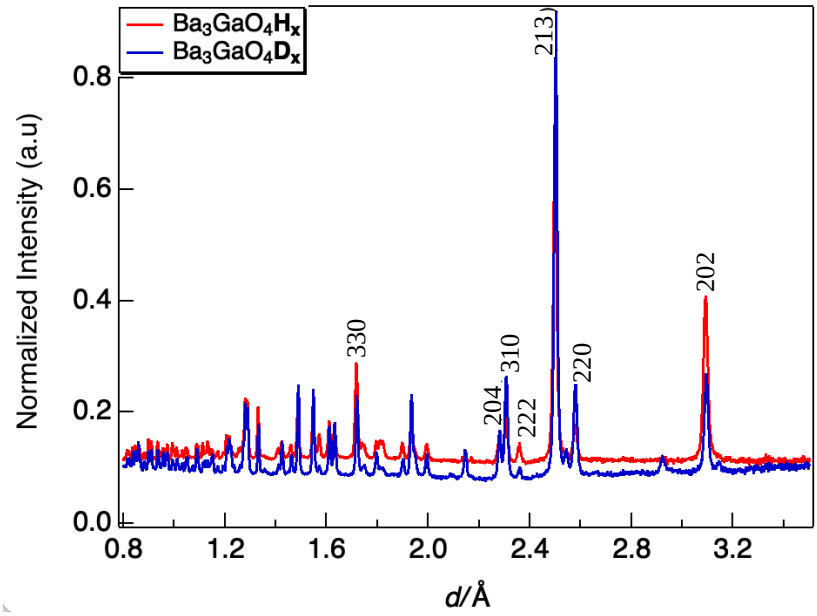

Figure 3.7 The normalized histogram data of Ba_3GaO_4H and Ba_3GaO_4D collected at BL09-Spica at room temperature.

To estimate how much hydrogen occupancy (g) in Ba_3GaO_4H, the ND simulation patterns were calculated with g varied from 0,0.5 to 1 of the expected hydrogen sites, 4*c* (0,0,0). The simulation pattern in Figures 3.8 suggested that the hydrogen is not fully occupied. The relative intensity in the pattern of g = 0.5 is close to the experimental data of ND. It revealed that the hydrogen is partly occupied.

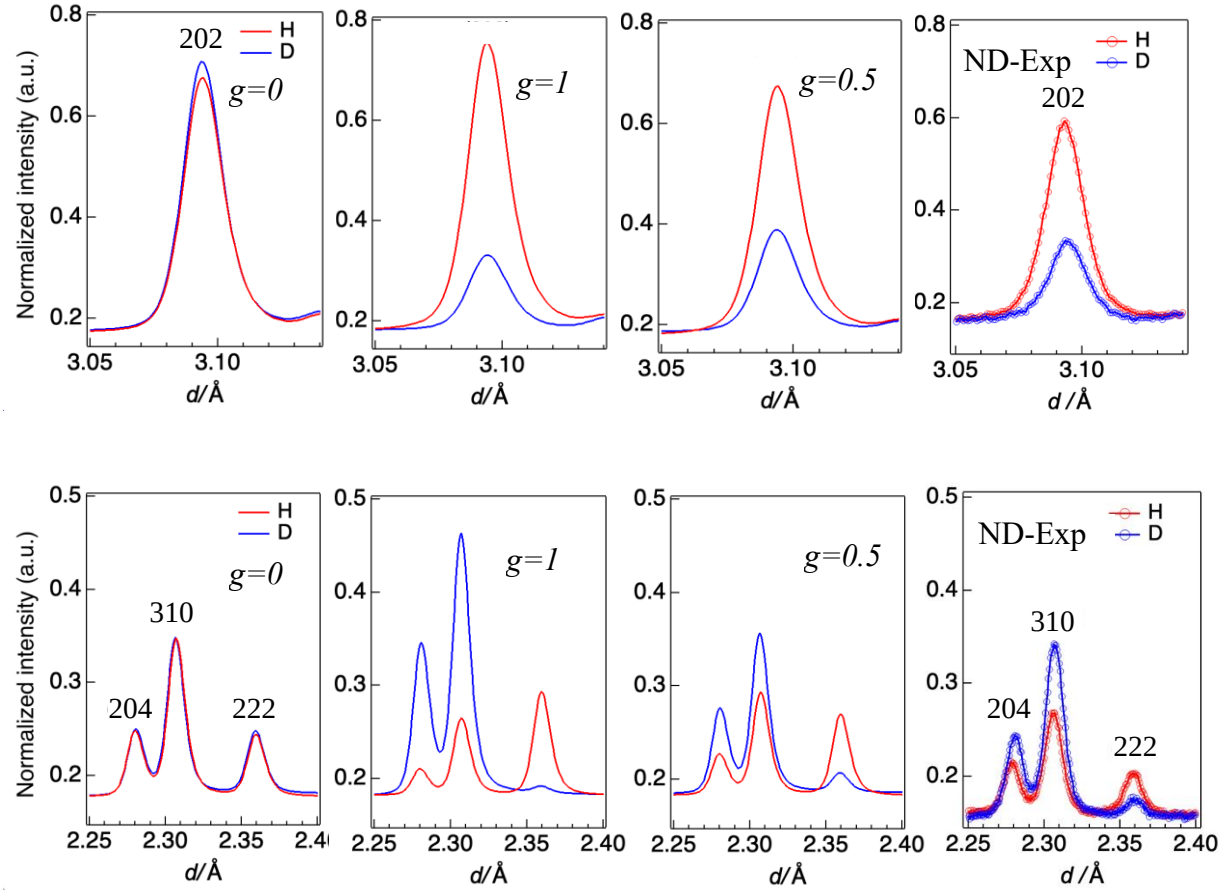

Figure 3.8 The ND simulation pattern of (202) peak of (a) g = 0, (b) g = 1, and (c) g = 0.5 and (204), (310), (222) peaks of (e) g = 0, (f) g = 1, and (g) g = 0.5 compared to (d) (f) its normalized ND experimental data, respectively.

3.3.5 Neutron Diffraction

The ND diffraction pattern of Ba_3GaO_4D and Sr_3GaO_4D is refined refer to the framework from SXRD refinement results to determine the occupancy of hydrogen and the estimated composition of Ba_3GaO_4H by adding hydrogen sites, 4*c* (0,0,0). The Rietveld refinement profile of the deuterated sample is presented in Figure 3.9.

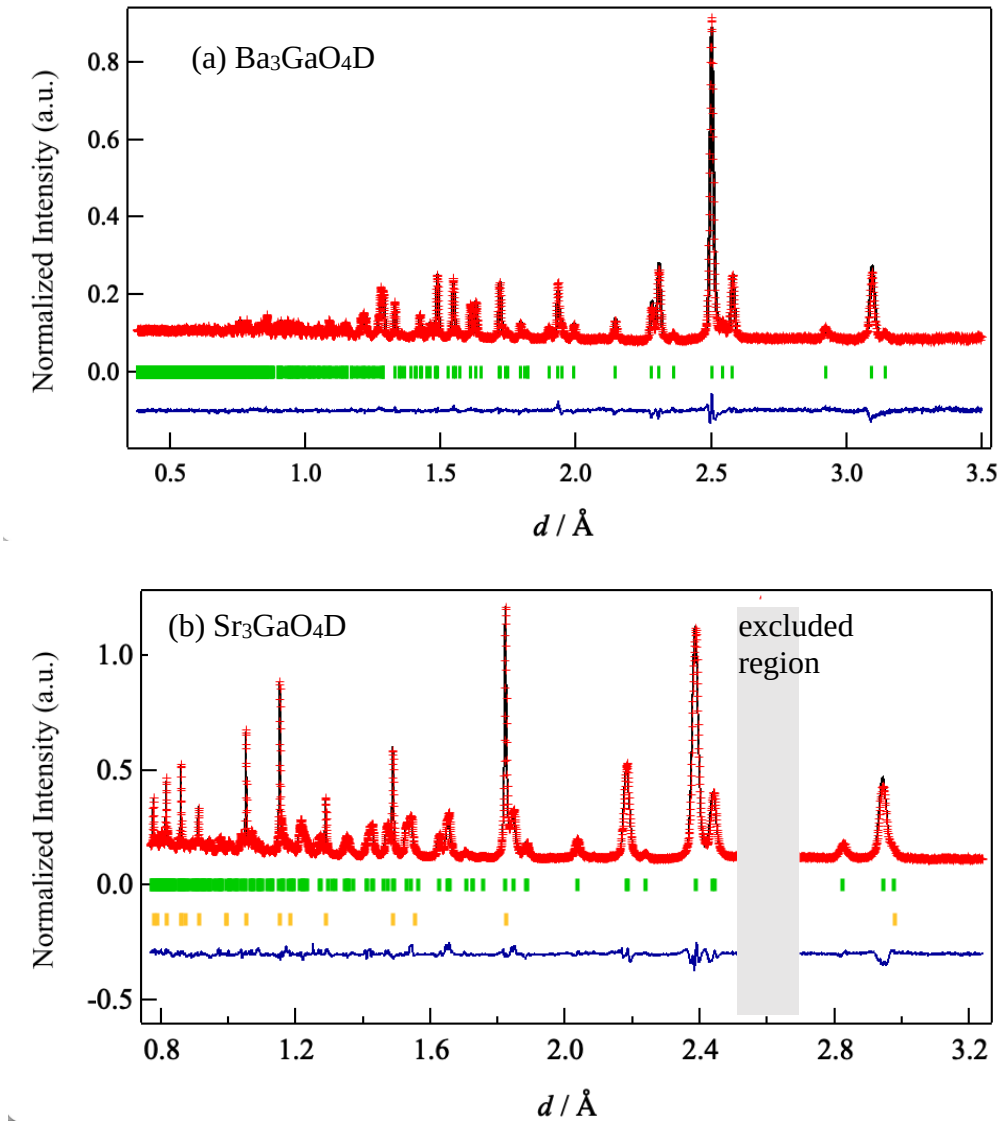

Figure 3.9 The refined ND pattern of (a) Ba_3GaO_4D and (b)Sr_3GaO_4D. The red mark, black and blue pattern are the experimental pattern, the calculated pattern, and the difference pattern. The green tick marks indicate the main phase, whereas the yellow tick mark on the Sr_3GaO_4H represents the SrO.

The Rietveld refinement profile of the Ba_3GaO_4D resulted in the tetragonal structure *I*4/*mcm* that confirmed hydrogen position at 4*c* (0,0,0) sites. The ND data also suggest Ba vacancy compensating the partial hydrogen occupancy. In Sr_3GaO_4D, the sample quality of the deuterated sample is different from the hydrogen sample due to the different quality of raw material. The ND refinement assuming an average structure is quite acceptable. The diffraction data revealed the possibility of lowering symmetry, but we will not discuss the detail in this report and accept the average structure as tetragonal *I*4/*mcm*.

Table 3.3 Refined crystal structure parameters from ND data of Ba_3GaO_4H and its calculated BVS.

Phase: $Ba_{2.8496(4)}GaO_4D_{0.699(3)}$

atom	site	*g*	*x*	*y*	*z*	*B*/Å^2	BVS
Ba1	4*a*	0.8496(14)*	0	0	0.25	0.78(2)	1.32
Ba2	8*h*	1	0.17489(6)	0.67489(6)	0	0.191(12)	2.15
Ga	4*b*	1	0	0.5	0.25	0.239(14)	2.94
D	4*c*	0.699(3)	0	0	0	1.45(3)	1.42
O1	16*l*	1	0.13914(4)	0.63914(4)	0.65098(4)	1.130(9)	1.78

*The refinement of *g* was constrained to fulfil the charge balance.

Unit cell: Tetragonal *I*4/*mcm*; *a*=*b*=7.29261(4)Å, *c*= 11.68652(10)Å,

S=1.67, R_{wp} = 2.44%, R_p=2.07%, R_e=1.46%, R_B= 5.39%, R_F=5.60%.

Table 3.4 Refined crystal structure parameters from ND data of Sr_3GaO_4H and its calculated BVS.

Phase 1: $Sr_{2.8933(11)}GaO_4D_{0.787(2)}$ (68.54 wt%)

atom	site	*g*	*x*	*y*	*z*	*B*/Å^2	BVS
Sr1	4*a*	0.8933(11)*	0	0	0.25	1.129(15)	1.20
Sr2	8*h*	1	0.17329(4)	0.67329(4)	0	0.079(7)	2.04
Ga	4*b*	1	0	0.5	0.25	0.094(11)	3.06
H	4*c*	0.787(2)	0	0	0	2.06(3)	1.14
O1	16*l*	1	0.14399(5)	0.64399(5)	0.64637(5)	2.055(11)	1.80

*The refinement of *g* was constrained to fulfil the charge balance.

Unit cell: Tetragonal *I*4/*mcm*; *a*=*b*=6.89829(4) Å, *c*= 11.29522(13)Å,

S=3.98, R_{wp} =4.20%, R_p=2.99%, R_e=1.05%, R_B= 7.07%, R_F=6.25%.

Phase 2: SrO (31.46 wt%)

atom	site	*g*	*x*	*y*	*z*	*B*/Å^2
Sr1	4*b*	1	0.5	0.5	0.5	0.485(7)
O1	4*a*	1	0	0	0	0.509(8)

SrO, Unit cell: Cubic *Fm-3m*; *a*=5.58083(6) R_B= 4.41%, R_F=3.07%.

The fitting parameters summarized in Table 3.2 and Table 3.3 indicate that the refinement is acceptable for both data. The ND confirmed that hydrogen exists in the samples, with partial vacancy, giving the estimated composition of $Ba_{2.85}GaO_4D_{0.70}$ and $Sr_{2.89}GaO_4D_{0.79}$. The partial occupancy in the oxyhydrides is typical, especially for the material prepared by the quenching method. The temperature factor of Ba1 and Sr1 from this refinement also showing relatively large in agreement with those results of SXRD. Supported by the relatively low BVS value

indicates Ba1 and Sr1 site is under bounding. The under-bonding state of the Ba1 site is also reported in other isostructural compounds, as listed in Table 3.5. The pair distribution function study of the $LaSr_2AlO_5$ explained that the under-bonding of the 4*a* site is due to the local distribution of Sr-O that is indistinguishable in the diffraction data [54].

Table 3.5 BVS calculation of 4*a* site of some isostructural compounds with *I*4/*mcm* structure.

Compound	**Site 4*a***	**BVS**
Sr_3GaO_4F [55]	Sr	1.3
Sr_3AlO_4H [52]	Sr	1.4
$LaSr_2AlO_5$ [54]	Sr	1.3

3.3.6 Sample stability and TG of $Ba_{2.85}GaO_4H_{0.70}$

Regarding the stability of $Ba_{2.85}GaO_4H_{0.70}$, the X-ray diffraction measurement was performed in air using laboratory XRD Rigaku MiniFlex 600. The XRD patterns indicate that the sample was decomposed into oxide phases within one minute of air exposure.

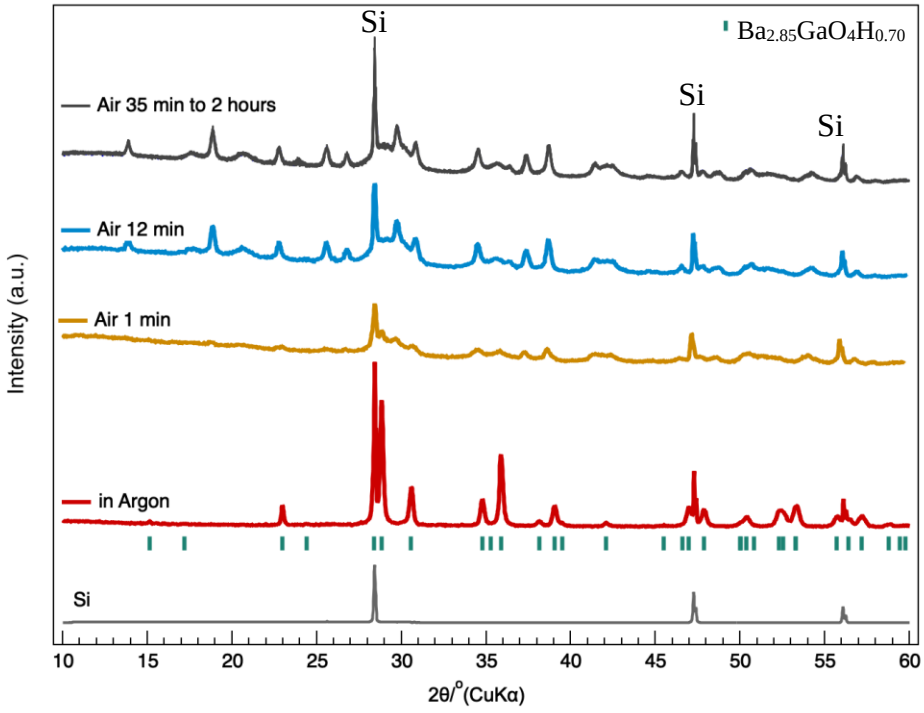

Figure 3.10 Laboratory X-ray diffraction of $Ba_{2.85}GaO_4H_{0.70}$ stability in air. The red line pattern is the initial pattern of $Ba_{2.85}GaO_4H_{0.70}$ mixed with Si powder as a reference. The sample decomposed right after contact with air.

The thermogravimetry (TG) were also done using Rigaku Thermo Plus 8121 with a heating rate of 5 ^{o}C/min up to 500 ^{o}C to check the thermal stability of the $Ba_{2.85}GaO_4H_{0.70}$ under both Ar and O_2 flow. During heating under argon gas flow, an infinitesimal mass gain was observed that might indicate hydrogen release from the structure. Due to the lightness of the hydrogen atom, the changing of mass is difficult to observe. Calculation mass loss of TG if hydrogen is completely evaporated is about 0.1%. On the other hand, during heating under O_2 gas flow, the significant mass gain was observed ~2.2%, as shown in Figure 3.9(a). It indicates the capability for H^-/O^{2-} exchange.

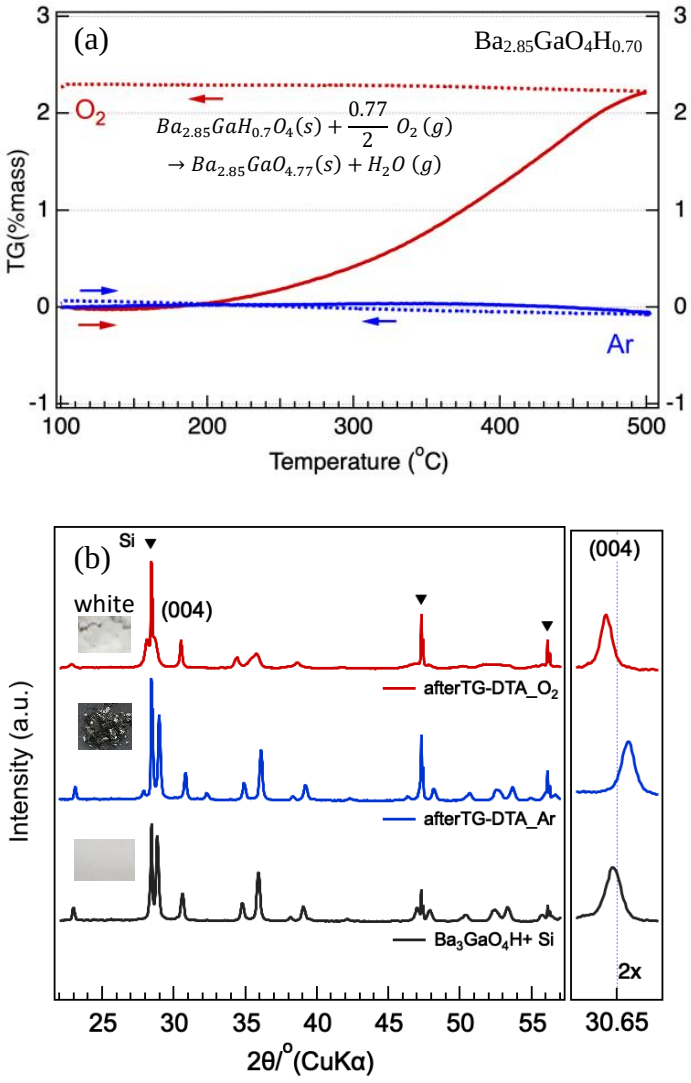

Figure 3.11(a) TG curve of $Ba_{2.85}GaO_4H_{0.70}$ measured under Ar and O_2, and (b) the XRD pattern of the sample after TG measurement mixed with Si powder as reference.

The XRD patterns of the $Ba_{2.85}GaO_4H_{0.70}$ revealed that the sample framework is stable after TG with observed peak shifting. After heating under Ar gas flow, the lattice volume shrinkage by ~1.3%. In contrast, the lattice volume expansion of ~2% was observed after heating under oxygen flow. It may be explained that hydrogen released induced volume reduction, while oxygen incorporation induced volume expansion in agreement with TG results. The detailed lattice parameters changes are listed in Table 3.6. Oxygen conduction was reported in this type of structure as in $BaLa_2ZnO_5$ [56]. The partial oxygen occupancy after H^-/O^{2-} exchange may potentially enhance the conduction property.

Table 3.6 Lattice parameters change of $Ba_{2.85}GaO_4H_{0.70}$ after TG.

$Ba_{2.85}GaO_4H_{0.70}$	**Lattice Parameters**				
	***a* = *b* (Å)**	**c (Å)**	**Δa**(%)	**Δc(%)**	**Δ*V*(%)**
After TG (O_2)	7.35751(16)	11.70467(40)	+0.92	+0.20	+2
After TG (Ar)	7.26559(10)	11.6019(2)	-0.34	-0.68	-1.3
Before TG	7.29053(25)	11.6813(4)			

3.3.7 Synthesis route consideration on oxyhydride synthesis

Generally, the synthesis of oxyhydride requires a high reductive environment, and the reaction should occur without transferring an electron from hydrogen [2], given its electronegativity 2.1. In the solid-state reaction synthesis of oxyhydrides, the metal hydride materials are the hydride source other than hydrogen gas, which creates a reductive environment. Meanwhile, the hydrogen itself has the two most possible stable states as a proton, H^+, when it reacts with electronegative atoms or H^- when it reacts with electropositive atoms [1]. Therefore, in the oxyhydride synthesis, an electropositive atom, in this report Ba and Sr, takes an essential role in avoiding electron transfer from hydrogen during the synthesis.

The *p*-block element atoms have diverse characters, both properties and reactivity. In this study, oxyhydride containing gallium ion is reported. Gallium is known for its semiconductor property as in its oxide Ga_2O_3 is a wide-gap semiconductor material. The heating of Ga_2O_3 in a reductive condition result in gallium metal due to the unavoidable electron transfer from hydrogen to gallium. Gallium hydride compounds, including GaH_3 (gallane), is known as an unstable compound [57]. Gallane compounds prepared by hydrogenation of the Zintl phase are also unstable at ambient conditions [58]. This study revealed that the gallium oxyhydrides preparation through high-pressure synthesis and quenching could stabilize its metastable phase at ambient pressure. Some unknown peaks were

observed in the initial synthesis, attributed to the unknown metal phase as gallium is easy to form metal at reductive conditions during heating as it also has a low melting point. Therefore, the synthesis route by avoiding heating is considered at the first step through ball milling, mechanical force, using planetary ball milling and relatively hard balls and pot material, ZrO, and a speed as high as 600 rpm. In a relatively high-energy ball milling process, the primary energy to initiate the reaction is expected to come from a mechanical collision between particles. A 30-minute rest was set for each 3 minutes milling cycle to anticipate the heat effect. The reaction is already initiated during the ball milling process which the rate of reaction is simply a relation of the collision frequency between particles. The ball could remove the product layers and stir the mixture well for a homogeneous reaction. The preparation of oxyhydrides through two synthesis routes, mechanochemical and high pressure, has not been reported.

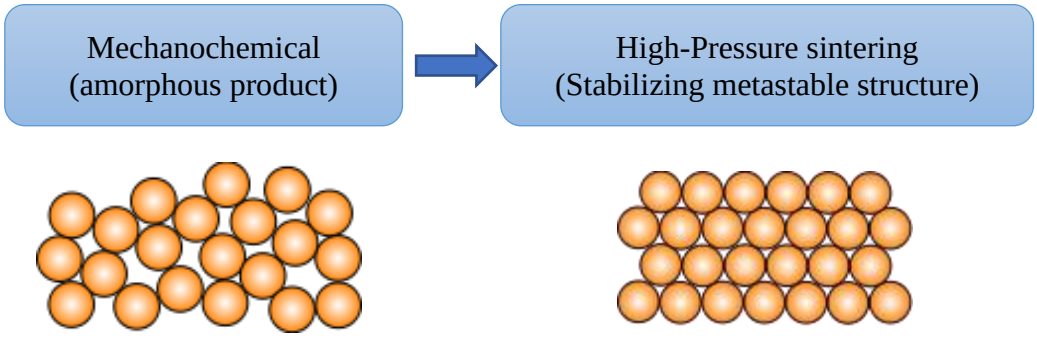

Figure 3.12 Two root step synthesis of metastable oxyhydrides phase A_3GaHO_4 (*A*=Ba.Sr).

3.3.8 Structure stability and H^-/O^{2-} exchangeability

Many oxyhydrides are reported unstable due to the reaction of hydride with moisture releasing hydrogen gas. Hydrogen gas is also released upon heating. The BVS of $Ba_{2.85}GaO_4D_{0.70}$ suggested the distribution of dense and loose layers in the structure. The local structure most likely exists in the loose layer, Figure 3.13, as reported in the similar structure [54]. Incorporating oxygen on the denser layer changes the lattice parameter significantly in the *a*-axis, which may induce different local ordering. In this study, only diffraction data were collected; therefore, explaining local ordering is not possible.

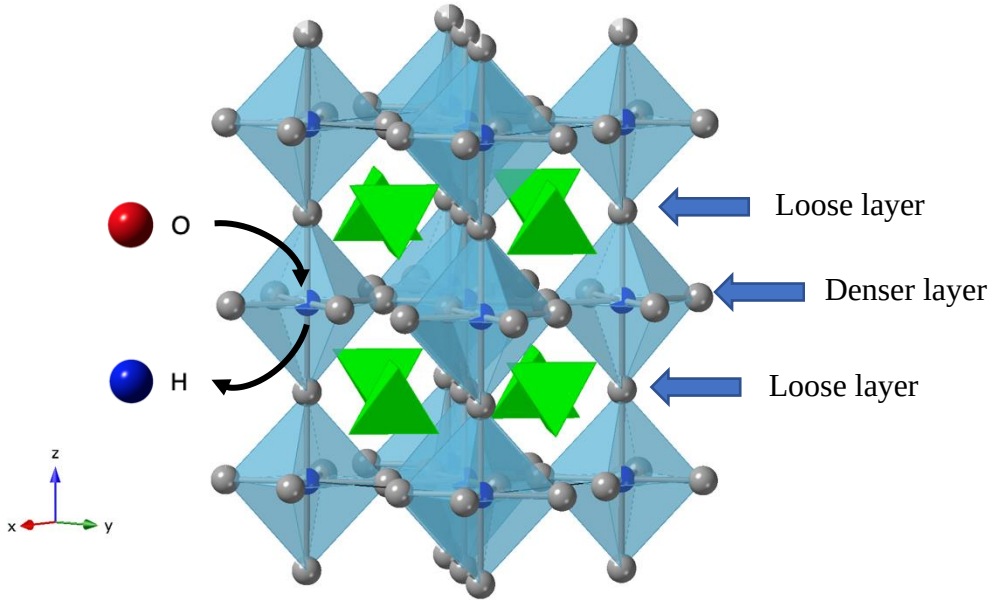

Figure 3.13 Structural illustration of the different layered density of atoms.

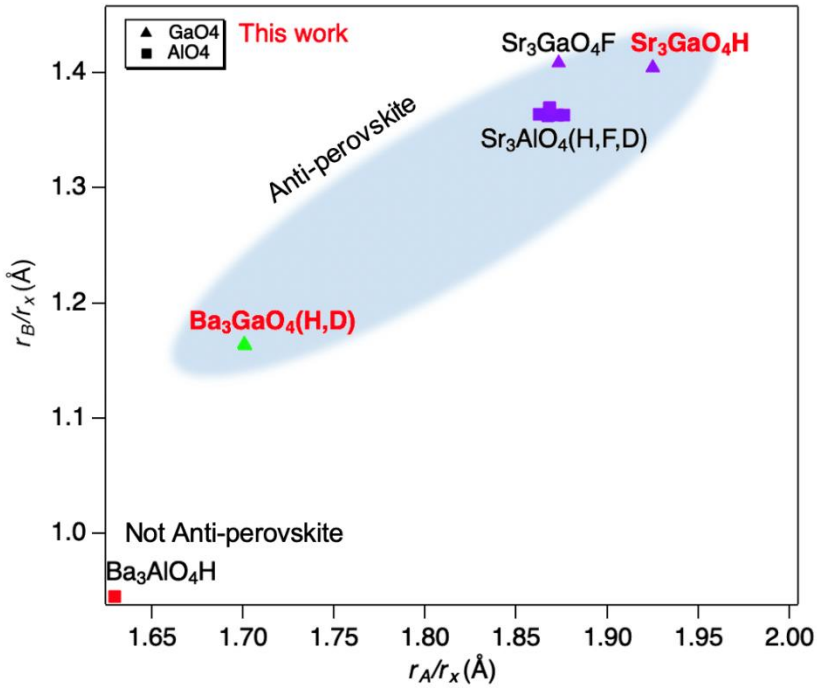

Figure 3.14 The summary of anti-perovskite gallium oxyhydrides and its reported isostructural oxyfluorides for structure prediction.

By adopting the perovskite structure ABX_3, the tendency of oxyhydride stability in an anti-perovskite structure was obtained by comparing the ionic radius ratio, Figure 3.14. In the ABX_3 perovskite structure, the *A* represents GaO_4 and AlO_4. The *B* represents H, F, or D, and *X* represents the cation, Ba, and Sr. Summarizing this work and other reported, GaO_4 and AlO_4

containing oxyhydrides could expand the material exploration on anti-perovskite oxyhydrides. The oxyhydrides material shows a wider stability area compared to oxyfluoride reveals the flexibility of hydrides. Furthermore, this plot can be used as structure prediction, which is by tuning the size of *B* cation obtaining a new anti-perovskite oxyhydride is possible.

3.4 Conclusion

In the term of material exploration, the first report of Ga-oxyhydrides was successfully synthesized under high pressure. The neutron diffraction refinement results indicated non-stoichiometric compositions of $(Ba,Sr)_{3-y}GaO_4H_x$ (x=0.22-0.30, y=0.10-0.15). It adopted an anti-perovskite structure with GaO_4 and $(Ba, Sr)_6H$ and vacancies ordered in the structure. Although $Ba_{2.85}GaO_4H_{0.70}$ is unstable in the air, it shows the H^-/O^{2-} exchangeability upon heating under dry oxygen flow resulted in a non-stoichiometry oxide phase enhance the oxide conduction in this structure. Anti-perovskite oxyhydrides, consisting of GaO_4 and AlO_4 units, were reviewed and gave an anti-perovskite structure prediction of *p*-element oxyhydrides exploration.

Chapter 4

Structural Study of Super-hydrides Conductor Ba_2LiD_3O

Abstract

A super-hydrides conductor $Ba_{1.75}LiH_{2.7}H_{0.9}$ (BLHO) was reported by Takeiri *et al.* having conductivity ~10^{-2} $S \cdot cm^{-1}$ at 320–350 ºC. The Arrhenius plot shows jump conductivity attributed to its phase transitions. This study aims to gain new insight into the hydride conduction mechanism in the superionic phase of the deuterated sample, BLDO. The Rietveld analysis of the high-temperature neutron diffraction data and MEM calculation discovered interstitial hydride sites at rock-salt and perovskite layers labeled as H3 and H4, respectively. A significant anisotropic temperature factor of lithium sites was observed, indicating the strong ionic correlation between lithium and hydride in the perovskite layer that may result in the presence of H4 sites. Thus, a new conduction mechanism is proposed taking into account the presence of the interstitial site. The main contribution to the conductivity is likely ascribed to the equatorial hydrides concentrated in the perovskite layer. The interstitial sites shorten the distance between carriers implying strong carrier correlation results in superionic behavior.

4.1 Introduction

Recent news reported $Ba_{1.75}LiH_{2.7}H_{0.9}$ (BLHO) shows superionic phase with conductivity ~10^{-2} $S \cdot cm^{-1}$ at 320–350 ºC [19]. At room temperature, the BLHO has a K_2NiF_4-type structure with an orthorhombic $Pmn2_1$ spacegroup due to apical anion ordering. The room temperature structure drawn in Figures 4.1 shows that this structure has three kinds of anion and cation ordering:

1. The ordering of hydrides and vacancies, H_{eq}/V_{eq} at the equatorial sites.
2. The ordering of hydrides and oxygen at the apical sites, H_{ap}/O_{ap}.
3. The ordering of Ba/*V* at the barium sites.

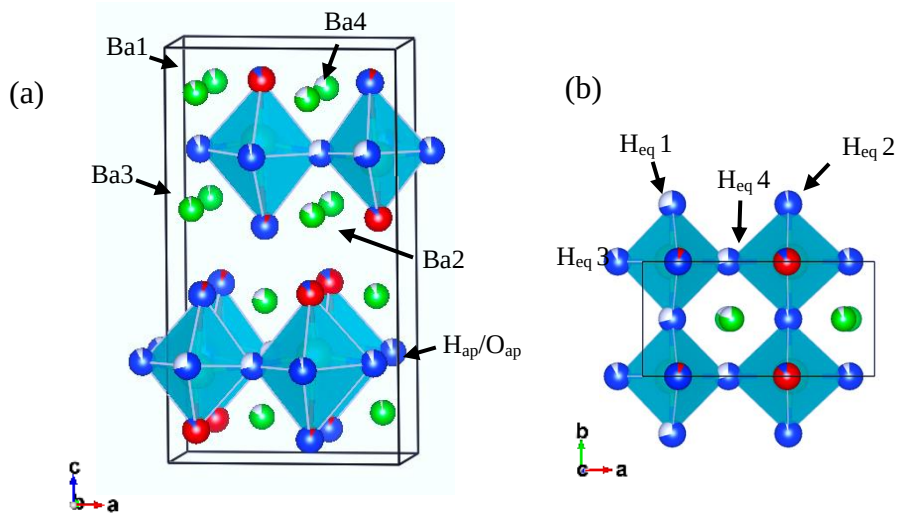

Figure 4.1 Crystal structure of BLHO at room temperature [19].

The temperature-dependent ND study of BLHO performed at BL21 NOVA, J-PARC, revealed the phase transitions of BLHO. Figure 4.2 illustrates the two-phase transitions between room temperature to 350 ^{o}C. The first phase transition, the transition from β-phase to γ-phase, occurred around 300 ^{o}C. This transition was indicated by vanishing the ordering of equatorial hydrides and barium sites but remaining the apical sites ordering. The second phase transition was the transition from γ-phase to δ-phase, which occurred around 340 ^{o}C. Upon heating above 340 ^{o}C, it formed a disordering structure, including the disordering of apical hydride and oxide retaining the four-fold symmetry and tetragonal unit cell with I4/*mmm* spacegroup symmetry. These order-disorder phase transitions resulted in a conductivity jump to a superionic phase at high temperatures, γ-phase and δ-phase.

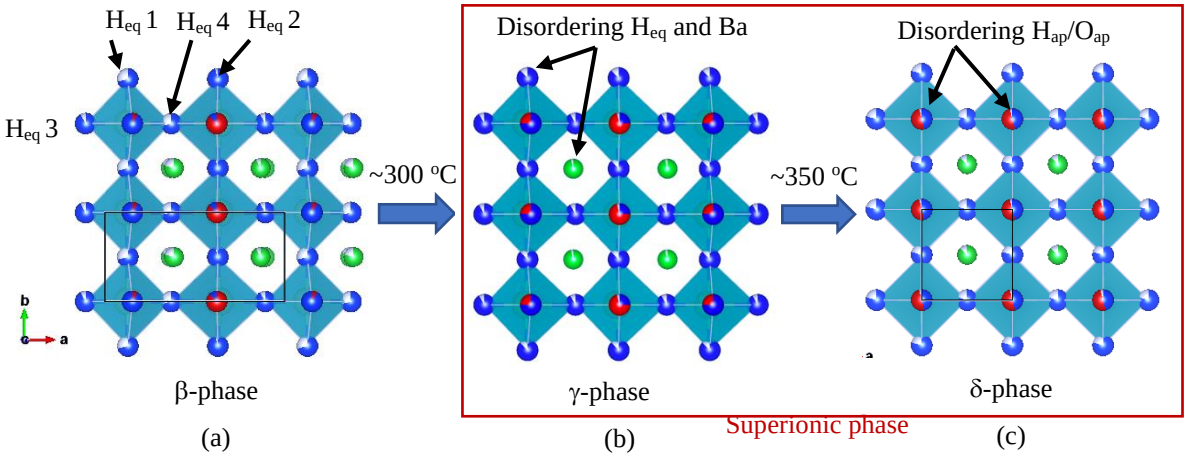

Figure 4.2 Phase transition of BLHO (a) β-phase → (b) γ-phase →(c) δ-phase [19].

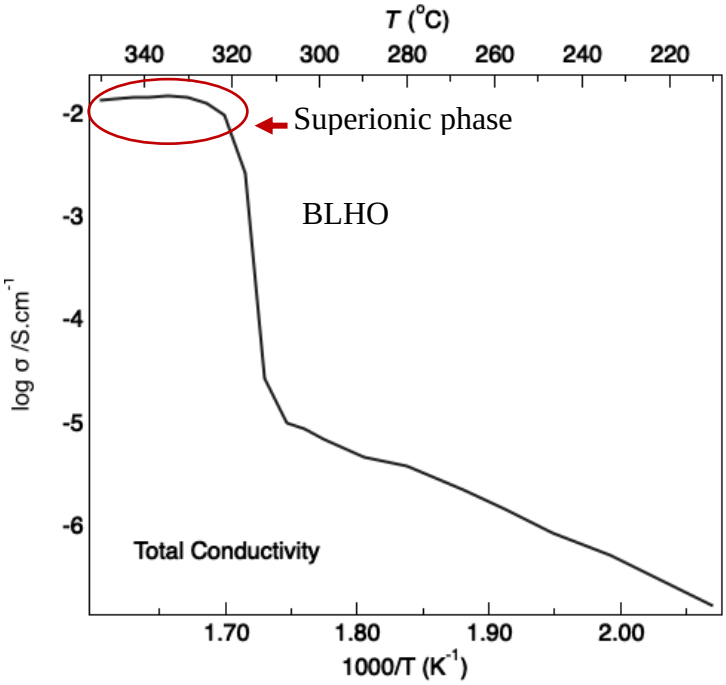

Figure 4.3 The Arrhenius plot of BLHO conductivity.

An abrupt change in the conductivity at high temperatures, as presented in Figure 4.3, corresponds to the phase transitions to the superionic phases at high temperatures. In other superionic carriers, the superionic behavior is commonly indicated by the nearly temperature-independent conductivity showing relatively low activation energy or nearly flat curve Arrhenius plot. The low activation energy in several superionic conductors had been ascribable to a collective or correlated ionic motion[59]. Correlate Li-ion migration was also reported in lithium superionic conductors in the LGPS series[60]. The structure study of reported superionic conductor materials such as AgI (Ag^+), $PbSnF_4$ (F^-), and LGPS (Li^+) revealed the presence of interstitial sites facilitating ionic migration pathway or concerted migration of ions visualized by MEM density map [61–64]. The MEM analysis is a powerful method to investigate the ionic conduction pathway.

In BLHO, the origin of the high conductivity of BLHO at the superionic phase is unknown. Therefore, the aim of this research in the topic (b) is to gain a new insight into the hydride conduction state of BLHO from the viewpoint of crystal structure, the origin of superionic conductivity, and to show the relationship between structure phase transition and superionic transition. Thus, we synthesized the deuterated sample, measured neutron diffraction in wide temperature ranges, and performed MEM analysis. First, the results of structure analyses are compared with the proposed model, then the relationship between conduction mechanism and hydrides ordering is discussed.

4.2 Experimental

4.2.1 Synthesis of Ba_2LiD_3O (BLDO)

In the structural study of Ba_2LiH_3O using the neutron diffraction method, the deuterated sample Ba_2LiD_3O was prepared and expected to have the same similar structure as the hydrogen phase. The BLDO sample was synthesized *via* solid-state reaction under the deuterium atmosphere of 0.2 MPa. The starting materials BaD_2 (93%, Kojundo), BaO (99.99%, Mitsuwa), and LiD (98%, Aldrich) were mixed in a ratio of 0.93:1:1.5 (excess of LiD) using planetary ball milling with agate pot and balls under 150 rpm for 3 hours. The mixing raw materials were then sintered at 650 ^oC in the deuterium gas atmosphere for 6 hours. This synthesis is quite sensitive to the amount of BaO as the initial material, which tends to remain after sintering. Therefore, to avoid BaO impurity, the initial amount of BaO raw material was reduced to 0.93. The synthesis method of ambient pressure synthesis, including the heating program, has been detailed in Chapter 2.

4.2.2 Characterizations

Laboratory X-ray diffractometer (XRD) Rigaku MiniFlex 600, the wavelength of CuKα_1 and CuKα_2, was used for phase identification. After confirming the quality of the deuterated sample BLDO, we measured the conductivity of the sample to confirm a similar superionic phase behavior. The conductivity measurements were performed using an AC impedance spectroscopy method using a Bio-Logic MTZ-35 analyzer with a measurement range of 35 MHz – 0.1 Hz and applied voltage 20-100 mV. The measurement was performed under D_2 gas flow at the temperature of 200 ^oC – 350 ^oC. The sample dimension was 1.25 mm thickness and 4.21 mm diameter with a 3 mm diameter H_2-blocking Mo electrode sputtered on both surfaces using RF sputtering at 30 W power for 30 minutes. Confirming the phase transition behavior, we collect temperature-dependent synchrotron diffraction (SXRD) data at BL02B2, SPring-8, where the sample is mounted in a quartz capillary with a diameter of 0.3 mm. The sample was rotated during measurement to avoid preferred orientation. The temperature-dependent neutron diffraction (ND) measurement was collected at the SPICA beamline, J-PARC. The sample is mounted in V-Ni can with diameter of a 6 mm sealed in Ar-gas filled glovebox. The neutron diffraction data were collected at room temperature up to 400 ^oC in certain temperature points refer to the phase transition temperature observed in SXRD.

4.3 Result

4.3.1 Laboratory X-ray Diffraction

The XRD pattern, see Figure 4.4, shows the splitting peaks or superlattice peaks of (201), (011), and (203), (013) as evidence of the superlattice structure in Ba_2LiD_3O similar to BLHO. The XRD pattern can be indexed well with orthorhombic structure with *Pnma* space-group indicates that the Ba_2LiD_3O (BLDO) was successfully synthesized.

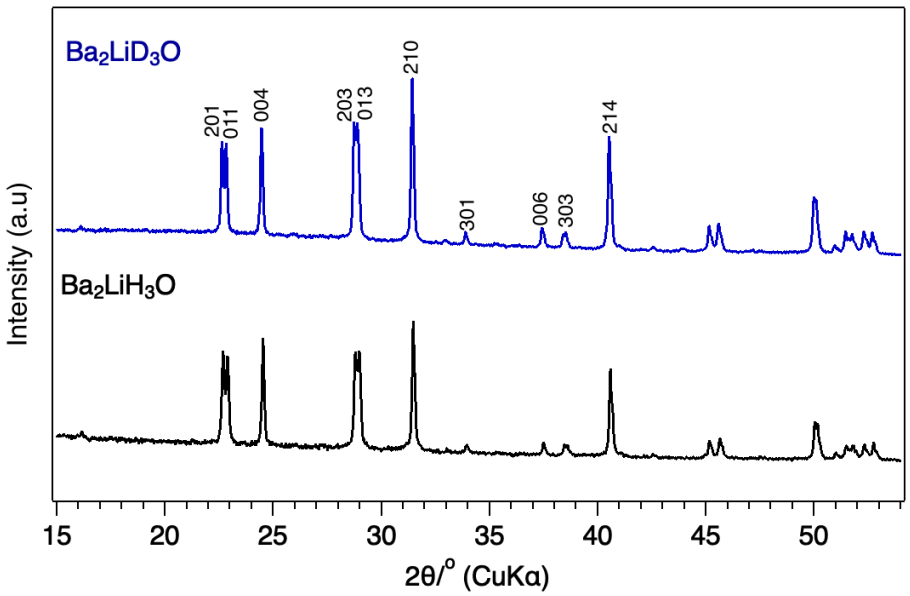

Figure 4.4 The XRD pattern of BLDO synthesized at ambient pressure.

4.3.2 Fourier Transform Infrared Spectroscopy (FT-IR)

The FT-IR spectroscopy of the absorbance data was collected to confirm the sample quality and check that there is no $^-$OH bonding in the sample. The $^-$OH bonding absorbance peak usually appears at the position around 1400 cm^{-1} [52]. In the FT-IR spectrum in Figure 4.5, the $^-$OH peak was not observed for both BLDO and BLHO, indicates that hydrogen in the BLDO sample is pure hydrides identical to BLHO.

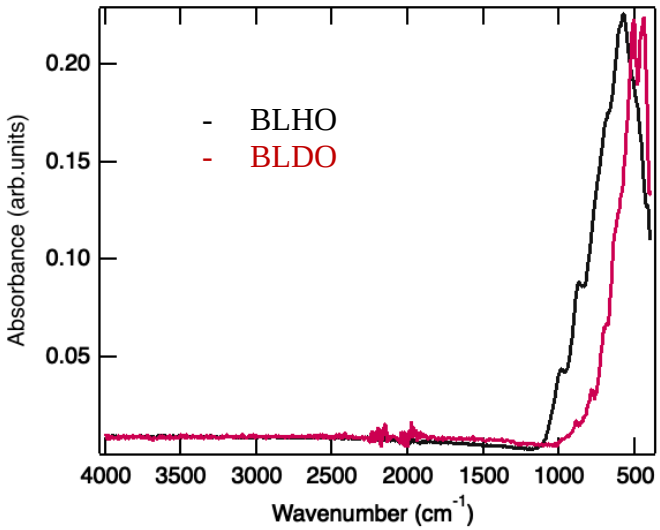

Figure 4.5 The FT-IR spectrum of Ba_2LiD_3O.

4.3.3 Synchrotron X-ray Diffraction (SXRD) at High Temperature

The SXRD measurement was performed at BL02B2, SPring-8, to study the structure and phase transition of BLDO. The sample was sealed under vacuum in a quartz capillary with a diameter of 0.3 mm. The temperature-dependent measurement was done up to 400 ^{o}C, higher than the second phase transition temperature, between 340 ^{o}C and 350 ^{o}C. The SXRD pattern is shown in Figure 4.6 refined using orthorhombic *Pnma* structure model refers to BLHO structure with the ordering of hydrogen and oxygen in the apical sites. The sample in this measurement consisted of a small amount of BaO impurity. The refined structure parameters listed in Table 4.1 shows reasonable and good fitting parameters.

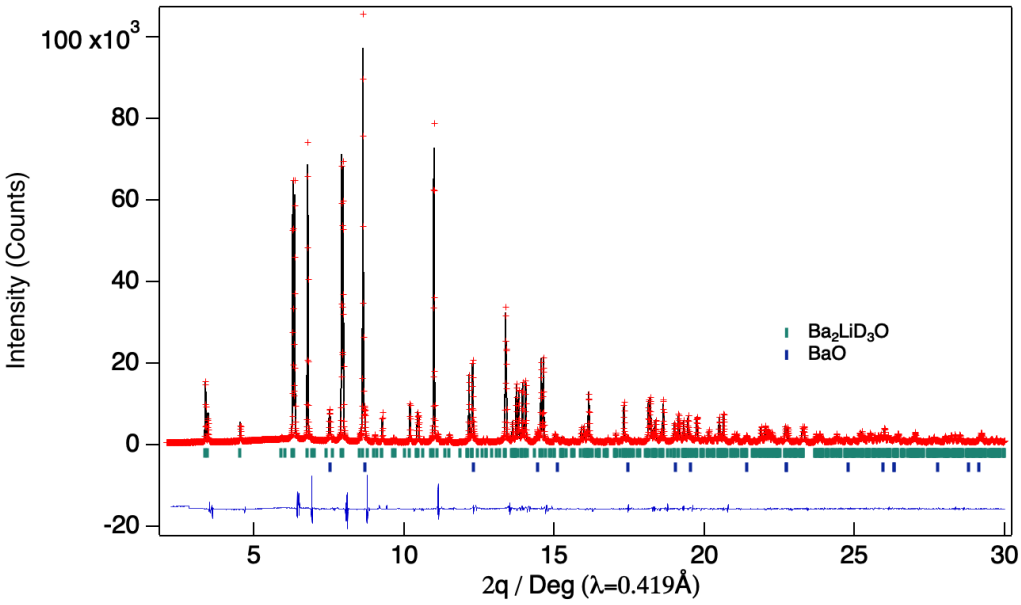

Figure 4.6 The SXRD pattern of BLDO measured at room temperature.

Table 4.1 The SXRD pattern of BLDO measured at room temperature.

Phase 1: Ba_2LiD_3O 94.24(2) wt%

atom	site	*g*	*x*	*y*	*z*	*B*/Å^2
Ba1	4*c*	1	0.11780(8)	0.25	0.10393(2)	0.656(6)
Ba2	4*c*	1	0.63720(8)	0.25	0.11682(2)	0.789(7)
Li1	4*c*	1	0.125	0.25	-0.25	0.5
H1	4*c*	1	0.375	0.25	-0.25	0.5
H2	4*c*	1	0.875	0.25	0.25	0.5
H3	4*c*	1	0.625	0.25	-0.0856	0.5
O1	4*c*	1	0.1353(4)	0.25	-0.08481(15)	1.54(7)

Unit cell: Orthorhombic *Pmna*, *a*= 7.92046(2), *b*= 3.922871(8), *c*= 14.16068(3)Å

R_{wp} = 7.23%, R_p=5.49%, R_e=2.27%, *S*=3.17, R_B=3.78, R_F=2.39%

Phase 2: BaO 5.76(2) wt%

atom	site	*g*	*x*	*y*	*z*	*B*/Å^2
Ba1	4*a*	1	0	0	0	0.5
O1	4*b*	1	0.5	0.5	0.5	0.5

Unit cell: Cubic *Fm-3m*, *a*=5.53610(10) Å, R_B=5.13%, R_F=2.20%

The high-temperature (HT) SXRD pattern of BLDO, Figure 4.7, shows the phase transition of BLDO from the orthorhombic to tetragonal phase between 340 - 360 ^oC, where the superlattice peaks start to disappear during heating. During cooling at 340 ^oC, the superlattice peak did not appear, indicating that the transition temperature shifted or lowered due to slow thermal stability inside the material. The refinement results of the room temperature data suggest that the Ba positions shifted, indicating barium ordering. In the Ba_2LiH_3O, the additional barium ordering is attributed to the additional Ba/*V* ordering in the structure. The HT SXRD data were analyzed using a multi-histogram fitting feature in Z-Rietveld software. The temperature-dependent of the lattice parameters are plotted in Figures 4.8, appended to those of BLHO. The lattice expansion behavior of both BLDO and BLHO are similar despite the larger lattice volume of BLDO due to the larger ionic size of deuterium.

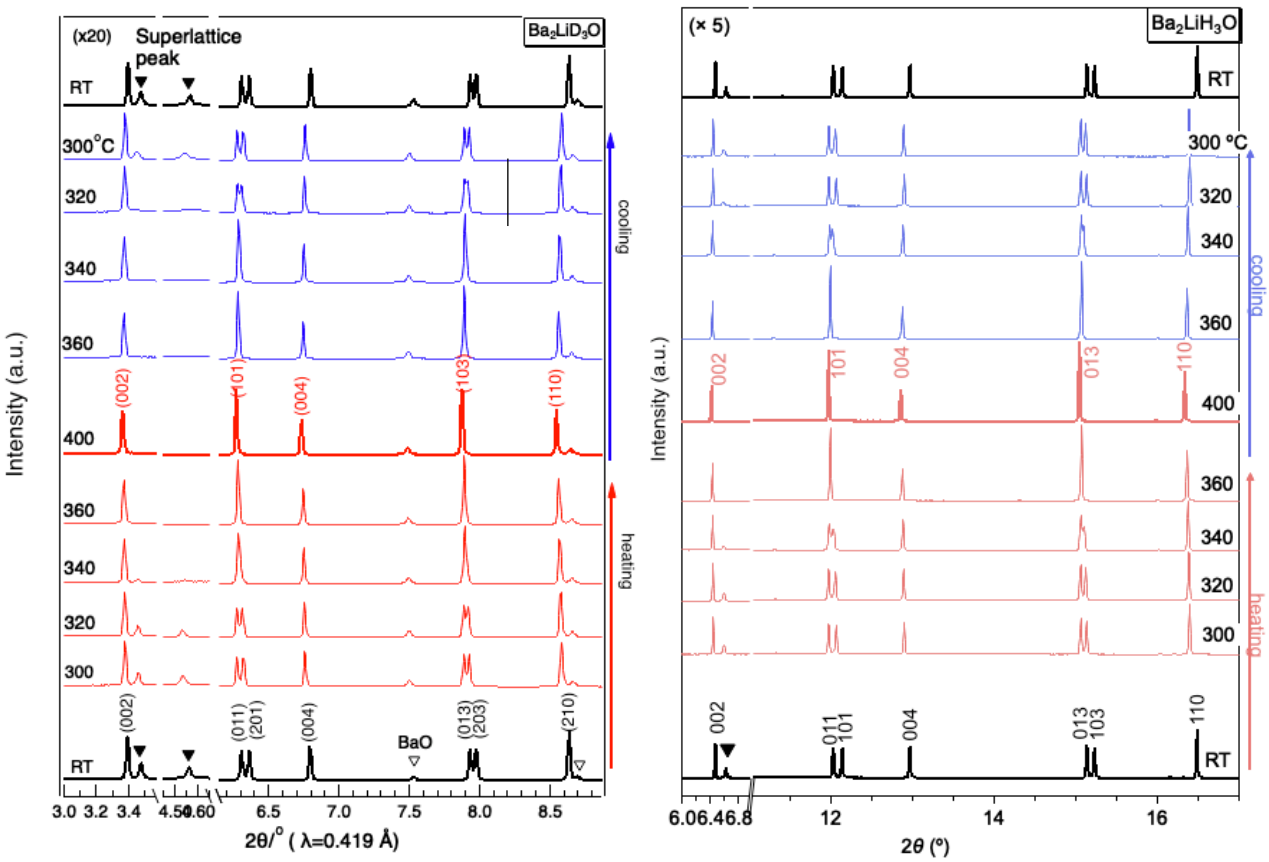

Figure 4.8 The temperature dependent SXRD pattern of BLDO (left) and BLHO (right).

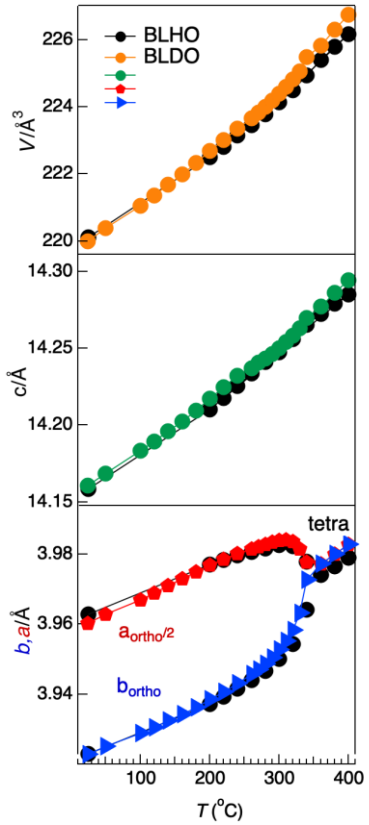

Figure 4.7 Lattice parameters of BLDO calculated from HT-SXRD refinement.

4.3.4 Electrochemical Impedance Spectroscopy (EIS)

The sample conductivity was calculated from the electrochemical impedance spectroscopy (EIS) data. The Arrhenius plot can be seen in Figure 4.9. The BLDO sample also shows a conductivity jump similar to BLHO, which occurred at a wider temperature than the hydrogen phase. At low temperature, β-phase, the conductivity of BLDO is about 10^{-5} S/cm at room temperature, which is higher than BLHO. It could be due to the contribution of the impurity and associated defect, including grain boundary. The conductivity behavior is different at the intermediate temperature of the γ-phase may be due to the different phase transition mechanism because of the different mass between hydrogen and deuterium. At the high-temperature region of the δ-phase, we also observed the superionic behavior in the deuterated sample with a lower conductivity than the BLHO. From this result, we can see that the isotope effect likely exists. The isotope effect was reported to affect the conductivity of the proton conductor [65–67]. In the proton conductor, assuming a simple hopping mechanism of direct exchange and classical approach, the isotope effect of the proton conduction can be calculated as below.

$$\frac{\sigma_H}{\sigma_D} \approx \sqrt{\frac{m_D}{m_H}} \approx \sqrt{\frac{2.014}{1.008}} \approx 1.41 \tag{4.1}$$

However, experimentally in BLHO, the observable σ_H/σ_D was nearly 3.21, larger than the proton conductor. Therefore, the isotope effect in BLDO may not follow simple hoping

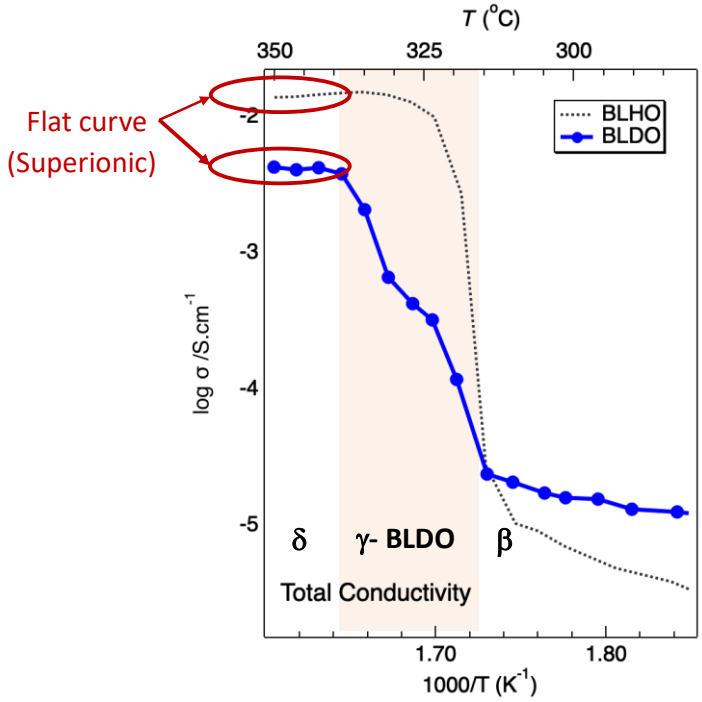

Figure 4.9 The Arrhenius plot of BLDO conductivity under deuterium gas condition.

mechanism. Instead, the more significant isotope effect may imply a large ions correlation. Regarding the sample stability during the EIS measurement, the XRD patterns after EIS under deuterium gas flow in Figure 4-10 indicate that the sample was stable without significant change of impurity phase, BaO. Therefore, the effect of a small amount of BaO ~ 5% on the conductivity can be considered minor and neglectable.

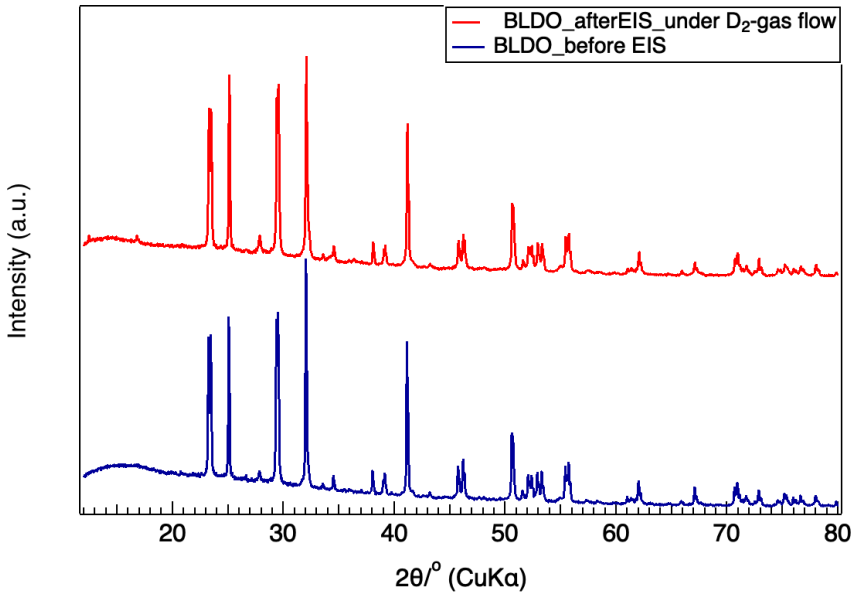

Figure 4.10 The XRD pattern of BLDO after EIS measurement under D_2-gas flow.

4.3.5 High-Temperature Neutron Diffraction

The high-temperature neutron diffraction (HT-ND) measurement revealed that the phase transition behavior of BLDO was similar to the hydrogen phase. During the heating measurement from room temperature to 340 ^{o}C, Figure 4-11 shows some additional superlattice peaks that appeared and were noticeable around 280 ^{o}C indicating phase transition to the γ-phase. Those superlattice peaks cannot be indexed with an orthorhombic *Pnma* structure. Indexing was obtained from the software Conograph [68] result in a larger orthorhombic unit cell superlattice with lattice parameters $a_s = 4b$, $b_s = c$, and $c_s = 2a$ corresponds to the lattice parameter of indexed in Figure 4.12. Those superlattice peaks did not appear during cooling.

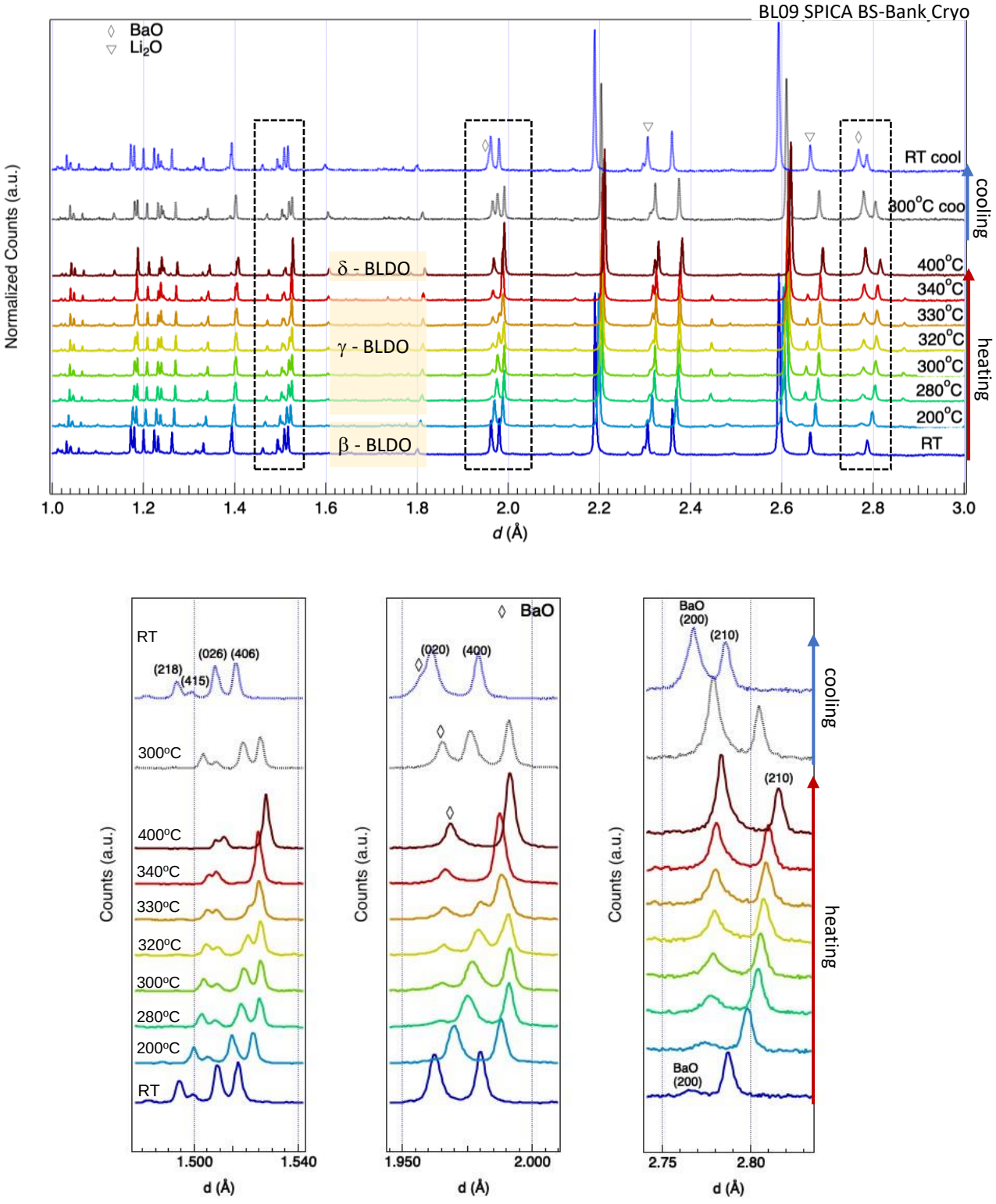

Figure 4.11 High temperature neutron diffraction for BLDO.

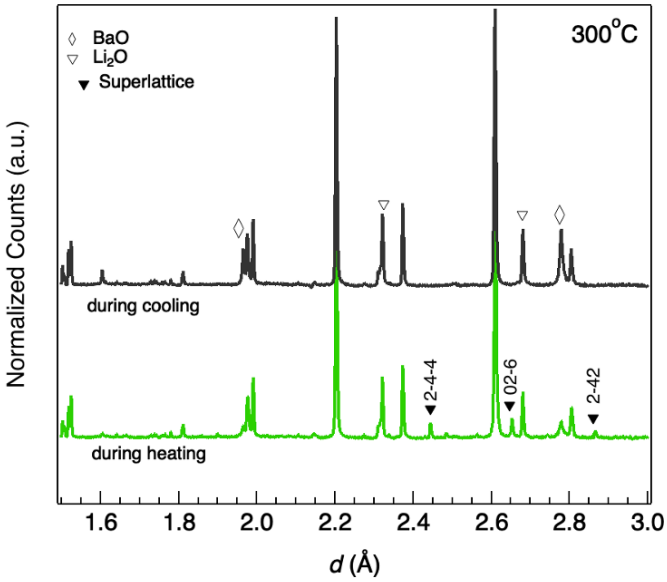

Figure 4.12 The indexing of the superlattice peaks at intermediate phase.

Phase transition is indicated by the changing of peak splitting (020) and (400), as detailed in Figure 4.11. Considering the (020) and (400) plane in the structure is identical; therefore, the calculated intensity should be similar. However, due to the broadening of (020), the intensity difference between (020) and (400) was observed. In this crystal structure model, the order-disorder of deuterium and oxygen is mainly in *a*-axis direction or doubling axis. The broadening of (002) imply local ordering may also occur in *b*-axis during phase transition, Figure 4.13.

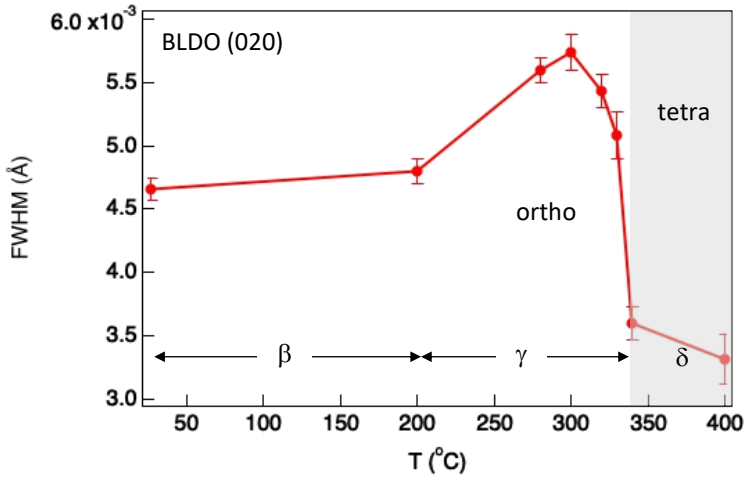

Figure 4.13 Peak broadening of (020) during the phase transition of BLDO.

During the measurement, BaO was increased by increasing temperature. The temperature-dependent of phase fraction change is represented in Figure 4.14. Considering

increasing BaO impurity, the barium and oxygen vacancy may increase, resulting in non-stoichiometry composition, which is neglected for neutron diffraction refinement.

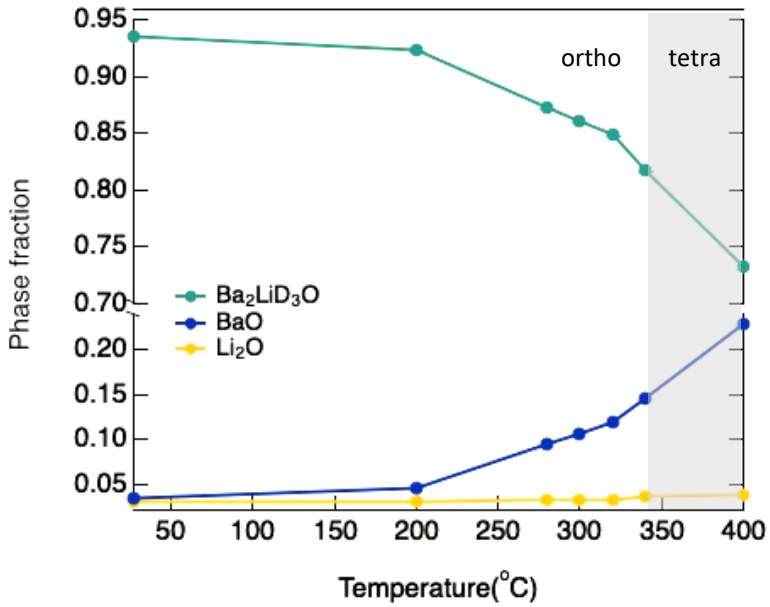

Figure 4.14 Phase fraction change during phase transition of BLDO.

4.3.6 Structure Refinement for MEM calculation

The refinement of HT-ND data of BLDO was used for MEM calculation. In order to obtain a reliable MEM result, the crystal model should be refined as close as possible to the experimental data obtaining the best fitting parameters. Furthermore, in order to avoid noise signals from the impurity, the local profile of the impurity peaks was refined. There are three different phase regions, the low-temperature phase (β), intermediate phase (γ), and high-temperature phase (δ). The low-temperature phase covers the temperature range from room temperature to 300 ^{o}C. The intermediate phase was indicated by the additional superlattice peak, which appeared at 280-340 ^{o}C before finally transform to the tetragonal phase (δ) at 400 ^{o}C. The refinement of the neutron diffraction data representing each region is presented.

4.3.6.1 Low Temperature Phase (27 °C)

At room temperature, the BLHO was reported in the *Pnm2₁* space group, but in this study, we adopted a higher symmetry space group for checking the general tendency resulted in a good fitting using orthorhombic *Pnma* unit cell (Figure 4.15). The equatorial hydride and apical hydride were ordered. In each hydride site, a small vacancy was likely to exist, which is also indicated by the high-temperature factor of hydrides compared to other atoms such as barium and oxide, see Table 4.2. The refinement of temperature factor B_{13} was omitted due to nearly zero value. At room temperature, the temperature factor of lithium showed a more significant value at the *b*-axis direction. By considering the possibility of local ordering, the detailed composition is assumed to be nearly stoichiometric.

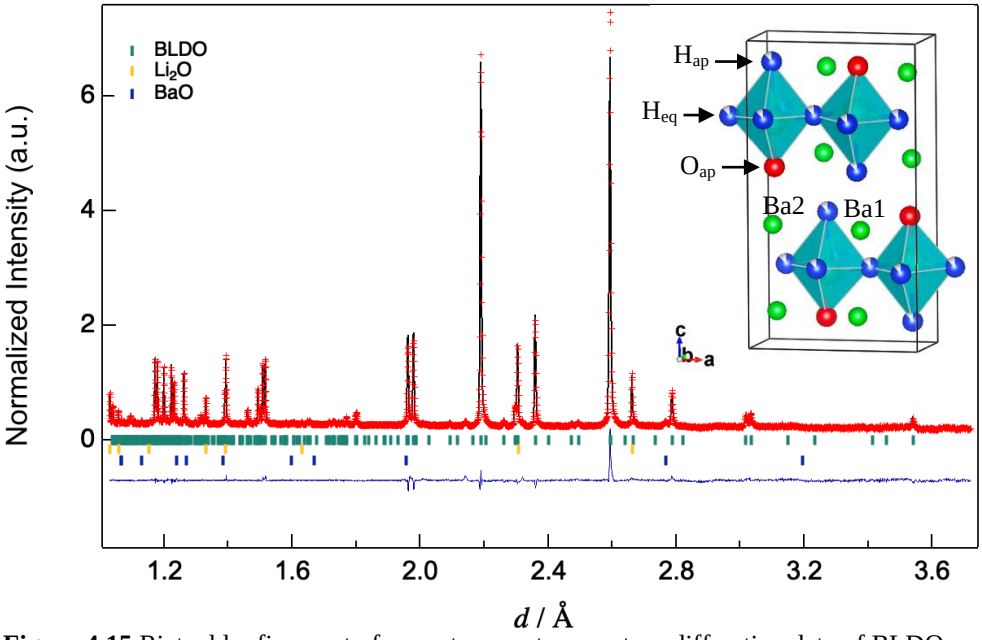

Figure 4.15 Rietveld refinement of room temperature neutron diffraction data of BLDO.

Table 4.2 Refined structure parameters of room temperature neutron diffraction data of BLDO.

Atom	Wyckoff	Label	*g*	x	y	*z*	B_{eq}/Å^2	B_{11}/Å^2	B_{22}/Å^2	B_{33}/Å^2
Ba1	4*c*	Ba	1	0.1379(5)	0.25	0.11698(11)	0.13(4)*			
Ba2	4*c*	Ba	1	0.1165(5)	0.25	0.39746(13)	0.30(4)*			
H1	4*c*	D	0.870(3)	0.3757(6)	0.25	0.25549(16)		0.96(7)	0.13(7)	0.67(6)
H2	4*c*	D	0.892(4)	0.1332(5)	0.75	0.25351(18)		0.58(7)	0.55(7)	1.24(6)
O1	4*c*	O	1	0.3712(5)	0.75	0.08384(11)		0.08(10)	0.83(15)	0.21(9)
Li1	4*c*	Li	1	0.3769(16)	0.75	0.2310(2)		0.38(18)	2.2(2)	0.6(2)
H3	4*c*	D	0.863(5)	0.3816(5)	0.75	0.42470(15)		1.15(11)	0.28(16)	1.81(11)

*Isotropic temperature factor

Phase 1: Ba_2LiD_3O 95.15 %, Unit cell: Orthorhombic *Pmna*, *a*=7.92017(3), *b*= 3.924842(14), *c*= 14.16214(5)Å

S= 1.31, R_{wp} = 3.18%, R_p=3.17%, R_e=2.42%, R_B=6.38%, R_F=4.17%

4.3.6.2 Low Temperature phase (200 °C)

At the higher temperature, 200 °C, the effect of local ordering is supposed to be reduced. The Rietveld refinement in Figure 4.16 resulted in a better pattern fitting. The hydride ordering was still preserved at equatorial and apical sites. In addition, a small vacancy of oxygen was observed, but not in the case of cation sites. The diffraction pattern suggested a full occupancy of barium and lithium sites. Compared to the room temperature data, increasing the temperature factor of all atoms summarized in Table 4.3 is in a reasonable value.

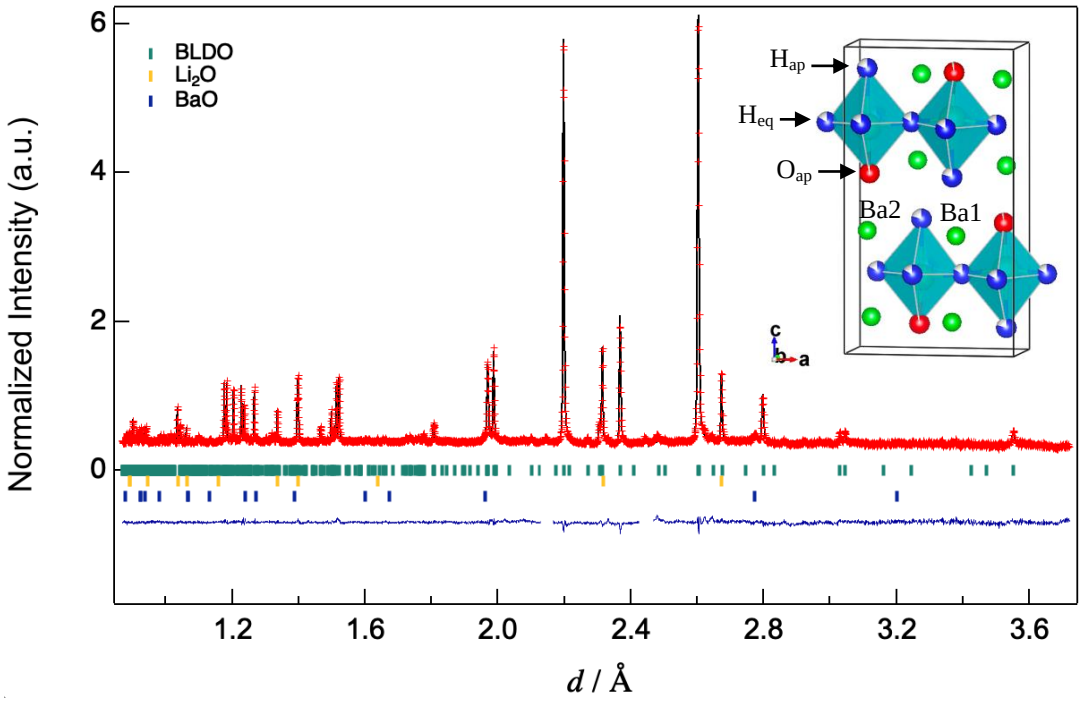

Figure 4.16 Rietveld refinement of neutron diffraction data of BLDO at 200 °C.

Table 4.3 Refined structure parameters of neutron diffraction data of BLDO at 200 °C.

Atom	Wyckoff	Label	*g*	*x*	*y*	*z*	B_{eq}/Å^2	B_{11}/Å^2	B_{22}/Å^2	B_{33}/Å^2	B_{13}/Å^2
Ba1	4*c*	Ba	1	0.1360(7)	0.25	0.11629(18)	0.372(5)*				
Ba2	4*c*	Ba	1	0.1126(7)	0.25	0.3970(2)	0.316(5)*				
Li1	4*c*	Li	1	0.3840(19)	0.75	0.2344(4)		1.2(2)	1.5(2)	1.4(3)	0
H1	4*c*	D	0.824(5)	0.3783(13)	0.25	0.2556(3)		1.513	1.217	1.320	0.1534
H2	4*c*	D	0.835(5)	0.1253(13)	0.75	0.2522(3)		1.418	1.536	2.020	0.1299
H3	4*c*	O	0.977(10)	0.3740(8)	0.75	0.0840(2)		0.573	0.292	0.949	0
O1	4*c*	D	0.802(9)	0.3866(9)	0.75	0.4249(3)		1.187	1.306	1.228	0

*Isotropic temperature factor

Phase 1: Ba_2LiD_3O 93.67 %, Unit cell: Orthorhombic *Pmna*, *a*=7.95179(6), *b*= 3.93970(3), *c*= 14.21276(8)Å

S= 1.01, R_{wp} = 3.06%, R_p=2.90%, R_e=2.79%, R_B=10.22%, R_F=6.32%

4.3.6.3 Intermediate Phase (320 °C)

The intermediate phase was indicated by the superlattice peaks located around 2.65 Å and 2.44 Å. The refinement in Figure 4.17 was done by excluding the superlattice peaks and adopting the crystal structure of 200 °C refinement result as the initial model. At 320 °C, the temperature factor of lithium listed in Table 4.4 is significant in the *b*-axis direction, similar to those hydride and oxide sites. The large anisotropic temperature factor at a particular direction may indicate the additional ordering that occurred, which brought up superlattice peaks. The details of the superlattice structure of the intermediate phase have not to be solved.

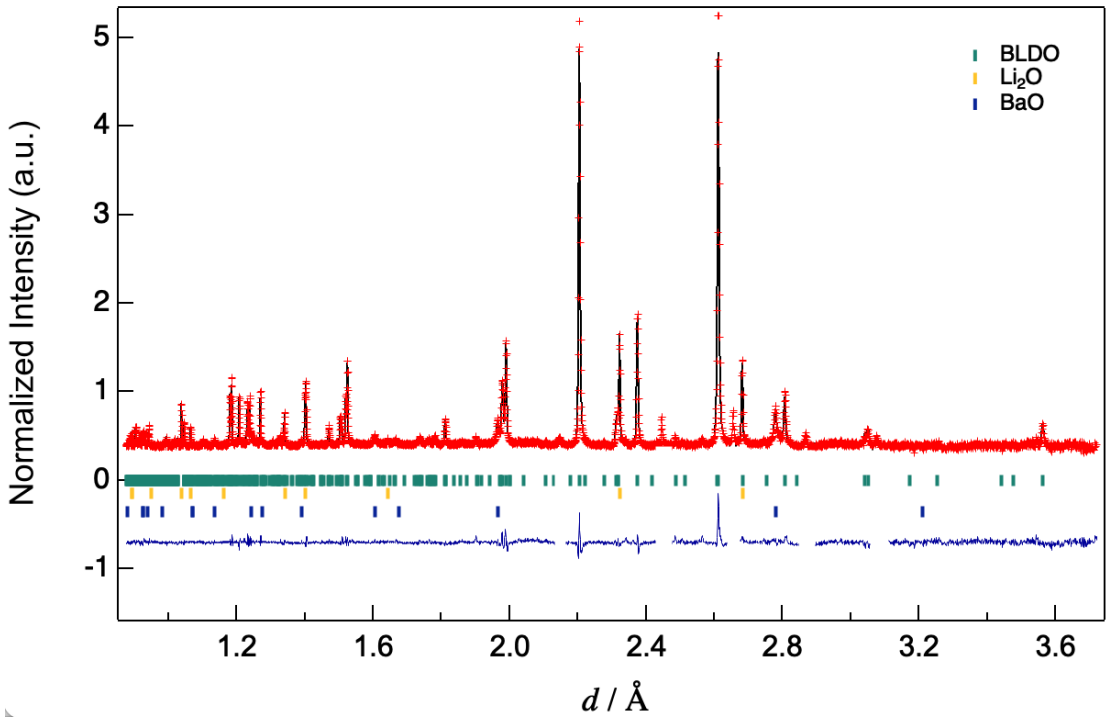

Figure 4.17 Rietveld refinement of neutron diffraction data of BLDO at 320 °C.

Table 4.4 Refined structure parameters of neutron diffraction data of BLDO at 320 °C.

Atom	Wyckoff	Label	*g*	*x*	*y*	*z*	B_{eq}/Å^2	B_{11}/Å^2	B_{22}/Å^2	B_{33}/Å^2
Ba1	4*c*	Ba	0.765(14)	0.1363(13)	0.25	0.1143(3)	0.50(8)*			
Ba2	4*c*	Ba	0.862(13)	0.1205(15)	0.25	0.3943(3)	1.00(8)*			
Li1	4*c*	Li	1	0.377(5)	0.75	0.2290(4)		2.73910	6.3(5)	2.3(5)
H1	4*c*	D	0.632(8)	0.372(2)	0.25	0.2540(5)		1.00(12)	2.87(19)	1.96(17)
H2	4*c*	D	0.649(9)	0.126(2)	0.75	0.2507(5)		0.60(13)	2.59(16)	2.14(17)
H3	4*c*	O	0.63270	0.3699(17)	0.75	0.0835(3)		0.61496	1.6(3)	0.38(16)
O1	4*c*	D	0.851(16)	0.3797(19)	0.75	0.4244(4)		1.86(17)	2.8(4)	2.76(19)

*Isotropic temperature factor

Phase 1: Ba_2LiD_3O 90.00 %, Unit cell: Orthorhombic *Pmna*, *a*=7.96260(5), *b*= 3.95991(4), *c*= 14.25454(10)Å

S= 1.26, R_{wp} = 3.41%, R_p=3.02%, R_e=2.69%, R_B=7.58%, R_F=7.72%

4.3.6.4 High-Temperature Phase (400 °C)

The BLDO structure at high-temperature phase 400 °C shows a disordered structure. The disordering of atoms results in higher symmetry, tetragonal *I*4/*mmm*. In Figure 4.18, the refinement result verified the similarity of superionic structure in both hydrogen and deuterium phase, BLHO and BLDO. At 400 °C, the refinement result summarized in Table 4.5 suggested the most significant lithium temperature factor. The anisotropic temperature factor of lithium indicates atomic displacement toward the *c*-axis direction, which differs from the tendency at low and intermediate temperatures. BaO impurity was increased at this temperature, introducing Ba-site vacancy result in a nearly similar composition to the hydrogen sample.

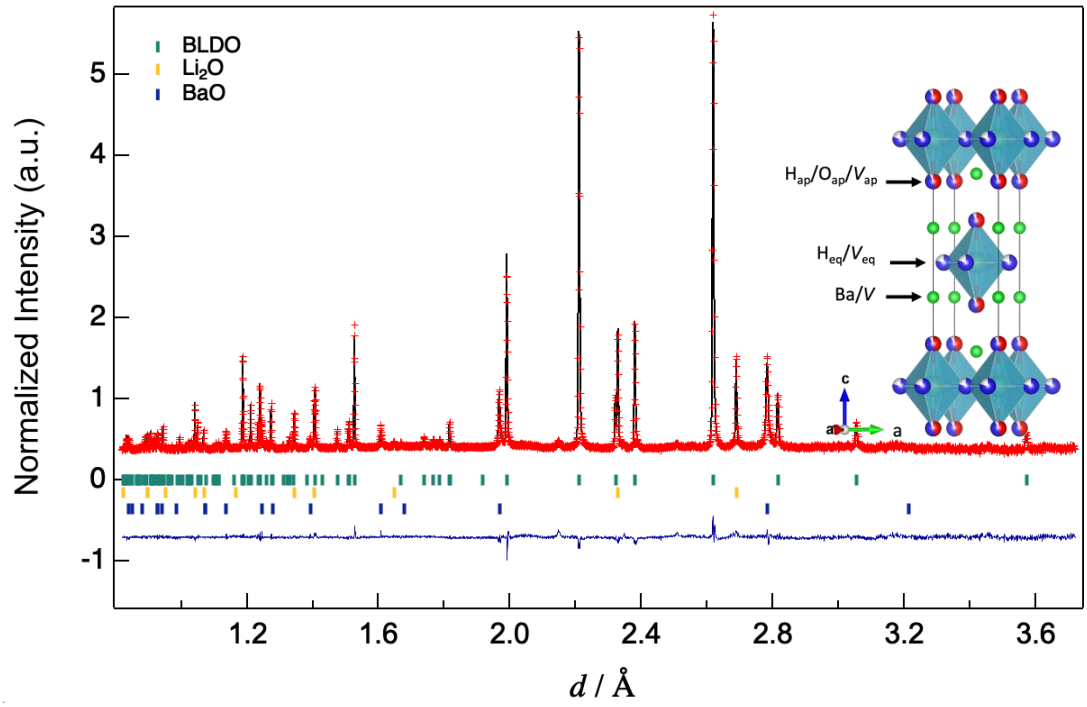

Figure 4.18 Rietveld refinement pattern of neutron diffraction data of BLDO at 400 °C.

Table 4.5 Refined structure parameters of neutron diffraction data of BLDO at 400 °C

Atom	Wyckoff	Label	*g*	*x*	*y*	*z*	B_{eq}/Å^2	B_{11}/Å^2	B_{22}/Å^2	B_{33}/Å^2
H1	4*c*	D	0.682(5)	0	0.5	0		2.17(8)	1.87(8)	2.39(8)
Li1	4*e*	Li	0.5	0	0	0.0202(10)		2.20(16)	2.20(16)	5.8(5)
O1	4*e*	O(0.45): D(0.55)	0.767(6)	0	0	0.17042(8)		2.12(6)	2.12(6)	2.01(7)
Ba1	4*e*	Ba	0.875	0	0	0.35989(8)	1.40(4)	1.37(5)	1.37(5)	1.45(6)

Phase 1: Ba_2LiD_3O 74.10 %, Unit cell: Tetragonal, *I*4/*mmm*, *a*= *b*= 3.982775(12), *c*=14.28975(7)Å

R_{wp} = 2.81%, R_p=2.54%, R_e=2.47%, *S*=1.14, R_B=4.98%, R_F=4.34%

4.4 Discussion

The $Ba_{1.75}LiH_{2.7}O_{0.9}$ (BLHO) has been studied having superionic conductivity at high-temperature phases of γ-phase and δ-phase with conductivity ~10^{-2} S/cm at 320-350 ^{o}C. The origin of the superconductivity and the conduction mechanism of this super-hydride conductor was unclear. As conductivity strongly relates to the crystal structure, the conduction mechanism study was proposed through structure study. The structure analysis of BLHO had been done using ND of the hydrogen sample because hydrogen is a light element and challenging to detect using XRD. In neutron diffraction, the scattering factor of hydrogen represented by the scattering length consists of coherent scattering and incoherent scattering. Deuterium, compared to hydrogen, has more significant coherent scattering. In this study, the deuterated sample, BLDO, was prepared for investigating the detailed structure of BLHO. The sample was successfully prepared by using the ambient pressure synthesis method. The laboratory XRD pattern indicated an isostructural to BLHO. The conductivity measurement confirmed that the deuterated sample became superionic at the δ-phase and the Rietveld refinement confirmed a similar structure to BLHO. The crystal structure of the room temperature phase or β-phase also results in an ordered structure with Ba/*V*, H_{eq}/*V*, and H_{ap}/O_{ap}. However, the γ-phase of BLDO shown a different structure and different temperature-dependent conductivity behavior. It might be due to the difference in the phase transition mechanism at the intermediate phase or γ-phase attributed to the difference in mass between hydrogen and deuterium. Therefore, to study the structure of the superionic conductor phase of BLDO, this research focused on the superionic phase or δ-phase.

4.4.1 Interstitial site at rock-salt layer

The Rietveld refinement of the ND data of δ-phase measured at 400 ^{o}C, results in a similar structure as BLHO, Table 4.5. The refinement results also indicating a significant anisotropic temperature factor of the Li-sites. Based on this refinement result, a density distribution was calculated using MEM. The MEM distribution in Figure 4.20 reveals an additional positive nuclear density at the position between Ba sites and $H_{ap}/O_{ap}/V$ sites or coordinate (0,0,*z*). Ba, O, and D contribute a positive structure factor in this compound, but oxygen is unlikely to occupy interstitial sites considering its bonding with lithium, which is stronger than hydride. Therefore, the remaining candidates are Ba and D. The Rietveld refinement was calculated using both models of Ba interstitial and D interstitial. The MEM

calculation result in Figure 4.19 disagreed with the Barium interstitial model (local ordering model), which proved that the Deuterium interstitial model is acceptable. The MEM density distribution of the hydrogen sample calculated from the ND data also agrees with this result.

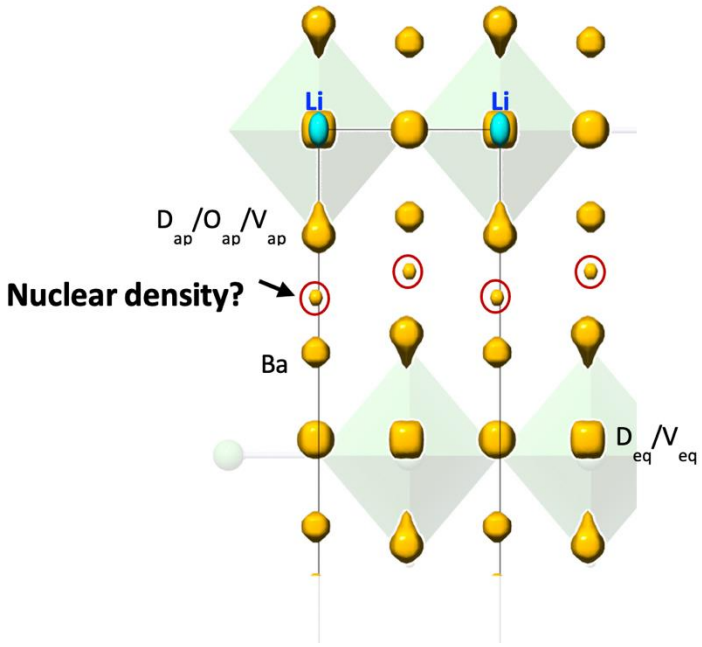

Figure 4.20 The MEM density map of δ-phase BLDO calculated from ND data. The iso-surface level is ±2.5 fm/Å^3. The blue region represents a negative structure factor, and the yellow distribution represents positive structure factor. Additional density peaks are indicated by red circle.

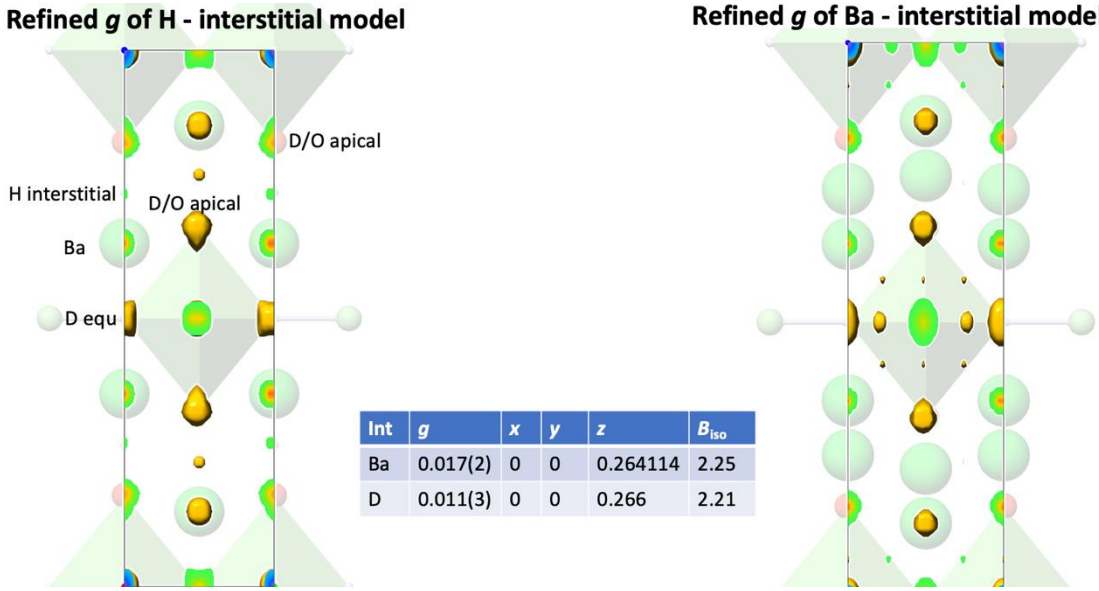

Int	g	x	y	z	B_{iso}
Ba	0.017(2)	0	0	0.264114	2.25
D	0.011(3)	0	0	0.266	2.21

Figure 4.19 The density map of the BLDO at 400 °C calculated using two different models of deuterium (H) interstitial model and barium interstitial model. The inset table indicated the structure information of the interstitial site. Refined structure model of tetragonal *I4/mmm* and iso-surface level ± 2 fm/ Å^3.

The Rietveld refinement re-calculated using the hydride-interstitial model is presented in Figure 4.21 and Table 4.6. By introducing deuterium at the hydride-interstitial site labeled with H3, it could slightly improve the refinement. The refinement of the occupancy and atomic position of the interstitial site H3 could be converged, which agrees with the data. The changing of the calculated fitting data was tiny, which is reasonable for resulting small amount of deuterium occupancy, approximately 1% at *8f* site with *z*=0.266.

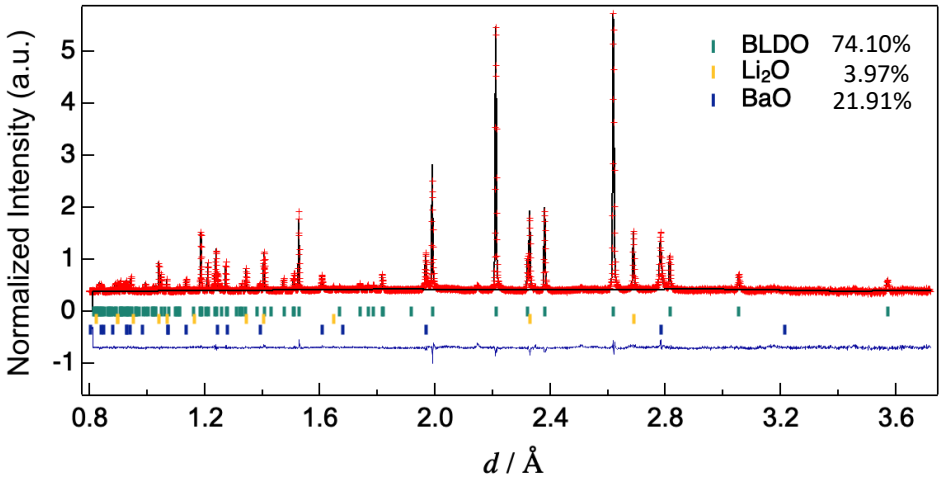

Figure 4.21 Neutron Rietveld refinement pattern of BLDO refined using hydride interstitial model at the rock-salt layer.

Table 4.6 Refined structure parameters of 400 ºC neutron diffraction data of BLDO using hydride interstitial model at rock-salt layer.

Atom	Wyckoff	Label	*g*	*x*	*y*	*z*	B_{eq}/Å^2	B_{11}/Å^2	B_{22}/Å^2	B_{33}/Å^2
H1	4*c*	D	0.679(5)	0	0.5	0		2.22(8)	1.89(8)	2.32(8)
Li1	4*e*	Li	0.5	0	0	0.0199(4)		2.0(15)	2.0(15)	6.6(5)
O1	4*e*	O(0.506): D(0.494)	0.763(6)	0	0	0.17046(8)		2.14(6)	2.14(6)	2.00(8)
Ba1	4*e*	Ba	0.875	0	0	0.35985(8)		1.34(5)	1.34(5)	1.53(7)
H3	**4*e***	**D**	**0.0123(15)**	**0**	**0**	**0.265(5)**	**2.00***			

*Isotropic temperature factor

Phase 1: Ba_2LiD_3O 74.10 %, Unit cell: Tetragonal, *I4/mmm*, *a*= *b*= 3.982775(12), *c*=14.28975(7)Å

R_{wp} = 2.80%, R_p=2.52%, R_e=2.47%, *S*=1.13, R_B=4.10%, R_F=4.23%.

The MEM analysis was calculated using the hydride interstitial model from the refinement results, Table 4.6. The position of the H3 site was confirmed from both MEM analysis and the Rietveld refinement results, as we can see in Figure 4-23. Here, the H3 site

in the rock-salt layer could be initiated from the apical deuterium. As mentioned earlier, the hydride is polarizable and flexible in size. Therefore, it is possible to sneak into the interstitial sites. In addition, during the phase transition, there is re-ordering of apical site hydrides, which suggests that the mobility between apical hydrides likely occurs, resulting in disorders in the apical sites at high temperatures.

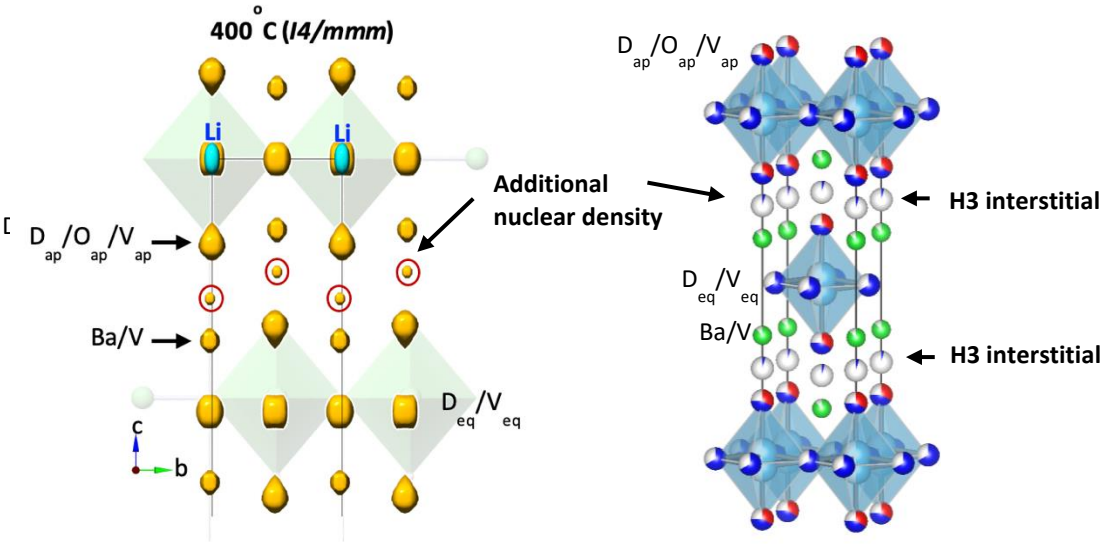

Figure 4.22 The position of H3 site calculated in (right) the Rietveld refinement is the same with the nuclear peak position calculated in (left) the MEM density map indicated in red circles. The iso-surface level is ±2.5 fm/Å^3.

4.4.2 Interstitial site at perovskite layer

In the MEM density map (Figure 4.22) in the perovskite layer, we can see the distribution shape in the lithium site, and equatorial hydride sites indicated extension along the c-axis direction. The density map was plotted in a lower iso-surface level of +0.05 fm/Å^3 to investigate the detail of the density distribution presented in Figure 4.23. We can see the detailed extension of the equatorial sites protrude toward apical sites. An interstitial site was introduced in this position labeled with H4 completing the previously obtained crystal model. The refinement pattern and the crystal structure are presented in Figure 4.24 and Table 4.7. The occupancy detected by the Rietveld refinement for H4 located in a 16*n* site is less than 1% or ~0.57%, half of the H3 (4*e*) occupancy. Although improving fitting parameters is hardly

observed, the refinement did not reject H4 sites, which means it possibly exists. Then, the MEM calculation was updated using this final crystal structure model.

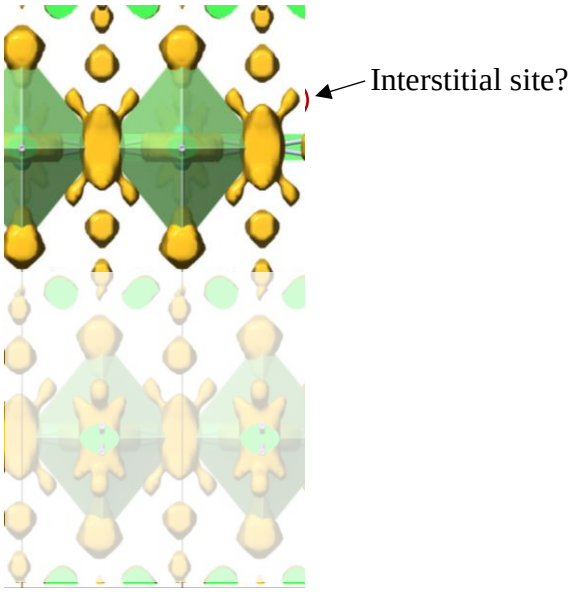

Figure 4.23 The MEM density map of δ-phase BLDO calculated from ND data overplotted with the structure model represented in green octahedral. The iso-surface level is +0.05 fm/Å^3. The yellow distribution represents positive structure factor. Additional density peaks are indicated by red circle.

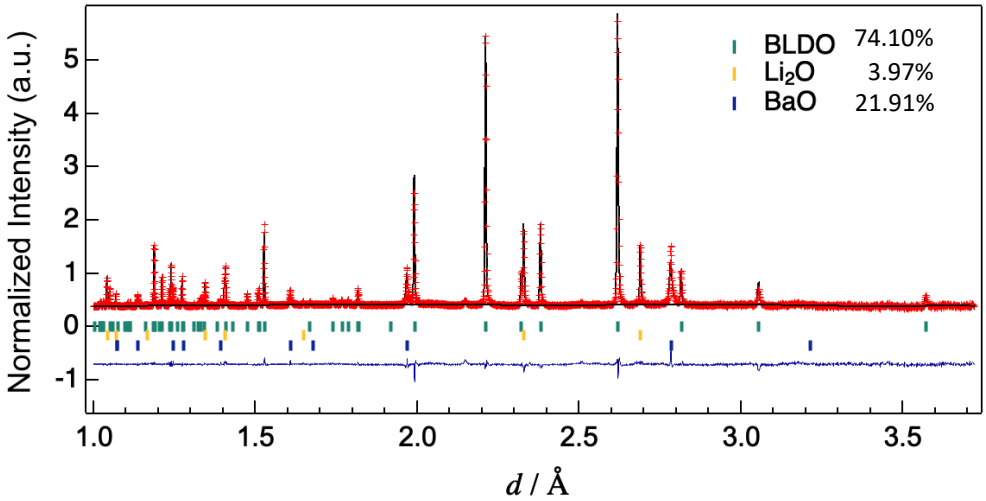

Figure 4.24 Neutron Rietveld refinement pattern of BLDO refined using hydride interstitial model at the perovskite layer.

Table 4.7 Refined structure parameters of 400 °C neutron diffraction data of BLDO using hydride interstitial model at perovskite layer.

Atom	Wyckoff	Label	*g*	*x*	*y*	*z*	B_{eq}/Å^2	B_{11}/Å^2	B_{22}/Å^2	B_{33}/Å^2
H1	4*c*	D	0.726(5)	0	0.5	0				
Li1	4*e*	Li	0.5	0	0	0.018(2)		1.91(16)	1.91(16)	7.3(19)
O1	4*e*	O(0.45):	0.8593	0	0	0.17037(8)				
		D(0.55)						2.56(6)	2.56(6)	2.43(6)
Ba1	4*e*	Ba	0.875	0	0	0.35973(8)		0.97(4)	0.97(4)	1.01(5)
H3_int	**4*e***	D	0.0123	0	0	0.265	2.00*			
H4	**16*n***	**D**	**0.0057(9)**	**0.5**	**0.199(18)**	**0.584(6)**	**2.00***			

*Isotropic temperature factor

Phase 1: Ba_2LiD_3O 74.10 %, Unit cell: Tetragonal, *I4/mmm*, *a*= *b*= 3.982775(12), *c*=14.28975(7)Å

R_{wp} = 2.86%, R_p=2.55%, R_e=2.47%, *S*=1.16, R_B=4.14%, R_F=4.84%.

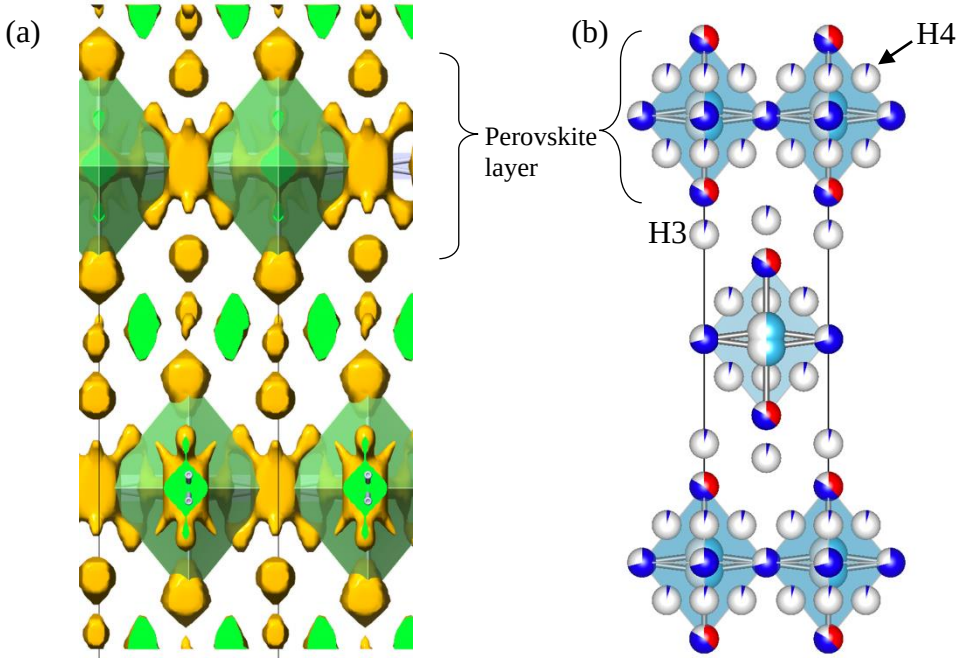

Figure 4.25(a) The MEM density map confirmed position of H4 site obtained from (b) the Rietveld refinement results. The iso-surface level is +0.05 fm/Å^3.

The discovery of H4 and its position were confirmed in the MEM analysis and Rietveld refinement, Figure 4.25. The presence of H4 could be explained as an indication of a strong ion correlation between lithium and equatorial hydrides sites. As in the refinement results, the lithium site has a large anisotropic temperature factor along the *c*-axis. Therefore, lithium's local vibration, which bound nearby hydrides, could induce mobility of hydride into the H4 sites illustrated in Figure 4.26.

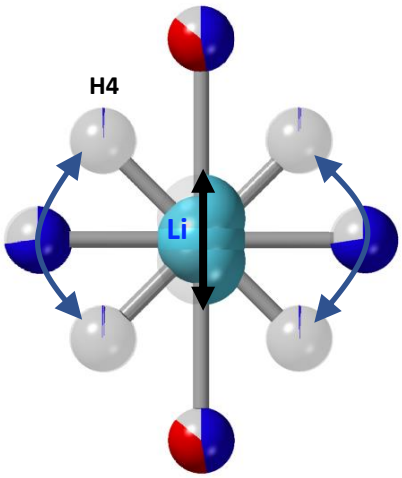

Figure 4.26 Illustration of strong ion correlation between Lithium and equatorial hydrides. The significant local ordering of lithium along c-axis induce the presence of H4 hydrides.

In this conclusion of the crystal structure, we have discovered interstitial hydride sites in the rock-salt layer and perovskite layer, which are H3 sites and H4 sites, respectively, from the MEM analysis and Rietveld refinement. The information collected from the analysis results including the occupancy of each site and the distance between sites. The discussion of the conduction mechanism in this superionic phase or d-phase BLDO refers to carrier distribution and distance between carriers, in this case, hydrides. The carrier distribution or hydride distribution indicates the dominant hydrides mobility contributes to the conductivity is equatorial hydrides as hydrides concentrated in the equatorial sites of the perovskite layer. Hence, the following discussion will focus on the hydride mobility on the perovskite layer, followed by the discussion of the additional contribution of hydride mobility in the rock-salt layer.

4.4.3 Conduction mechanism at perovskite layer

In the conventional model, the ionic mobility mechanism is explained by the single hopping model. In the single hopping model, the ion jumps from one site to another, requiring specific energy known as the activation energy. Several factors affect ion mobility, such as the carrier site's occupancy, including vacancy and the jump distance, which also determine the activation energy. This work will not discuss the activation energy but discuss those two factors to consider the preferable ionic jump mechanism. The jump distance or hydride-hydride distance and other site distance are summarized in Table 4.8.

Table 4.8 The distance between cations and anions. The selected anion-anion distance for the next discussion indicated in bold character.

cation-cation	distance (Å)	cation-anion	distance (Å)	anion -anion	distance (Å)
Ba – Ba	3.98277(0)	Li – H_{eq}	2.008(0)	**H_{eq} – H_{eq}'**	**2.81625(0)**
Ba – Ba	4.009(3)	Li – H/O_{ap}	2.18(17)	**H_{eq} – H4**	**1.34**
Ba – Li	3.31(4)	Ba – H3	2.29(4)	**H4 – H4**	**1.75**
Ba – Li	3.61(4)	Ba – H_{eq}	2.8255(9)	H4 – H/O_{ap}	1.78
				H_{eq} – H/O_{ap}	3.1453(9)

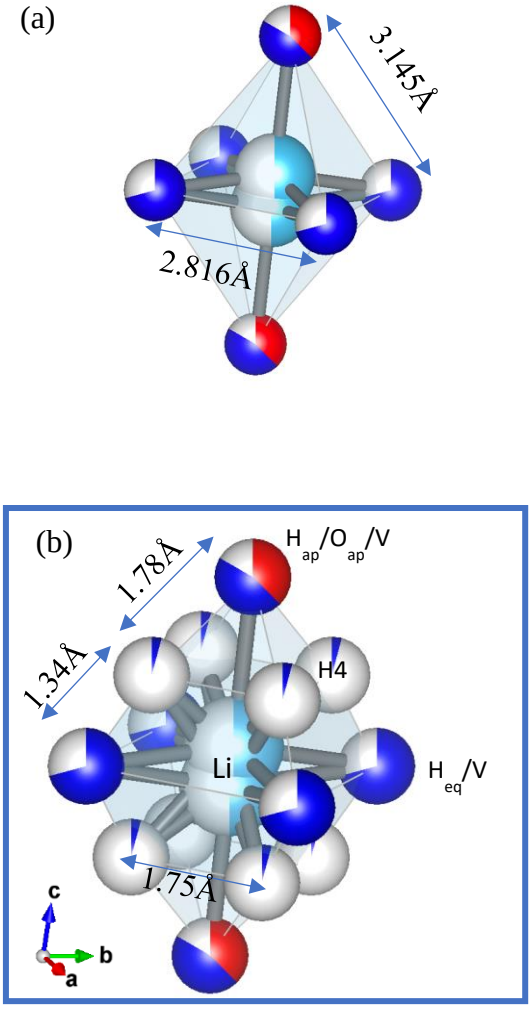

Figure 4.27 (a) The conduction mechanism in the conventional model and (b) proposed a new conduction mechanism by considering the interstitial site, H4.

In the conventional hydride jumping model illustrated in Figure 4.27(a), hydrides jump from one equatorial site to another equatorial site. The jumping distance is 2.81 Å with ion mobility via the vacancy mechanism. Hydride jump to the apical site is unlikely to occur due

to more considerable distance or more significant jump distance 3.14 Å and partial hydride occupancy in the apical sites. This mechanism is unlikely reported for the superionic case because the observed activation energy is small in the superionic phase, indicating nearly free ion mobility rather than single hopping.

By considering the finding of the interstitial site in the perovskite layer, H4, we can observe in Figure 4.27(b) that the carrier distance or hydride distance becomes shorter in this case ~1.3-1.7 Å. This carrier distance is comparable to those reported in fluoride superionic conductor $PbSnF_4$ [62], and it is likely known as one of the characteristics of the superionic phase. Furthermore, a shorter carrier distance indicates a strong ion correlation between carriers, hydrides that could induce correlated motion, as reported in the calculation study of lithium superionic conduction in LGPS series [59,60].

This research proposed a new conduction mechanism in the perovskite layer facilitated by the H4 site interstitial. Due to the presence of H4, there are more available hydride mobility pathways. Some of the possible pathways are illustrated in Figure 4.28, such as (1) H_{eq} → H4 → H_{eq}', (2) H_{eq} → H4 → H4'→ H_{eq}', and (3) H_{eq} → H4 → $H_{ap.}$ Among those three possibilities, the first pathway is likely favorable as we know that the equatorial - equatorial jump is reported as a dominant contribution. In this proposed model, the migration pathway for the hydride equatorial to apical mobility facilitated by H4 becomes more accessible, although the partial occupancy of oxygen in the apical site could hinder hydride mobility.

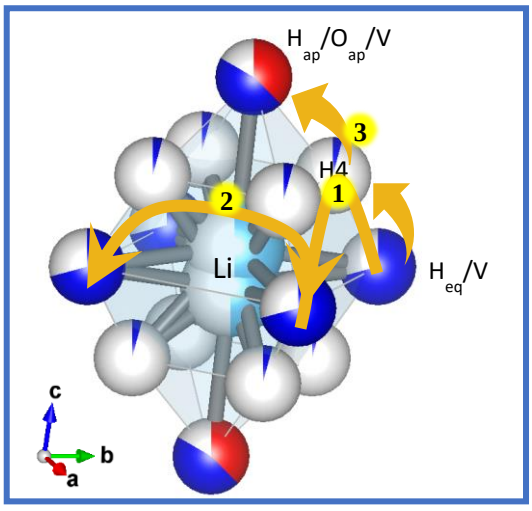

Figure 4.28 Some possible conduction pathways in the perovskite layer. The number indicating hydride mobility in (1) H_{eq} → H4 → H_{eq}', (2) H_{eq} → H4 → H4'→ H_{eq}', and (3) H_{eq} → H4 → $H_{ap.}$

4.4.4 Additional contribution of conduction of rock-salt layer

The conduction of hydride in K_2NiF_4-type structure was rarely reported on the rock-salt layer due to the dominant ordering of hydrides in the equatorial sites. Several oxyhydrides conductor were reported having ordering of hydride at the apical sites. However, the calculation study using AIMD method reported a higher energy is required for hydride mobility from equatorial sites to the apical sites compared to the hydride mobility between the apical sites[20]. A different tendency was reported in Ba_2ScHO_3 where hydride ordering only available in the apical sites resulting hydride mobility pathway along the rock-salt layer [69]. An interstitialcy mechanism was also reported possible in this structure via an interstitial site in the rock-salt layer as drawn in Figure 4.29.

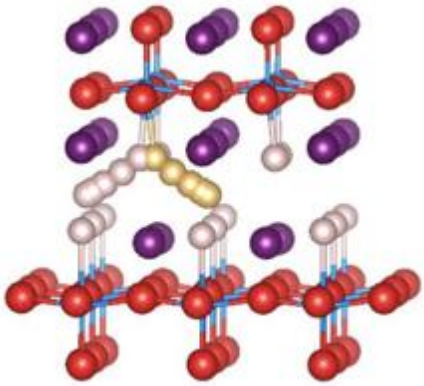

Figure 4.29 An interstitialcy mechanism reported in the calculation study of conduction mechanism in Ba_2ScHO_3 with apical hydride ordering [69].

The previous study suggested that the interstitial site in the rock-salt layer could support hydride migration between apical sites. However, it is unlikely favorable in the BLDO case considering a further distance between carriers compared to the perovskite layer. In addition, the apical sites are not fully occupied by hydride. Despite this, we could not avoid the possibility of additional contribution of rock-salt layer through interstitialcy mechanism. The possible hydrides pathways in the rock-salt layer are as illustrated in Figure 4.30.

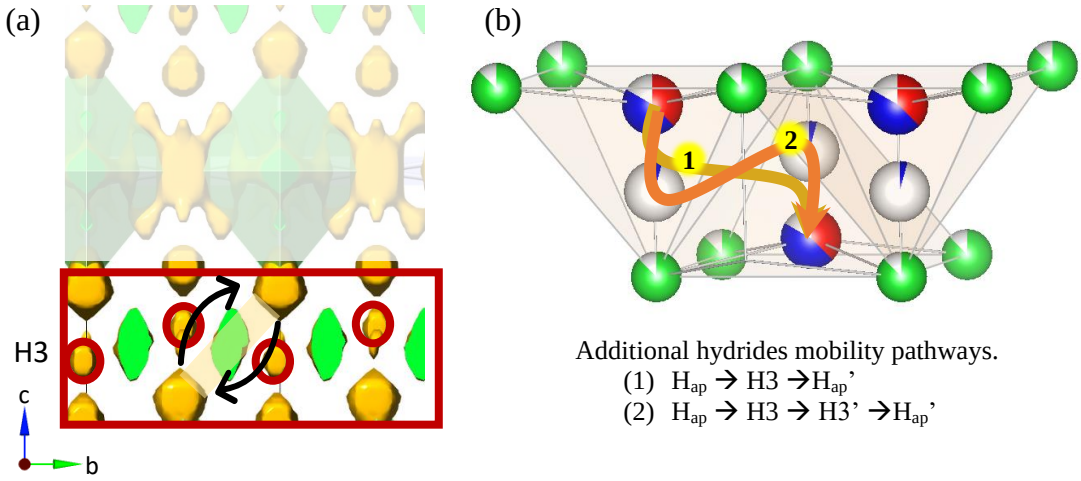

Figure 4.30 (a) MEM density distribution at the rock-salt layer and the possible hydrides pathway via H3 interstitial site.

Finally, considering all the available pathways in the perovskite and rock-salt layers, the total conduction mechanism. Hydride mobility is dominant in the equatorial sites of the perovskite layer where hydrides occupancy is concentrated, supported by additional mobility in the rock-salt layer. The interstitial site shortens the jump distance and induces a strong ionic correlation between hydrides ions, making concerted migration possible and resulting in superionic conductor behavior.

4.5 Conclusion

The Ba_2LiD_3O was successfully synthesized by solid-state reaction under ambient pressure. The structural study of the superionic hydride conductor of Ba_2LiD_3O with K_2NiF_4-type structure revealed that both hydrogen and deuterium phases have a similar superionic conductivity and phase transition nature similar for β-phase and δ-phase but different in γ-phase. The MEM calculation of the δ-phase structure suggested interstitial hydrides in the rock-salt-layer and perovskite layer. A new conduction mechanism was proposed in this study, with the dominant contribution to the conductivity is from the perovskite layer. The interstitial sites are likely to induce strong hydrides correlation, which results in superionic behavior.

Chapter 5

Summary

In terms of oxyhydride material exploration, we reported a successful preparation of the first oxyhydride with a gallium cation prepared under high pressure. Non-stoichiometric compositions of $(Ba,Sr)_{3-y}GaO_4H_x$ (x=0.22-0.30, y=0.10-0.15) adopted an anti-perovskite ABX_3 in a space group *I4/mcm* with Ba_3 as the inverse anion, GaO_4 in *A* site and H^- in *B* site or octahedral center. Although the $Ba_{2.85}GaO_4H_{0.70}$ is unstable in the air, the XRD data after TG shows the capability of H^-/O^{2-} replacement upon heating under dry oxygen flow. Here we summarized the reported oxyhydrides and oxyfluorides containing GaO_4 and AlO_4 units and plotted the stability region of anti-perovskite oxyhydride as structure prediction for oxyhydrides exploration in *p*-element cation. Further study of oxyhydrides in *p*-element cation in this anti-perovskite structure can be done by replacing the cation size with isovalent or aliovalent atom and anion replacement to increase hydrogen content in the sample.

The unique characteristics of hydride ions make it ideal for fast conduction. In this study, we investigated the hydride conduction in the superionic hydrides $Ba_{1.75}LiH_{2.7}H_{0.9}$ (BLHO). The deuterated sample was prepared, and the structure was studied by neutron diffraction, and MEM analysis showed a similar structure to BLHO at β-phase and δ-phase but different in γ-phase. The MEM calculation of the superionic phase, δ-phase, discovered interstitial hydrides in the rock-salt-layer and perovskite layer. The interstitial hydride in the perovskite layer implied a strong correlation between lithium and hydrides. Then, we proposed a new conduction mechanism in this study. The interstitial sites are likely to induce strong hydrides correlation, which results in superionic behavior. The reported BLDO structure in this report can be referred to for a calculation study for further investigation of hydride conductors in the K_2NiF_4-type structure. Furthermore, the study on other K_2NiF_4 type structures with different ordering of apical and equatorial sites may develop our knowledge on the mechanism of hydrides' mobility. In addition, the study on the isotope effect on the ionic conductivity in BLHO required a detailed investigation.

The hydrides in oxide material show exciting characteristic which differs to the hydrides in the metal. We observed the flexibility of hydride that could accommodate wider stability

to the cation replacement in BGHO. Furthermore, the discovery of hydrides in the interstitial site of BLDO indicates the capability of hydrides to sneak into the structure in oxide material.

References

1. Cardarelli F. Gases. In: Materials Handbook. 1981. p. 1689–99.
2. Kageyama H, Hayashi K, Maeda K, Attfield JP, Hiroi Z, Rondinelli JM, Poeppelmeier KR. Expanding frontiers in materials chemistry and physics with multiple anions. Nat Commun. 2018;9(1).
3. Smithson H, Marianetti CA, Morgan D, Van Der Ven A, Predith A, Ceder G. First-principles study of the stability and electronic structure of metal hydrides. Phys Rev B - Condens Matter Mater Phys. 2002;66(14):1–10.
4. Norby T, Widerøe M, Glöckner R, Larring Y. Hydrogen in oxides. Dalt Trans. 2004;(19):3012–8.
5. Monge M, Pareja R, González R, Chen Y. Positron bound states on hydride ions in thermochemically reduced MgO single crystals. Phys Rev B - Condens Matter Mater Phys. 1996;54(13):8950–3.
6. Widerøe M, Münch W, Larring Y, Norby T. Proton and apparent hydride ion conduction in Al-substituted $SrTiO_3$. Solid State Ionics. 2002;154–155:669–77.
7. Hayashi K, Sushko P V., Hashimoto Y, Shluger AL, Hosono H. Hydride ions in oxide hosts hidden by hydroxide ions. Nat Commun. 2014;5:1–8. Available from: http://dx.doi.org/10.1038/ncomms4515
8. Huang B, Corbett JD. Ba_3AlO_4H : Synthesis and Structure of a New Hydrogen-Stabilized Phase. J Solid State Chem. 1998;575(141):570–5.
9. Hayward MA, Cussen EJ, Claridge JB, Bieringer M, Rosseinsky MJ, Kiely CJ, Blundell SJ, Marshall IM, Pratt FL. The hydride anion in an extended transition metal oxide array: $LaSrCoO_3H_{0.7}$. Science (80-). 2002;295(5561):1882–4.
10. Yamaguchi S. Large, soft, and polarizable hydride ions sneak around in an oxyhydride. Science (80-). 2016;351(6279):1262–3.
11. Kobayashi Y, Hernandez OJ, Sakaguchi T, Yajima T, Roisnel T, Tsujimoto Y, Morita M, Noda Y, Mogami Y, Kitada A, Ohkura M, Hosokawa S, Li Z, Hayashi K, Kusano Y, Kim JE, Tsuji N, Fujiwara A, Matsushita Y, Yoshimura K, Takegoshi K, Inoue M, Takano M, Kageyama H. An oxyhydride of $BaTiO_3$ exhibiting hydride exchange and electronic conductivity. Nat Mater. 2012;11(6):507–11. Available from: http://dx.doi.org/10.1038/nmat3302
12. Yamamoto T, Zeng D, Kawakami T, Arcisauskaite V, Yata K, Patino MA, Izumo

N, McGrady JE, Kageyama H, Hayward MA. The role of π-blocking hydride ligands in a pressure-induced insulator-to-metal phase transition in $SrVO_2H$. Nat Commun. 2017;8(1). Available from: http://dx.doi.org/10.1038/s41467-017-01301-0

13. Kobayashi Y, Tang Y, Kageyama T, Yamashita H, Masuda N, Hosokawa S, Kageyama H. Titanium-Based Hydrides as Heterogeneous Catalysts for Ammonia Synthesis. J Am Chem Soc. 2017;139(50):18240–6.
14. Kobayashi G, Hinuma Y, Matsuoka S, Watanabe A. Pure H^- conduction in oxyhydrides. Science (80-). 2016;351(6279):1314–8.
15. Tanaka I. Nanoinformatics. Tanaka I, editor. Singapore: Springer Nature; 2018. 1–298 p.
16. Watanabe A. Synthesis and Hydride Ion Conductivities of K_2NiF_4-type Oxyhydrides. 2017.
17. Yashima M, Tsujiguchi T, Sakuda Y, Yasui Y, Zhou Y, Fujii K, Torii S, Kamiyama T, Skinner SJ. High oxide-ion conductivity through the interstitial oxygen site in $Ba_7Nb_4MoO_{20}$-based hexagonal perovskite related oxides. Nat Commun. 2021;12(1):1–7. Available from: http://dx.doi.org/10.1038/s41467-020-20859-w
18. Meng Y, Gao J, Zhao Z, Amoroso J, Tong J, Brinkman KS. Review: recent progress in low-temperature proton-conducting ceramics. J Mater Sci. 2019;54(13):9291–312. Available from: https://doi.org/10.1007/s10853-019-03559-9
19. Takeiri F, Watanabe A, Okamoto K, Bresser D, Lyonnard S, Frick B, Ali A, Imai Y, Nishikawa M, Yonemura M, Saito T, Ikeda K, Otomo T, Kamiyama T, Kanno R, Kobayashi G. (Under revision). 2021;
20. Bai Q, He X, Zhu Y, Mo Y. First-Principles Study of Oxyhydride H^- Ion Conductors: Toward Facile Anion Conduction in Oxide-Based Materials. ACS Appl Energy Mater. 2018;1(4):1626–34.
21. Nawaz H, Takeiri F, Kuwabara A, Yonemura M, Kobayashi G. Synthesis and H−conductivity of a new oxyhydride $Ba_2YHO_3$with anion-ordered rock-salt layers. Chem Commun. 2020;56(71):10373–6.
22. Takeiri F, Watanabe A, Kuwabara A, Ayu NIP, Yonemura M, Kanno R, Kobayashi G. Ba_2ScHO_3: H- conductive layered Oxyhydride with H- Site Selectivity. Inorg Chem. 2019;58:4431–6.
23. Takeiri F, Watanabe A, Kuwabara A, Nawaz H, Ayu NIP, Yonemura M, Kanno R, Kobayashi G. Ba_2ScHO_3 : H^- Conductive Layered Oxyhydride with H^- Site

Selectivity. Inorg Chem. 2019;58(7).

24. Sakaguchi T, Kobayashi Y, Yajima T, Ohkura M, Tassel C, Takeiri F, Mitsuoka S, Ohkubo H, Yamamoto T, Kim JE, Tsuji N, Fujihara A, Matsushita Y, Hester J, Avdeev M, Ohoyama K, Kageyama H. Oxyhydrides of (Ca,Sr,Ba)TiO_3 perovskite solid solutions. Inorg Chem. 2012;51(21):11371–6.
25. Gao S, Broux T, Fujii S, Tassel C, Yamamoto K, Xiao Y, Oikawa I, Takamura H, Ubukata H, Watanabe Y, Fujii K, Yashima M, Kuwabara A, Uchimoto Y, Kageyama H. Hydride-based antiperovskites with soft anionic sublattices as fast alkali ionic conductors. Nat Commun. (2021):1–10. Available from: http://dx.doi.org/10.1038/s41467-020-20370-2
26. Iwasaki Y, Matsui N, Suzuki K, Hinuma Y, Yonemura M, Kobayashi G, Hirayama M, Tanaka I, Kanno R. Synthesis, crystal structure, and ionic conductivity of hydride ion-conducting Ln_2LiHO_3 (Ln = La, Pr, Nd) oxyhydrides. J Mater Chem A. 2018;6(46):23457–63.
27. Matsui N, Hinuma Y, Iwasaki Y, Suzuki K, Guangzhong J, Nawaz H, Imai Y, Yonemura M, Hirayama M, Kobayashi G, Kanno R. The effect of cation size on hydride-ion conduction in $LnSrLiH_2O_2$(Ln = La, Pr, Nd, Sm, Gd) oxyhydrides. J Mater Chem A. 2020;8(46):24685–94.
28. Yamamoto T, Yoshii R, Bouilly G, Kobayashi Y, Fujita K, Kususe Y, Matsushita Y, Tanaka K, Kageyama H. An antiferro-to-ferromagnetic transition in $EuTiO_{3-x}H_x$ induced by hydride substitution. Inorg Chem. 2015;54(4):1501–7.
29. Katayama T, Chikamatsu A, Yamada K, Shigematsu K, Onozuka T, Minohara M, Kumigashira H, Ikenaga E, Hasegawa T. Epitaxial growth and electronic structure of oxyhydride $SrVO_2H$ thin films. J Appl Phys. 2016;120(8).
30. Amano Patino M, Zeng D, Blundell SJ, McGrady JE, Hayward MA. Extreme Sensitivity of a Topochemical Reaction to Cation Substitution: $SrVO_2H$ versus $SrV_{1-x}Ti_xO_{1.5}H_{1.5}$. Inorg Chem. 2018;57(5):2890–8.
31. Yamamoto T, Shitara K, Kitagawa S, Kuwabara A, Kuroe M, Ishida K, Ochi M, Kuroki K, Fujii K, Yashima M, Brown CM, Takatsu H, Tassel C, Kageyama H. Selective Hydride Occupation in $BaVO_{3-x}H_x$ ($0.3 \leq \times \leq 0.8$) with Faceand Corner-Shared Octahedra. Chem Mater. 2018;30(5):1566–74.
32. Bang J, Matsuishi S, Hiraka H, Fujisaki F, Otomo T, Maki S, Yamaura JI, Kumai R, Murakami Y, Hosono H. Hydrogen ordering and new polymorph of layered perovskite oxyhydrides: $Sr_2VO_{4-x}H_x$. J Am Chem Soc. 2014;136(20):7221–4.

33. Denis Romero F, Leach A, Möller JS, Foronda F, Blundell SJ, Hayward MA. Strontium vanadium oxide-hydrides: “square-planar” two-electron phases. Angew Chemie - Int Ed. 2014;53(29):7556–9.
34. Tassel C, Goto Y, Kuno Y, Hester J, Green M, Kobayashi Y, Kageyama H. Direct synthesis of chromium perovskite oxyhydride with a high magnetic-transition temperature. Angew Chemie - Int Ed. 2014;53(39):10377–80.
35. Tassel C, Goto Y, Watabe D, Tang Y, Lu H, Kuno Y, Takeiri F, Yamamoto T, Brown CM, Hester J, Kobayashi Y, Kageyama H. High-Pressure Synthesis of Manganese Oxyhydride with Partial Anion Order. Angew Chemie - Int Ed. 2016;55(33):9667–70.
36. Helps RM, Rees NH, Hayward MA. $Sr_3Co_2O_{4.33}H_{0.84}$: An extended transition metal oxide-hydride. Inorg Chem. 2010;49(23):11062–8.
37. Goto Y, Tassel C, Noda Y, Hernandez O, Pickard CJ, Green MA, Sakaebe H, Taguchi N, Uchimoto Y, Kobayashi Y, Kageyama H. Pressure-Stabilized Cubic Perovskite Oxyhydride $BaScO_2H$. Inorg Chem. 2017;56(9):4840–5.
38. Jin L, Lane M, Zeng D, Kirschner FKK, Lang F, Manuel P, Blundell SJ, McGrady JE, Hayward MA. $LaSr_3NiRuO_4H_4$: A 4d Transition-Metal Oxide–Hydride Containing Metal Hydride Sheets. Angew Chemie - Int Ed. 2018;57(18):5025–8.
39. Jin L, Hayward M. Rhodium-containing oxide-hydrides: covalently stabilized mixed-anion solids. Chem Commun. 2019;55 33:4861–4.
40. Joubert JC, Chenavas J. New Phases at High Pressure. In: Hannay NB, editor. Changes of State. Boston, MA: Springer US; 1975. p. 463–511. Available from: https://doi.org/10.1007/978-1-4757-1120-2_9
41. Yonemura M, Mori K, Kamiyama T, Fukunaga T, Torii S, Nagao M, Ishikawa Y, Onodera Y, Adipranoto DS, Arai H, Uchimoto Y, Ogumi Z. Development of SPICA, new dedicated neutron powder diffractometer for battery studies. J Phys Conf Ser. 2014;502(1).
42. Young RA. The Rietveld Method. Oxford University Press; 1993. 298 p.
43. Oishi R, Yonemura M, Nishimaki Y, Torii S, Hoshikawa A, Ishigaki T, Morishima T, Mori K, Kamiyama T. Rietveld analysis software for J-PARC. Nucl Instruments Methods Phys Res Sect A Accel Spectrometers, Detect Assoc Equip. 2009;600(1):94–6.
44. Brese NE, O’Keeffe M. Bond-valence parameters for solids. Acta Crystallogr Sect B. 1991;47(2):192–7.

45. Brown ID, Altermatt D. Bond-Valence Parameters Obtained from a Systematic Analysis of the Inorganic Crystal Structure Database. Acta Crystallogr Sect B41. 1985;244(2):244–7.
46. Magdysyuk O V, Smaalen S Van, Dinnebier RE. 4 . 8 . Application of the maximum-entropy method to powder-diffraction data. 2019;473–88.
47. Ishikawa Y, Zhang J, Kiyanagi R, Yonemura M. Physica B : Condensed Matter Z-MEM , Maximum Entropy Method software for electron / nuclear density distribution in Z-Code. Phys B Phys Condens Matter. 2018;(August 2017):1–4. Available from: https://doi.org/10.1016/j.physb.2018.03.034
48. Wu JF, Chen EY, Yu Y, Liu L, Wu Y, Pang WK, Peterson VK, Guo X. Gallium-doped $Li_7La_3Zr_2O_{12}$ garnet-type electrolytes with high lithium-ion conductivity. ACS Appl Mater Interfaces. 2017;9(2):1542–52.
49. Kendrick E, Kendrick J, Knight KS, Islam MS, Slater PR. Cooperative mechanisms of fast-ion conduction in gallium-based oxides with tetrahedral moieties. Nat Mater. 2007;6(11):871–5.
50. Matsuishi S, Hayashi K, Hirano M, Hosono H. Hydride ion as photoelectron donor in microporous crystal. J Am Chem Soc. 2005;127(36):12454–5.
51. Hayashi K. Kinetics of electron decay in hydride ion-doped mayenite. J Phys Chem C. 2011;115(22):11003–9.
52. Wu T, Fujii K, Murakami T, Yashima M, Matsuishi S. Synthesis and Photoluminescence Properties of Rare-Earth- Activated $Sr_{3-x}A_xAlO_4H$(A=Ca, Ba: x=0,1): New Members of Aluminate Oxyhydrides. Inorg Chem. 2020;
53. Brown ID. Bond Valences in Education. 2013. 233–250 p.
54. Im W Bin, Page K, Denbaars SP, Seshadri R. Probing local structure in the yellow phosphor $LaSr_2AlO_5:Ce^{3+}$, by the maximum entropy method and pair distribution function analysis. J Mater Chem. 2009;19(46):8761–6.
55. Vogt T, Woodward PM, Hunter BA, Prodjosantoso AK, Kennedy BJ. Sr_3MO_4F (M ، Al , Ga)— A New Family of Ordered Oxyfluorides. 2001;231(1999):228–31.
56. Nakamura K, Fujii K, Niwa E, Yashima M. Crystal structure and electrical conductivity of BaR_2ZnO_5 (R = Sm, Gd, Dy, Ho, and Er) a new structure family of oxide-ion conductors. J Ceram Soc Japan. 2018;126(5):292–9.
57. Downs AJ, Goode MJ, Pulham CR. Gallane at Last! Synthesis and Properties of Binary Gallium Hydride. J Am Chem Soc. 1989;111:1936–7.
58. Evans MJ, Holland GP, Garcia-Garcia FJ, Haussermann U. Polyanionic Gallium

Hydrides from AlB_2-Type Precursors AeGaE (Ae) Ca, Sr, Ba; E) Si, Ge, Sn). J Am Chem Soc. 2008;130:12139–12147.

59. He X, Zhu Y, Mo Y. Origin of fast ion diffusion in super-ionic conductors. Nat Commun. 2017;8(May):1–7. Available from: http://dx.doi.org/10.1038/ncomms15893

60. Yajima T, Hinuma Y, Hori S, Iwasaki R, Kanno R, Ohhara T, Nakao A, Munakata K, Hiroi Z. Correlated Li-ion migration in the superionic conductor $Li_{10}GeP_2S_{12}$. J Mater Chem A. 2021;(9):11278–84.

61. Kaneko Y, Ueda A. Dynamic Correlation and Cation Diffusion in a-AgI. J Phys Soc Japan. 1986;55(11):3924–30.

62. Fujisaki F, Mori K, Yonemura M, Ishikawa Y, Kamiyama T, Otomo T, Matsubara E, Fukunaga T. Mechanical synthesis and structural properties of the fast fluoride-ion conductor $PbSnF_4$. J Solid State Chem. 2017;253(June):287–93. Available from: http://dx.doi.org/10.1016/j.jssc.2017.06.007

63. Mori K, Mineshige A, Saito T, Sugiura M, Ishikawa Y, Fujisaki F, Namba K, Kamiyama T, Otomo T, Abe T, Fukunaga T. Experimental Visualization of Interstitialcy Diffusion Pathways in Fast-Fluoride-Ion-Conducting Solid Electrolyte $Ba_{0.6}La_{0.4}F_{2.4}$. ACS Appl Energy Mater. 2020;3(3):2873–80.

64. Kato Y, Hori S, Saito T, Suzuki K, Hirayama M, Mitsui A, Yonemura M, Iba H, Kanno R. High-power all-solid-state batteries using sulfide superionic conductors. Nat Energy. 2016;1(4):1–7.

65. Nowick AS, Vaysleyb A V. Isotope effect and proton hopping in high-temperature protonic conductors. Solid State Ionics. 1997;97(1–4):17–26.

66. Bonanos N, Huijser A, Poulsen FW. H/D isotope effects in high temperature proton conductors. Solid State Ionics. 2015;275:9–13.

67. Mehrer H, Imre AW, Tanguep-Nijokep E. Diffusion and ionic conduction in oxide glasses. Vol. 106, Journal of Physics: Conference Series. 2008. p. 012001.

68. Esmaeili A, Kamiyamaa T, Oishi-Tomiyasu R. New functions and graphical user interface attached to powder indexing software. J Appl Crystallogr. 2017;50:651–9.

69. Kuwabara A, Takeiri F, Nawaz H, Kobayashi G. First-Principles Calculations of Point Defect Formation and Anion Diffusion Mechanism in Oxyhydride Ba_2ScHO_3. ChemRxiv. 2020;2–4.

70. Fukui K, Iimura S, Tada T, Fujitsu S, Sasase M, Tamatsukuri H, Honda T, Ikeda K, Otomo T, Hosono H. Characteristic fast H^- ion conduction in oxygen-substituted

lanthanum hydride. Nat Commun. (2019):1–8. Available from: http://dx.doi.org/10.1038/s41467-019-10492-7

List of Figures

Figure 1.1 Hydrogen in the compound when it donors electron (H^+) or gains electron (H^-). 1

Figure 1.2 The partial replacement of oxygen by hydrogen in the $LaSrCoO_4$ (left) results in oxyhydride $LaSrCo_3H_{0.7}$. 3

Figure 1.3 Summary of conductivity of reported oxyhydrides.....4

Figure 1.4 The crystal structure of (a) $Ba_{1.75}LiH_{2.7}O_{0.9}$, (b) Ba_2YHO_3, and (c)Ba_2ScHO_3. The green, blue and red balls represent barium, hydrogen, and oxygen, respectively. The tetragonal represents the cation of Li, Y, and Sc in each. 5

Figure 1.5 Perovskite structure ABX_3 with partial substitution of oxygen by hydride results in $BaTiO_{3-x}H_x$. In this structure, *A*, *B*, and *X* represent barium, titanium, and oxide/hydride. 6

Figure 1.6 K_2NiF_4 structure showing a slab of layered perovskite and rock-salt structure..7

Figure 2.1 Cubic anvil of high-pressure apparatus. 10

Figure 2.2 The high-pressure cubic cell assembly.....11

Figure 2.3 The heating program of ambient pressure synthesis of Ba_2LiD_3O. 12

Figure 2.4 The stainless-steel container for ambient pressure synthesis. 12

Figure 2.5 Bragg condition for diffraction. 14

Figure 2.6 XRD sample holder for air-sensitive sample, (a) Al and (b) Silicon Rigaku holder. 14

Figure 2.7 Layout of beam line BL09 SPICA. 16

Figure 2.8 The heating program of temperature dependent neutron measurement of Ba_2LiD_3O. 17

Figure 2.9 Radiation shield covered the sample attached to the sample stick for the Cryo-furnace. 17

Figure 2.10 Heating program of TG measurement. 22

Figure 2.11 The Nyquist plot and the equivalent circuit were adopted to calculate the total resistivity of the sample R_b in this study. The R_s and C_b represent the cell resistance and capacitance, respectively. 23

Figure 3.1 The crystal structure of Mayenite oxide, C12A7 (left) similar to S12A7 and its cage structure with hydride ion trapped inside (right). 25

Figure 3.2 Crystal structure of (a) Ba_3AlO_4D and (b) Sr_3AlO_4H. 25

Figure 3.3 The laboratory XRD pattern of Ba_3GaHO_4H and Sr_3GaO_4H. 27
Figure 3.4 The XRD pattern of (a) mixed BaH_2+BaO+Ga_2O_3 after ball-milling and (b) after sintering under high-pressure. 28
Figure 3.5 The refined SXRD pattern of (a) Ba_3GaO_4H and (b)Sr_3GaO_4H. The red mark, black and blue pattern are the experimental pattern, the calculated pattern, and the difference pattern. The green tick marks indicate the main phase. The yellow tick mark on the Sr_3GaO_4H represents the SrO (18.7 wt%). 29
Figure 3.6 The crystal structure of A_3GaO_4H (*A* = Ba, Sr) drawn as layered structure and anti-perovskite structure. The green tetrahedral represents GaO_4. Gray balls represent Ba. Blue balls represent the expected position of hydrogen. 31
Figure 3.7 The normalized histogram data of Ba_3GaO_4H and Ba_3GaO_4D collected at BL09-Spica at room temperature. 31
Figure 3.8 The ND simulation pattern of (202) peak of (a) g = 0, (b) g = 1, and (c) g = 0.5 and (204), (310), (222) peaks of (e) g = 0, (f) g = 1, and (g) g = 0.5 compared to (d) (f) its normalized ND experimental data, respectively. 32
Figure 3.9 The refined ND pattern of (a) Ba_3GaO_4D and (b)Sr_3GaO_4D. The red mark, black and blue pattern are the experimental pattern, the calculated pattern, and the difference pattern. The green tick marks indicate the main phase, whereas the yellow tick mark on the Sr_3GaO_4H represents the SrO. 33
Figure 3.10 Laboratory X-ray diffraction of $Ba_{2.85}GaO_4H_{0.70}$ stability in air. The red line pattern is the initial pattern of $Ba_{2.85}GaO_4H_{0.70}$ mixed with Si powder as a reference. The sample decomposed right after contact with air. 35
Figure 3.11(a) TG curve of $Ba_{2.85}GaO_4H_{0.70}$ measured under Ar and O_2, and (b) the XRD pattern of the sample after TG measurement mixed with Si powder as reference. 36
Figure 3.12 Two root step synthesis of metastable oxyhydrides phase A_3GaHO_4 (*A*=Ba.Sr). 38
Figure 3.13 Structural illustration of the different layered density of atoms. 39
Figure 3.14 The summary of anti-perovskite gallium oxyhydrides and its reported isostructural oxyfluorides for structure prediction. 39
Figure 4.1 Crystal structure of BLHO at room temperature [19]. 42
Figure 4.2 Phase transition of BLHO (a) β-phase → (b) γ-phase →(c) δ-phase [19]. 42
Figure 4.3 The Arrhenius plot of BLHO conductivity. 43

Figure 4.4 The XRD pattern of BLDO synthesized at ambient pressure.....45
Figure 4.5 The FT-IR spectrum of Ba_2LiD_3O. 46
Figure 4.6 The SXRD pattern of BLDO measured at room temperature.....46
Figure 4.7 Lattice parameters of BLDO calculated from HT-SXRD refinement. 48
Figure 4.8 The temperature dependent SXRD pattern of BLDO (left) and BLHO (right).48
Figure 4.9 The Arrhenius plot of BLDO conductivity under deuterium gas condition. 49
Figure 4.10 The XRD pattern of BLDO after EIS measurement under D_2-gas flow.....50
Figure 4.11 High temperature neutron diffraction for BLDO. 51
Figure 4.12 The indexing of the superlattice peaks at intermediate phase.....52
Figure 4.13 Peak broadening of (020) during the phase transition of BLDO. 52
Figure 4.14 Phase fraction change during phase transition of BLDO.....53
Figure 4.15 Rietveld refinement of room temperature neutron diffraction data of BLDO. 54
Figure 4.16 Rietveld refinement of neutron diffraction data of BLDO at 200 ^oC.....55
Figure 4.17 Rietveld refinement of neutron diffraction data of BLDO at 320 ^oC.....56
Figure 4.18 Rietveld refinement pattern of neutron diffraction data of BLDO at 400 ^oC..57
Figure 4.19 The density map of the BLDO at 400 ^oC calculated using two different models of deuterium (H) interstitial model and barium interstitial model. The inset table indicated the structure information of the interstitial site. Refined structure model of tetragonal *I4/mmm* and iso-surface level $\pm$ 2 fm/ $Å^3$. 59
Figure 4.20 The MEM density map of δ-phase BLDO calculated from ND data. The iso-surface level is ±2.5 fm/$Å^3$. The blue region represents a negative structure factor, and the yellow distribution represents positive structure factor. Additional density peaks are indicated by red circle. 59
Figure 4.21 Neutron Rietveld refinement pattern of BLDO refined using hydride interstitial model at the rock-salt layer. 60
Figure 4.22 The position of H3 site calculated in (right) the Rietveld refinement is the same with the nuclear peak position calculated in (left) the MEM density map indicated in red circles. The iso-surface level is ±2.5 fm/$Å^3$.....61
Figure 4.23 The MEM density map of δ-phase BLDO calculated from ND data overplotted with the structure model represented in green octahedral. The iso-surface level is +0.05 fm/$Å^3$. The yellow distribution represents positive structure factor. Additional density peaks are indicated by red circle.....62

Figure 4.24 Neutron Rietveld refinement pattern of BLDO refined using hydride interstitial model at the perovskite layer.....62
Figure 4.25(a) The MEM density map confirmed position of H4 site obtained from (b) the Rietveld refinement results. The iso-surface level is +0.05 fm/Å^3.....63
Figure 4.26 Illustration of strong ion correlation between Lithium and equatorial hydrides. The significant local ordering of lithium along c-axis induce the presence of H4 hydrides.....64
Figure 4.27 (a) The conduction mechanism in the conventional model and (b) proposed a new conduction mechanism by considering the interstitial site, H4. 65
Figure 4.28 Some possible conduction pathways in the perovskite layer. The number indicating hydride mobility in (1) H_{eq} → H4 → H_{eq}', (2) H_{eq} → H4 → H4'→ H_{eq}', and (3) H_{eq} → H4 → $H_{ap.}$.....66
Figure 4.29 An interstitialcy mechanism reported in the calculation study of conduction mechanism in Ba_2ScHO_3 with apical hydride ordering [69]. 67
Figure 4.30 (a) MEM density distribution at the rock-salt layer and the possible hydrides pathway via H3 interstitial site. 68

List of Tables

Table 1.1 Summary of reported oxyhydrides. 8
Table 2.1 The list of scattering lengths, *b*, of some atoms on this report. 15
Table 3.1 Refined crystal structure parameters from SXRD data of Ba_3GaO_4H and its calculated BVS. 30
Table 3.2 Refined crystal structure parameters from SXRD data of Sr_3GaO_4H and its calculated BVS. 30
Table 3.3 Refined crystal structure parameters from ND data of Ba_3GaO_4H and its calculated BVS. 34
Table 3.4 Refined crystal structure parameters from ND data of Sr_3GaO_4H and its calculated BVS. 34
Table 3.5 BVS calculation of 4*a* site of some isostructural compounds with *I*4/*mcm* structure. 35
Table 3.6 Lattice parameters change of $Ba_{2.85}GaO_4H_{0.70}$ after TG. 37
Table 4.1 The SXRD pattern of BLDO measured at room temperature. 47
Table 4.2 Refined structure parameters of room temperature neutron diffraction data of BLDO. 54
Table 4.3 Refined structure parameters of neutron diffraction data of BLDO at 200 ^oC. ..55
Table 4.4 Refined structure parameters of neutron diffraction data of BLDO at 320 ^oC. ..56
Table 4.5 Refined structure parameters of neutron diffraction data of BLDO at 400 ^oC ...57
Table 4.6 Refined structure parameters of 400 ^oC neutron diffraction data of BLDO using hydride interstitial model at rock-salt layer. 60
Table 4.7 Refined structure parameters of 400 ^oC neutron diffraction data of BLDO using hydride interstitial model at perovskite layer. 63
Table 4.8 The distance between cations and anions. The selected anion-anion distance for the next discussion indicated in bold character. 65

Acknowledgments

I want to express my utmost gratitude to my supervisors, Professor Kamiyama Takashi, Associate Professor Kobayashi Genki, for their guidance throughout my project. I would also like to thank my promotor supervisor, Professor Itoh Shinichi, for his great patient and support in my doctoral training. I also would like to thank Associate Professor Saito Takashi, Assistance Professor Takeiri Fumitaka, and Assistance Professor Hagihara Masato for their valuable advice and assistance through my research work.

I would like to thank Associate Professor Yonemura Masao, who guided and supported my research work and introduced me to Professor Kobayashi Genki. In addition, my bachelor supervisor, Professor Evvy Kartini, introduced me to Professor Kamiyama Takashi and encouraged me to pursue my doctoral degree.

Thanks to fellow group members of Kobayashi laboratory, IMS, NINS. My colleagues Okamoto Kei and Uchimura Tasuku helped me with my experiment and valuable discussion. Technical staffs, Imai Yumiko, Kubota Akiko, and Nishikawa Masako provided me technical advice and support. Thanks to neutron powder group members, IMSS, KEK, Dr.Torii Shuki, Namba Kaoru, and Song Seungyub for technical advice and support.

I want to express my gratitude to the Japan Ministry of Education, Culture, Sports, Science, and Technology (MEXT) for the scholarship provided during my five years doctoral course and SOKENDAI Student Dispatch Program, which supported my stay in the Institute for Molecular Science and made this research collaboration possible.

Special thanks to my family, especially my parents, for their long prayer, my younger brother, younger sister, and my friends, for all their encouragement.

Nur Ika Puji Ayu